TABLE OF CONTENTS Page

LIST OF TABLES

Page

LIST OF FIGURES

Page

LIST OF ABREVIATIONS

AA	Aluminum Alloy
FSW	Friction Stir Welding
FEM	Finite Element Method
HAZ	Heat Affected Zone
TMAZ	Thermal Mechanical Affected Zone
PWHT	Post Weld Heat Treatment
UTS	Ultimate tensile strength
LOP	Lack of penetration
YS	Yield strength
A%	Total elongation percentage

LIST OF SYMBOLS

^0C	Degree Celsius
μm	Micrometer
Cm	Centimeter
HI	Heat Index
KJ	Kilo joule
MPa	Mega Pascal
mm	millimeter
nm	Nanometer
T	Temperature
T	Time
Wt%	Weight percent

INTRODUCTION

Aerospace industry always is looking for decreasing the weight and increasing the strength of aeronautic structures. 3rd generation Al-Li alloys e.g. AA2198 have highly desirable combinations of specific properties compared to their conventional counterparts, e.g. AA2024 which is a high demanded raw material for aeronautic structures. AA2198 is superior to AA2024 in high cycle fatigue (HCF) and fatigue strength. AA2198 has the capability to absorb between 2 to 3 times more energy to fracture in comparison to AA2024 for the same normalized applied stresses (Alexopoulos, Migklis, Stylianos, & Myriounis, 2013; Dursun & Soutis, 2014) that makes Al-Li alloys as good replacement for conventional aluminum alloys. However, they are relatively expensive. Therefore, an economical solution is to use hybrid designs with AA2198 alloys only for critical regions, while the remaining structure retain AA2024 alloys. In order to produce hybrid structures containing last generation and conventional aluminum alloys; a joining method is required. Unfortunately, conventional fusion welding methods cannot be used because of the fact that they produce welding defects, such as hot cracking (Handbook & Welding, 2005). The solution is to use a solid-state welding technique such as friction stir welding (FSW). FSW process is commercialized very well in both automobile and aerospace industry, e.g. it is currently used as an alternative to riveting for the assembly of airplane fuselages (Lohwasser & Chen, 2009). Therefore, FSW is an appropriate process for joining of AA2024 to AA2198. The goal of this study is the mechanical properties improvement of hybrid structures made by friction stir welding between AA2198 and AA2024 materials. Different tool designs, welding speed parameters, base metal heat treatment (T8 and T3), post weld heat treatment and the possibility of using active cooling during welding were investigated in order to improve the mechanical properties of the joint.

CHAPTER 1

LITERATURE REVIEW

1.1 Historical Development of Al-Li alloys

Aluminum alloy 2024-T351 plates were used for the lower wing skin of airplanes for many years (Cantor, Assender, & Grant, 2015). A research for conventional aluminum alloys replacement by aluminum-lithium material was started by Alcoa and Bombardier in order to decrease the weight and increase inspection interval (Giummarra, Thomas, & Rioja, 2007). The material substitution selection for 2024-T351 is important to decrease fuel consumption and maintenance cost. The fatigue crack growth (FCG) is the most important material properties for determining the inspection interval (Giummarra et al., 2007). The result of this study showed using aluminum-lithium alloy, e.g. 2199-T8E79 can decrease the airplane weight up to 25 percent over the 2024-T351 material. Composite forecasts & consulting LLC has calculated that decreasing just one pound of an aircraft weight could save between 440 to 700 $ per year for jumbo jets through decreasing annual fuel consumption. It shows how much is the importance of 2024-T351 replacement by AL-Li alloys. There are more details about this new material in the following sections.

1.1.1 First generation of AL-Li alloys

Improvement of mechanical properties is always on demand by industry. It is possible to improve the mechanical properties of aluminum alloys by work hardening and/or precipitate hardening. Lithium has high solubility at high temperatures and its solubility decreases by lowering the temperature. It is then good element for precipitate hardening. On the other hand, lithium is a light element so it is an interesting candidate for weight reduction (Prasad, Gokhale, & Wanhill, 2013). The research on the addition of lithium to aluminum alloys started in 1920[S] (Roberto & John, 2012). The earliest industrial application of first generation of aluminum alloys was 1958 in Table 1.1. The first generation of aluminum- lithium alloys had low

toughness and their production was expensive due to special requirement for reaction of lithium with oxygen during casting (Prasad et al., 2013).

Table 1.1 The earliest industrial application of first generation of Al-Li alloys (Prasad et al., 2013; Roberto & John, 2012)

Alloy	Li (Wt%)	The application	Year
2020	1.2	the wings of the Navy's RA-5C Vigilante aircraft	1958
01420	2.1	vertical-takeoff and landing aircraft Âk36 and Âk38 and liquid oxygen tanks	1970

1.1.2 Second generation of aluminum- lithium alloys

Research on the development of 2nd generation of AL-Li alloys started in early 1980S. Some proposed alloys are shown in Table 1.2 (Roberto & John, 2012). The 8090 alloy has the most successful application between the second generation of Al-Li alloys. It was used in European EH101 helicopters as structural components. Mostly, if any second generation aluminum-lithium alloys were used in aircraft besides the EH101 helicopter, it had been used for nonstructural, light duty applications (Cantor et al., 2015).

Table 1.2 The 2nd generation of AL-Li alloys which were prosed as a substitution of conventional aluminum alloys (Roberto & John, 2012)

Institution	Conventional material	2nd generation replacement	year
Alcoa	7075-T6	2090-T81	1984
Pechiney (from France)	2024-T3	2091-T8X	1985
British Aerospace Establishment	2024-T3	8090-T81	1984

In general, the preceding 2nd generation Al-Li products contained Li concentrations above 2 wt. pct. Although density reduction was clearly attractive, these products exhibited several characteristics that were considered undesirable by airframe designers. The advantage and limitation of 2nd aluminum alloys are summarized in Table 1.3 (Giummarra et al., 2007; Rioja & Liu, 2012).

Table 1.3 The advantage and limitation of 2nd aluminum alloys

Advantage	limitation
Higher Young modules Lower density lower fatigue crack growth (FCG) rates and higher fatigue life	Poor corrosion resistance Lower short-transverse fracture toughness Lower plane stress (K_c) fracture toughness/residual Strength in sheet form Tensile properties anisotropy

1.1.3 Third generation of aluminum- lithium alloys

The shortcomings of 1st and 2nd generation of Al-Li alloys pushed the scientists to work more on the alloy design principles of Al-Li alloys and it led to the successful development and commercialization of the 3rd generation Al-Li alloys with reduced Li concentration (Alexopoulos et al., 2013). 3rd generation Al-Li alloys have less than 1.8 wt. pct. of lithium. The chemical composition of some 3rd generation of aluminum alloys is shown in the Table 1.4 sorted by the year of introduction (Prasad et al., 2013; Roberto & John, 2012). It can be seen Li content of 3rd generation of Al-Li alloys has not changed significantly during recent years, in contrast to 2nd and 1st generation. The role of each element (alloy design principles) in 3rd generation Al-Li alloys has been summarized and it goes as follow (Rioja & Liu, 2012):

-Lithium and Magnesium: Age hardening, solid solution strengthening and density reduction

-Copper and Silver: Age hardening and solid solution strengthening

-Zinc: corrosion enhancement and solid-solution strengthening

-Zirconium and Manganese: controller of recrystallization and texture of wrought products

-Titanium: Grain refinement during ingots solidification

Iron, silicone, sodium and potassium are impurities and they have negative effect on the fracture toughness, fatigue, and corrosion (Roberto & John, 2012). It is important to understand the influence of chemical composition, geometry and location of precipitates and their role in the microstructure of 3rd generation alloys. Schematics of precipitates geometry and location in the 3rd generation Al-Li alloys is shown in Figure 1.1. T1 (Al_2CuLi), δ' (Al_3Li), and θ'-type (~Al_2Cu) precipitates increase the material strength. While T1 (Al_2CuLi), T2 (Al_6CuLi_3), β'(Al_3Zr), and $Al_{20}Cu_2Mn_3$ precipitates improve the fracture toughness. TEM micrographs of the strengthening precipitates in 3rd generation Al-Li alloys are shown in the Figure 1.2.

Typically, cold stretching is applied on Al-Cu-Li alloys before artificial aging to increase dislocations which are low energy nucleation sites for strengthening precipitates (Deschamps, Livet, & Bréchet, 1998). The material reaches to its maximum strength when T1, δ' and θ' precipitates are finely dispersed (S.-f. Zhang, Zeng, Yang, Shi, & Wang, 2014).

Table 1.4 Nominal Composition of Al-Li Alloys (Wt%) (Rioja & Liu, 2012)

Year	Alloys	Li	Cu	Mg	Ag	Zr	Mn	Zn
1992	2195	1.0	4.0	0.4	0.4	0.11	-	-
1997	2297	1.4	2.8	0.25 max	-	0.11	0.3	0.5 max
2000	2196	1.75	2.9	0.5	0.4	0.11	0.35 max	0.35 max
2000	2098	1.0	3.5	0.5	0.4	0.11	0.35 max	0.35 max
2002	2397	1.4	2.8	0.25 max	-	0.11	0.3	0.1
2003	2099	1.8	2.7	0.3	-	0.09	0.3	0.7
2004	2050	1.0	3.6	0.4	0.4	0.11	0.35	-
2005	2198	1.0	3.2	0.5	0.4	0.11	0.5 max	0.35 max
2005	2199	1.6	2.6	0.2	-	0.09	0.3	-
2010	2296	1.6	2.45	0.6	0.43	0.11	0.28	-
2011	2060	0.75	3.95	0.85	0.25	0.11	0.3	-
2012	2055	1.15	3.7	0.4	0.4	0.11	0.3	-

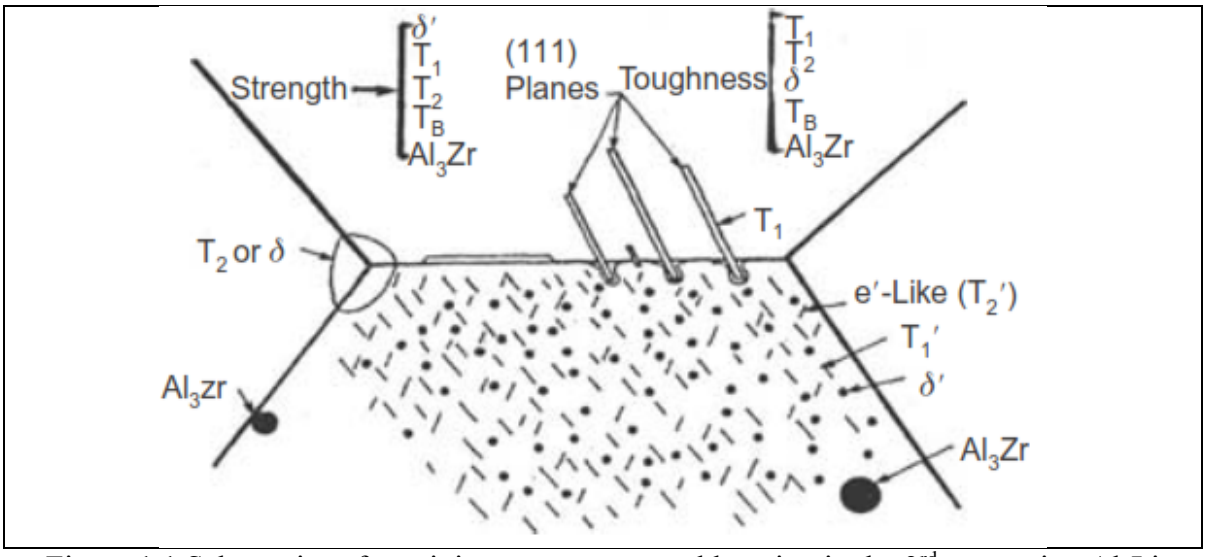

Figure 1.1 Schematics of precipitates geometry and location in the 3rd generation Al-Li alloys (Prasad et al., 2013)

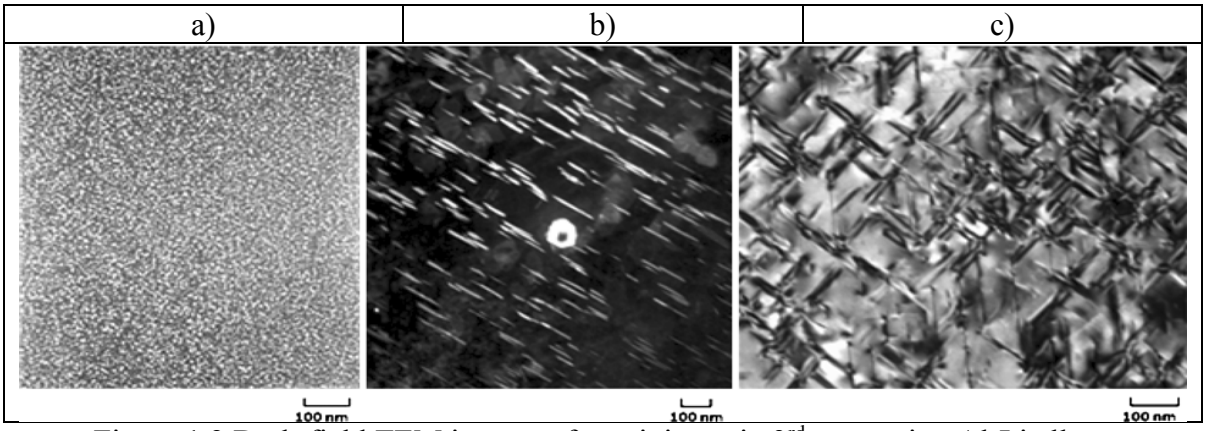

Figure 1.2 Dark-field TEM images of precipitates in 3rd generation Al-Li alloys : a) δ'(Al_3Li), b) T1 (Al_2CuLi), c) θ'(Al_2Cu) (Roberto & John, 2012).

AA2198 alloy is a good candidate from the 3rd generation of aluminum alloys. It has high mechanical properties while its damage tolerance and formability is also good (Heinz et al., 2000; Knüwer, Schumacher, Ribes, Eberl, & Bes, 2006). It has been used successfully for fuel tanks of Falcon 9 rocket (Li, Song, Guo, & Sun, 2013). Alcan developed AA2198 as a derivate of AA 2098 with lower content of copper and some minor chemistry modification for toughness optimization (Knüwer et al., 2006). It is possible to apply age hardening heat treatment on AA2198 close to net final shape, so the parts can obtain excellent combination of strength and toughness (S.-f. Zhang et al., 2014). The optical grain structure micrographs of

rolled 2198-T3 and 2024-T3 are shown in Figure 1.3. TD, RD and ND represents traverse direction, rolling direction and normal direction. he microstructure of 2198-T3 consists in flat pancake lying in the TD-RD plane (Robe, Zedan, Chen, Feulvarch, & Bocher, 2015) while 2024-T3 has equiaxed grains in TD-RD plane.

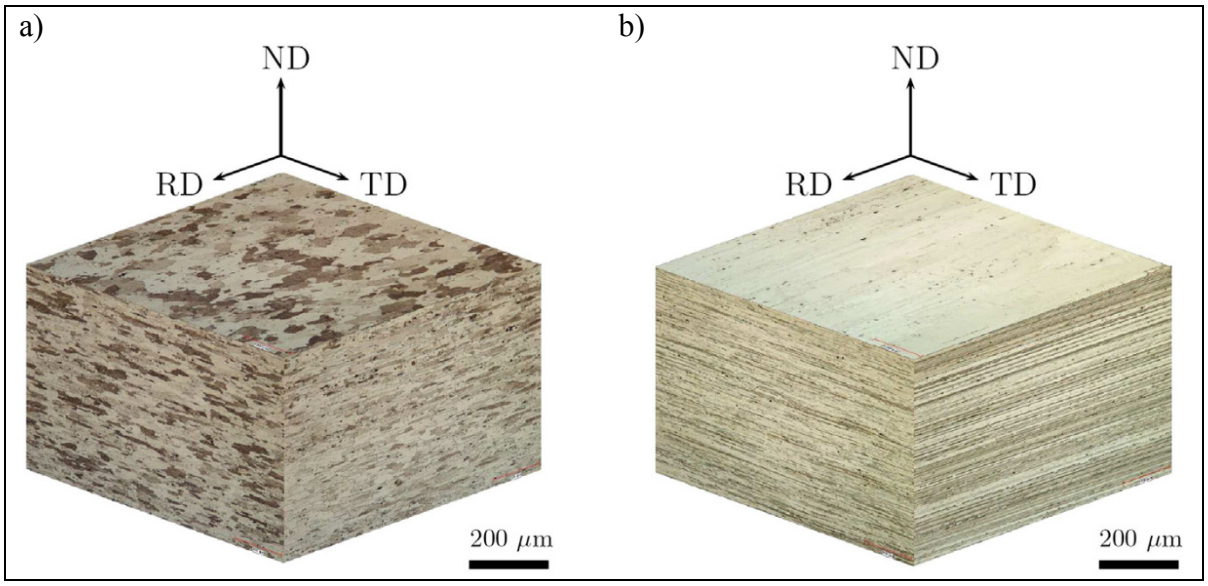

Figure 1.3 Three dimensional microstructures: a) AA2024-T3 , b) AA2198-T3 (Robe et al., 2015)

Zhang et. al. (S.-f. Zhang et al., 2014) have investigated the effects of ageing treatments on evolution of microstructure, properties and fracture of aluminum-lithium alloy 2198. In other words, they have compared T3 heat treatment condition with T8 heat treatment condition. T8 condition could be achieved by applying artificial aging on T3 conditions. They found out AA2198 has a considerable ageing response and its mechanical properties are very dependent to ageing temperatures due to different microstructures. Their characterization proved only the presence of $\delta'(Al_3Li)$ in naturally aged condition (T3) while high density of precipitates appeared after T8 heat treatment. The majority of these precipitates are $\delta'(Al_3Li), \theta'(Al_2Cu)\ and\ T1(Al_2CuLi)$. Their results show that higher aging temperatures increase the density of precipitates. The main precipitates are $\delta'(Al_3Li), \theta'(Al_2Cu)$ at aging temperatures under 160 ^{0}C. The dominant strengthening phase is $T1(Al_2CuLi)$ above 160 C. Fracture mode changes by increasing aging temperature from a typical dimple type to a mixed

of dimple and intergranular. Mechanical properties (yield strength, ultimate strength, elongation and hardness) variation of 2198 alloy at different ageing temperatures as a function of aging temperature have been measured in their research as shown in Figure 1.4. It is clear that the effect of T8 heat treatment temperature on tensile properties of 2198 alloy is significant. Compared with the data in T3 state, all tensile strength data in T8 state get significantly increased, indicating a strong ageing response of this alloy. The optimum values for having the highest yield strength and ultimate tensile strength are 175 ^{0}C and 14 hours of aging temperature and time, respectively.

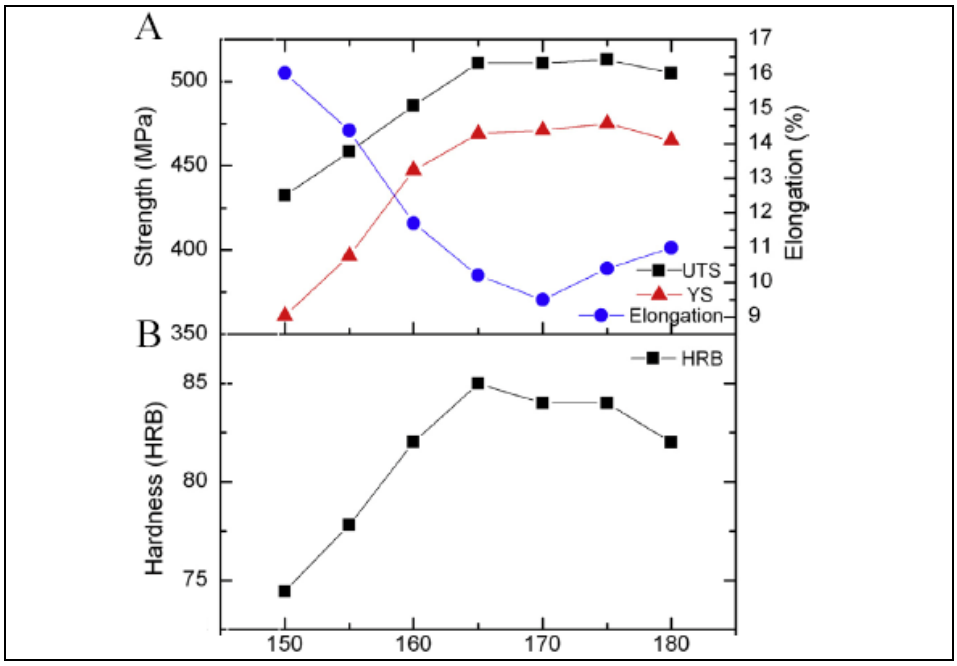

Figure 1.4 Mechanical properties variation of 2198 alloy at different ageing temperatures: a) Yield strength (YS), Ultimate strength (UTS) and elongation and b) Hardness as a function of aging temperature (S.-f. Zhang et al., 2014)

1.2 Friction Stir welding process

Friction stir welding (FSW) is a solid-state welding technique using a rotary pin to locally mix the materials of the two sides of the joint below the melting point temperatures. There is no melting of the base material so the possibility of the cracks and porosity from liquid is eliminated. Furthermore, there is no need for filler material (Guerra, Schmidt, McClure, Murr,

& Nunes, 2002; Shigematsu, Kwon, Suzuki, Imai, & Saito, 2003). FSW has been widely utilized to join difficult to weld aluminum alloys such as AA2××× and AA7××× series. It is currently used as an alternative to riveting for the assembly of airplane fuselages (Mishra & Ma, 2005). The heat source of FSW process is provided from tool rotation and its contact with part surface. Researches show that 86% of the heat needed to reach plasticity is obtained from friction between tool shoulder and part surface, the rest being a result of plastic strain and friction between pin and part. Figure 1.5 shows schematic of the FSW process (Sattari, Bisadi, & Sajed, 2012).

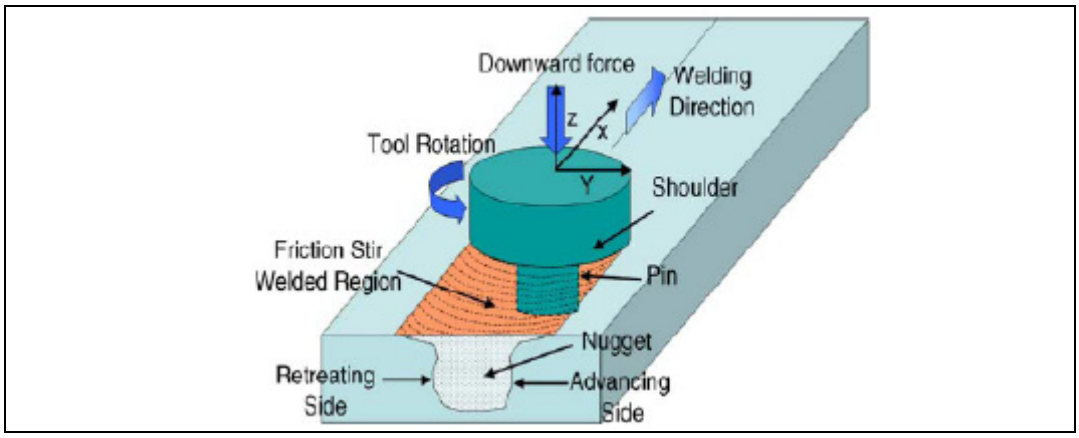

Figure 1.5 Schematic of friction stir welding process (Sattari et al., 2012)

1.2.1 Welding joint zones

FSW process creates four different zones in the joint as shown in Figure 1.6 which are completely different when compared to the joints created by fusion welding process (McQueen et al., 2013; Sattari et al., 2012).

(1) Nugget or stir zone, where dynamic recrystallization completely occurred. The friction between tool shoulder with workpiece surface causes higher temperature on the top of joint compare to the bottom of joint which could causes different grain size in joint.

(2) Thermo-mechanically affected zones (TMAZ) that are located immediately on each side of the nugget. TMAZ is subjected to thermal cycles is extremely deformed. The grains of TMAZ are stretched upward in parallel to the material flow. The applied plastic deformation on this zone is not enough for recrystallization process.

(3) Heat affected zones (HAZ) which is located adjacent to the TMAZ. It experiences a thermal cycle without mechanical deformation. This zone experiences temperatures which will effect on the precipitations process.

(4) The last zone is the unaffected base material.

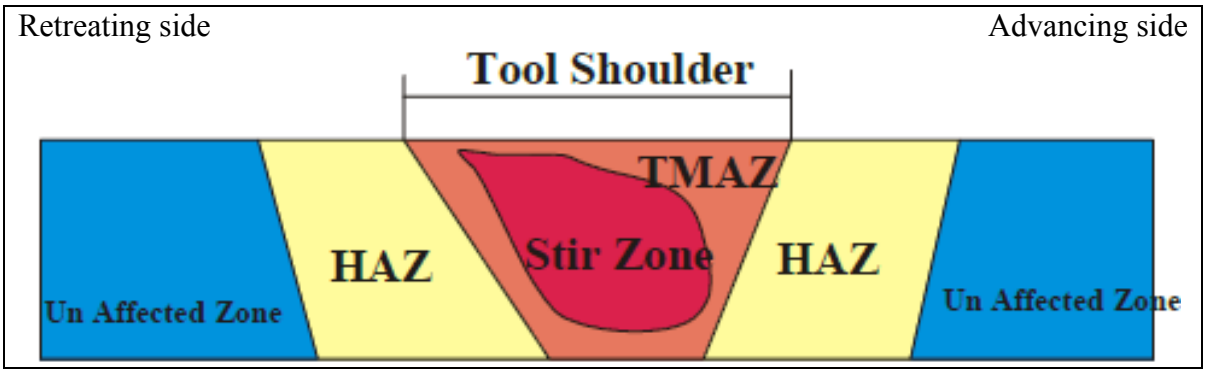

Figure 1.6 Different welding zones as a result of FSW process (Sattari et al., 2012)

1.2.2 Friction stir welding process parameters

Choosing the right parameters of FSW process is important for producing a defect free joint and generally the parameters selection is not a straightforward work, it needs experience and knowledge. The input parameters of FSW process and resulting output parameters are shown in Figure 1.7 (De Backer, 2014). The following section explain more details about the mentioned parameters in Figure 1.7, such as tilt angle, welding speed, plunge depth and etc.

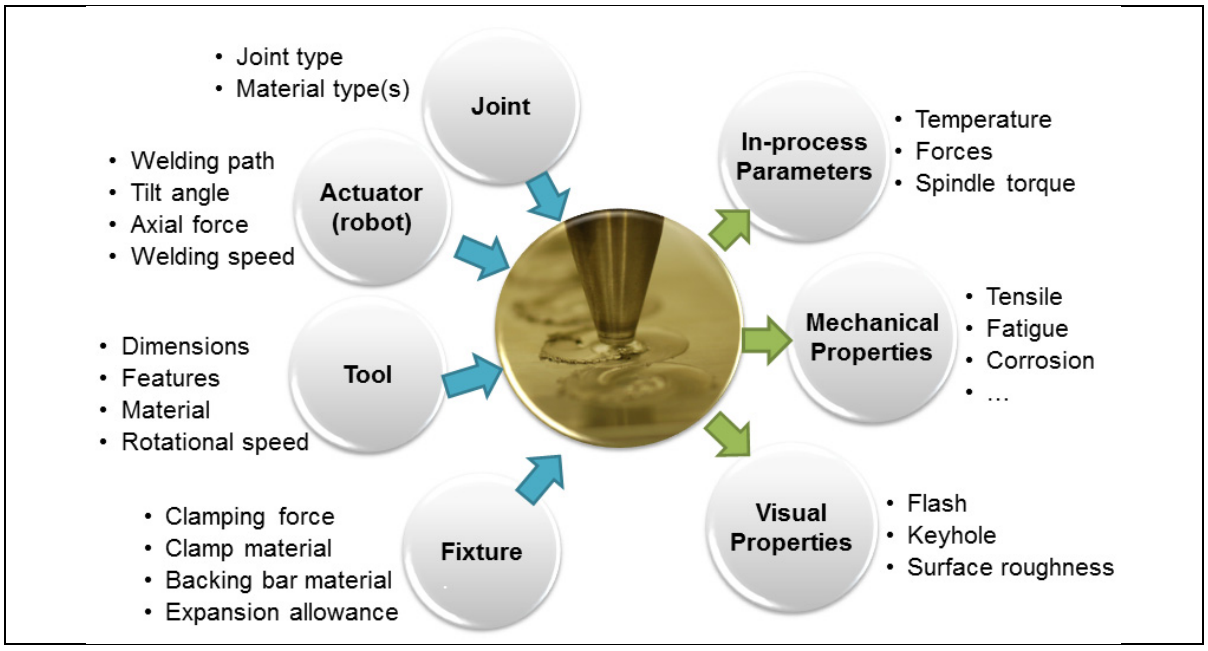

Figure 1.7 Input parameters affecting the FSW process and the resulting output parameters (De Backer, 2014)

1.2.2.1 Welding speeds

Rotational and traversal speed are two main parameters of FSW process. The material is stirred and mixed by rotation and forward movement of tool. Contribution of thermal cycle has higher importance compared to material flow for the precipitation evolution of second phase particles. Mishra et. al. (Mishra & Ma, 2005) proposed to estimate the heat input of FSW by the following formula.

$$Q = \frac{4}{3}\pi^2 \alpha \mu P R^3 \frac{\omega}{v} \tag{1.1}$$

Where Q is the heat input per unit of length and α, P, R and μ stand for heat input efficiency, pressure of tool on the joint, shoulder radius and friction coefficient, respectively. ω and v are the rotation and traverse speeds, respectively. It can be concluded that a relatively higher ω/v ratio can increase heat input so more metal around the pin can reach plastic state, flow and deform with the pin rotation, and then recrystallize. Therefore, the areas of the weld nugget and HAZ are relatively wider with higher ratio of ω/v (Ma, Xia, Jiang, & Li, 2013).

The following experimental relationship for calculation of average peak temperature (T) was proposed (Dixit, Mishra, Lederich, & Talwar, 2009).

$$\frac{T}{T_m} = K(HI)^A \tag{1.2}$$

$$HI = \frac{\omega^2}{v \times 10^4} \tag{1.3}$$

K and A are constants and they can be calculated from experimental results, T_m is the melting point of material. HI is heat index. There is a direct relationship between peak temperature as well as the duration of thermal cycle with HI. In other words, HI is an appropriate candidate for the depiction of average thermal profile during FSW. Generally, a cold weld is produced for HI <1.42 and generates worm hole defects in nugget; whereas, the hot cold has weaker mechanical properties (Dixit et al., 2009). Figure 1.8 shows an outline of the influence of process parameters on quality of weld, microstructure and mechanical. Highlighted region represents range of process parameters appropriate for FSW of Al-2024 (T3) alloy for attaining high tensile properties. It could be seen, combination of high traverse speed and low rotational speed produces a "cold weld" and it increases the possibility of worm hole defect (cavity). While, a combination of low traverse speed and high rotational speed produces a "hot weld" and it increases the grain and precipitates sizes (Dixit et al., 2009). The investigation of Dixit et. al. (Dixit et al., 2009) showed that heat index about 3.94 can produce a defect free joint of AA2024-T3 with highest tensile strength.

It should be noted that as the frictional coupling of tool surface with workpiece is governing the heating, it is not expected that the heating will monotonically increase with tool rotation rate, as the coefficient of friction at interface will decrease with increasing tool rotation rate (Song & Kovacevic, 2003). So, the heat input is not a simple linear function of welding speed parameters and FEM simulation is required for more precise prediction of peak temperature.

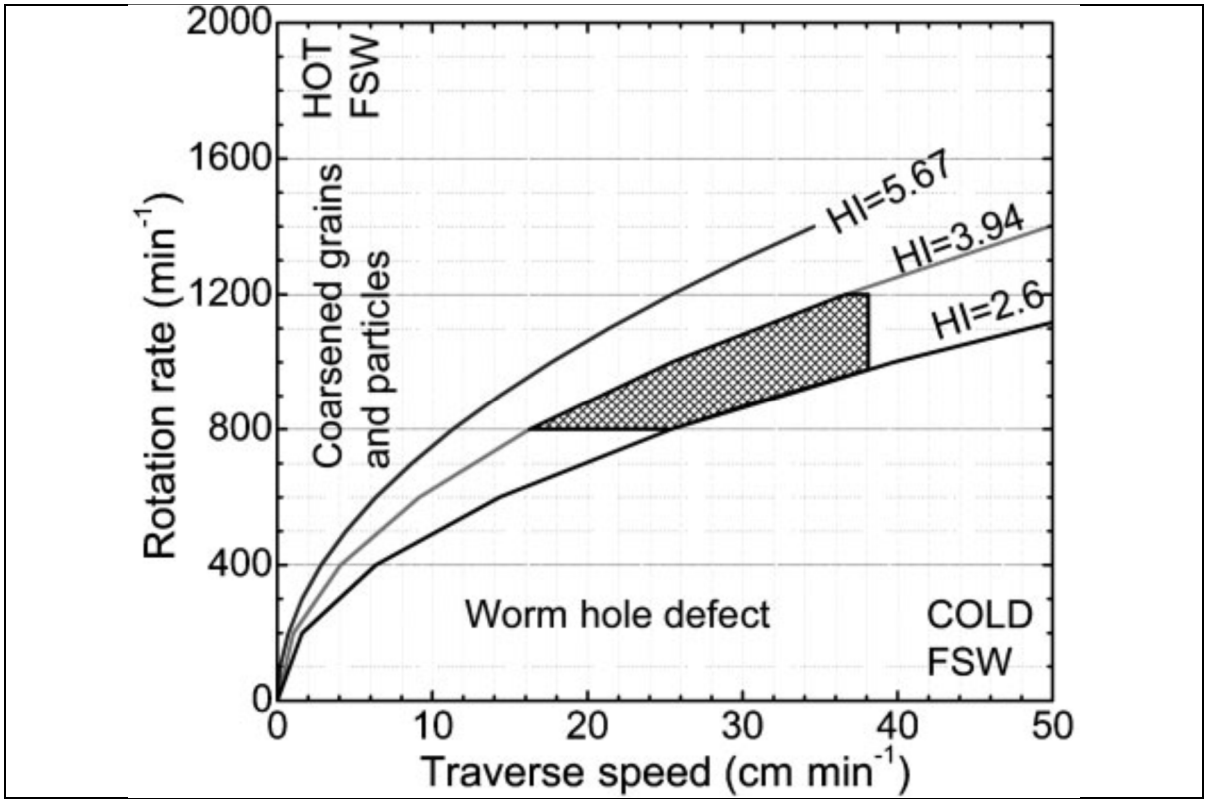

Figure 1.8 Process map of FSW for determining hot and weld cold conditions (Dixit et al., 2009)

Mastanaiah et. al. (Mastanaiah, Sharma, & Reddy, 2016) have investigated the effects of process parameters on material inter-mixing, defect formation, and mechanical properties of AA2219-AA5083 aluminum alloys joints. They have calculated the ratio between defect and joint surface versus tool rotation speed and tool traverse speed which can be seen in Figure 1.9. The area of defects increases at higher tool rotation speed and traverse speeds. They have explained that less shearing is required to transport softened material at higher temperature that causing considerable turbulence and resulting in defective welds.

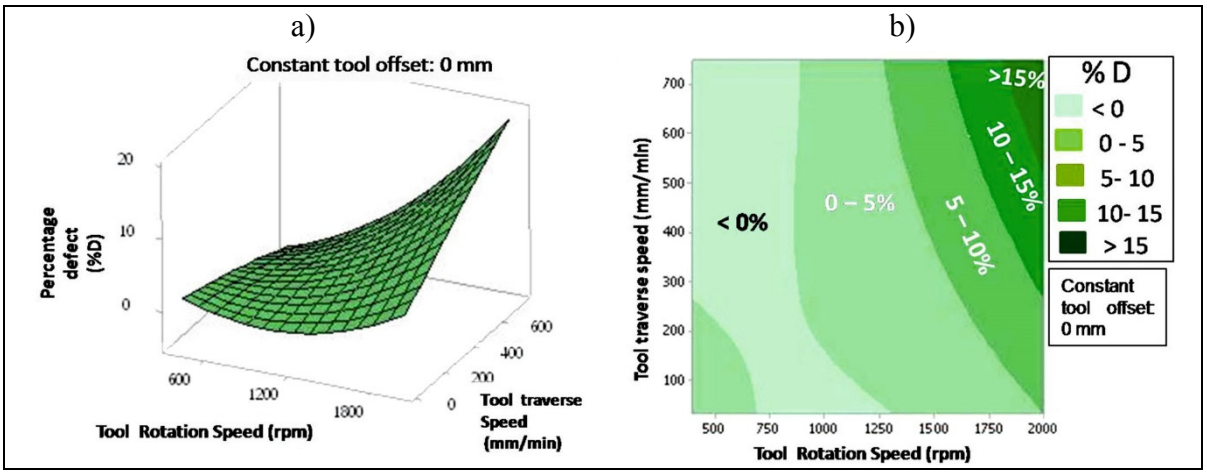

Figure 1.9 Percentage defect (%D) versus tool traverse speed and tool rotation speed: a) Surface plot and b) Contour plot (Mastanaiah et al., 2016)

The effect of the rotational speed, traverse speed were studied on dissimilar AA7075-AA6061 aluminum alloys joined by FSW (Hasan, Ishak, & Rejab, 2016) They used response surface methodology (RSM) with central composite design (CCD) for their experimental process to correlate welding properties and UTS. They found that the relationship of welding traverse speed and rotational speed with ultimate tensile strength presents an optimum value for each of them. Their results showed that 1100 RPM tool rotation speed, 300 mm/min traverse speed are the optimum value to create the stronger joint.

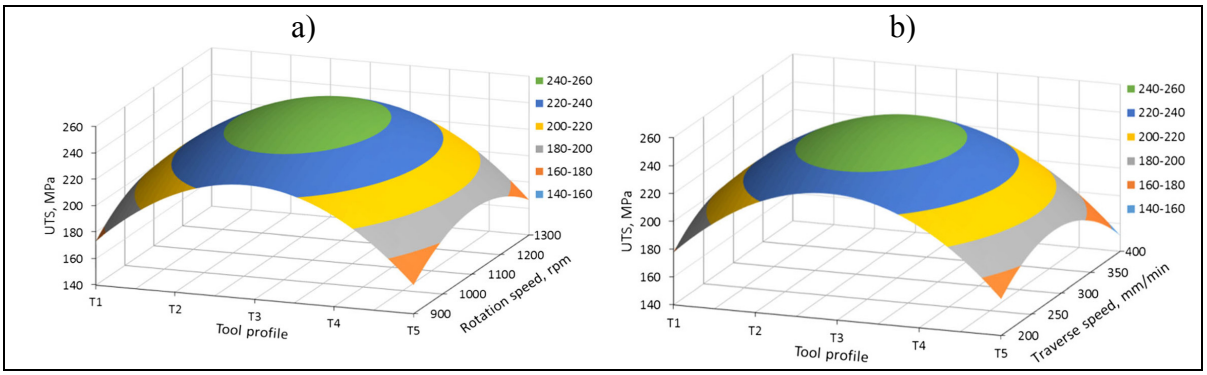

Figure 1.10 Response 3-D contour plots and clustered column showing the relation between the independent variables and the ultimate strength: a) rotational speed, b) traverse speed (Hasan et al., 2016)

Bitond et al. (C. Bitondo et al., 2010) studied the effect of FSW parameters on mechanical properties of AA2198-T3 joints and its optimization by a full-factorial experimental design using analysis of variance (ANOVA). They considered tool rotational speed and welding traverse speed as analysis factors and ultimate tensile strength (UTS) and yield strength (YS) for the response of their analysis. They observed that greater mechanical performance can be achieved by welds produced in cold conditions. UTS depends strongly on rotational speed and for lower value of rotational speed the greater values of UTS are achieved, while YS increases with weld traverses speed.

Bitond *et al.* (Bitondo, Prisco, Squilace, Buonadonna, & Dionoro, 2011) developed an empirical models based on regression analysis to predict FSW joint mechanical properties, as a function of the rotational and traverse speeds for rolled plates of AA2198 T3 aluminum alloy in particular yield and tensile strength. They did not investigate the metallurgical aspect of joints e.g. the defects such as JLR, kissing bond, tunneling cavity and microstructure of weld joint which is important for fatigue properties of material.

The advised parameters and the correspond optimum YS and UTS from difference researches for joining similar 2024 and similar 2198 FSW joint are shown in Table 1.5. It can be observed that the optimized rotational speed for joining AA2024 is approximately the same as the advised parameters for joining AA2198. The optimized traverse speed is lower for AA2024 than AA2198 and it can be a challenge for welding AA2198 to AA2024.

Table 1.5 Optimal welding conditions for 2198 and 2024 similar FSWed joint

Material	Optimize desirability	ω	v	YS	UTS	Reference
2198-T3	YS and UTS	500	300	252	354	(Bitondo, Prisco, Squillace, Giorleo, & Buonadonna, 2010)
2198-T3	YS and UTS	531	300	253	348	(Bitondo et al., 2011)
2198-T851	Flawless joint	1200	480	290	420	(Le Jolu et al., 2014; Le Jolu, Morgeneyer, & Gourgues-Lorenzon, 2010)
2024-T351	UTS	750	73	-	395	(Radisavljevic, Zivkovic, Radovic, & Grabulov, 2013)
2024-T351	UTS	750	93	-	355	
2024-T351	UTS	1180	116	-	398	
2024-T3	UTS	500	50	-	370	(Eramah et al., 2014)
2024-T351	YS	560	20	296	-	(Anil Kumar, Karur, Chipli, & Singh, 2015)
2024	YS and UTS	500	80	-	-	(Kasman, 2016)
ω= rotational speed (RPM), v=welding advancing speed (mm/min), YS=Yield strength (MPa), UTS=ultimate tensile strength (MPa).						

1.2.2.2 Tilt angle

The tool tilt angle with respect to the surface of workpiece is another welding parameter. An appropriate tilt angle ensures that the shoulder of the tool holds the surface material and moves it efficiently to the back of the shoulder. In most cases a tilt angle of about 3 degree is advised (Rai, De, Bhadeshia, & DebRoy, 2011; YN Zhang, Cao, Larose, & Wanjara, 2012).

1.2.2.3 FSW tool design

The FSW tool has the responsibility of localizing the heating and material flow. Furthermore, tool design governs the joint microstructure uniformity, mechanical properties and process loads, so its design is important (Mishra & Ma, 2005).

FSW tool composed of shoulder and pin as shown schematically in Figure 1.11. The pin of FSW tool can be fixed or adjustable. Another shoulder can be added to the tool in order to

cover the bottom of joint. This kind of tool with two shoulder is named bobbin tool. All of these tools are illustrated in Figure 1.12. (YN Zhang et al., 2012).

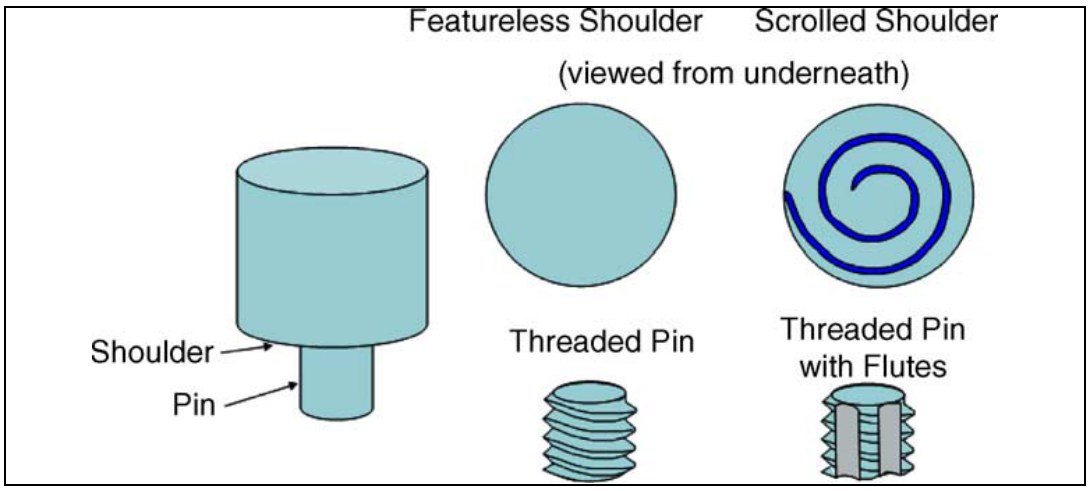

Figure 1.11 Schematic of the FSW tools (Mishra & Ma, 2005)

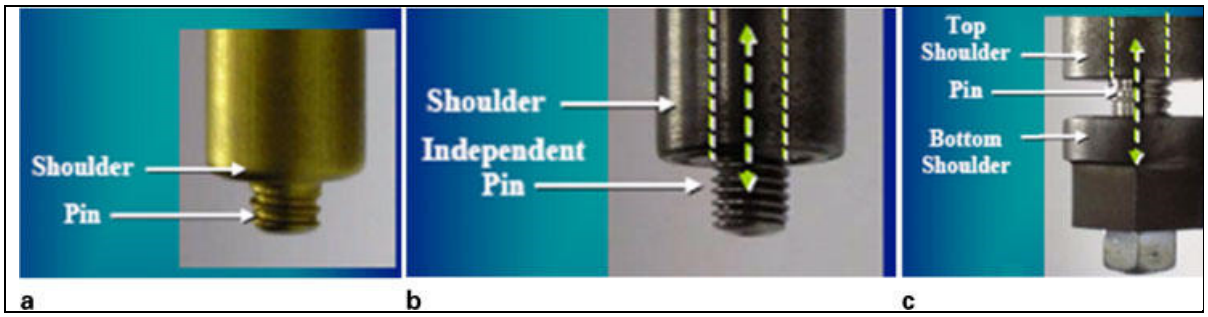

Figure 1.12 different types of FSW/P tools; a) fixed, b) adjustable and c) bobbin type tools (YN Zhang et al., 2012)

1.2.2.3.1 Pin profile

Salari et al. (Salari, Jahazi, Khodabandeh, & Ghasemi-Nanesa, 2014) studied the influences of different design elements such as combination of the conical and cylindrical pin, threaded pin, stepped pin on mechanical properties of AA5456 aluminum alloy in lap joint configuration by FSW process. Four different tool pin profiles were used as show in Figure 1.13. They have used a pin diameter equal to plate thickness. Tensile test showed adding stepped feature to the

pin can improve the mechanical properties while tool with triflute pin creates tunneling defect and shows the lowest mechanical properties. Furthermore, Shude et. al. (Ji et al., 2013) have showed a tool with a half-screw pin improves material flow behavior during friction stir welding and avoid root flaws. In both researches, changing of design in the middle of pin helps material flow in the mid thickness of the joint.

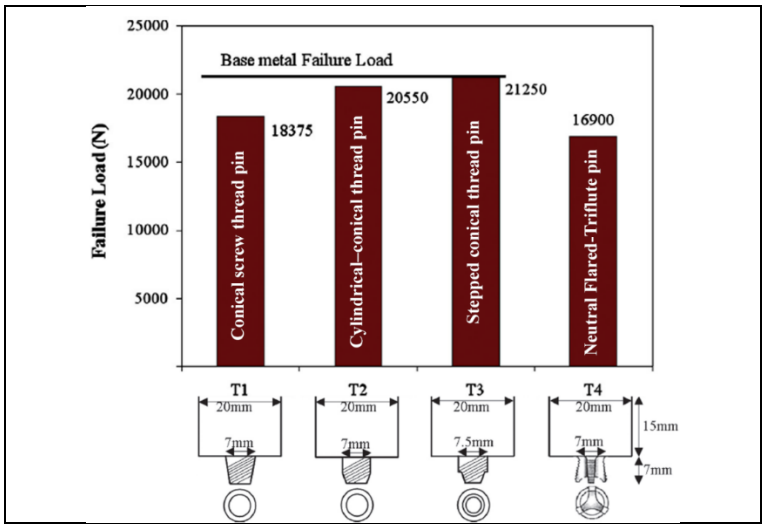

Figure 1.13 The effect of different tool designs on tensile tests (Salari et al., 2014)

Amirafshar *et. al* (Amirafshar & Pouraliakbar, 2015) have studied different designs of tool for joining ST14 structural steel and they have concluded that the cubic pins compared to cylindrical and conical pin create smaller nugget grain size and higher nugget hardness while cubic pin has the maximum tool wear. In a similar research (Mohanty, Mahapatra, Kumar, Biswas, & Mandal, 2012), aluminum joints manufactured with three pin designs as shown in Figure 1.14 were studied to find the best design. It was observed that use of a tapered cubic pin (trapezoidal) and tapered cylindrical pin instead of straight cylindrical tools does not necessarily improve joint mechanical properties for commercial grade aluminum alloys. Besides, tapered pin is less plunging force of the tool at the starting point of the process. The reason of no difference in mechanical properties is not mentioned clearly. In other research (Hasan et al., 2016), five tools with concave shoulders and different pin profiles (cylindrical and tapered, smooth and threaded, flatted and non-flatted) were used for joining AA7075-AA6061 aluminum alloys showing that the most influential factor on the tensile strength and

material mixing is tool design. Tool with tapered probe and additional features such as threads and flat can produce defect free weld with smooth surface finish, material mixing and high tensile strength. On the other hand, smooth cylindrical or even tapered pin result in poor material mixing which cause lower joint strength. They just mentioned the effect of tool design on ultimate tensile strength, so the effect of tool design on the joint yield strength, which is more important parameter for engineering application, is not clear.

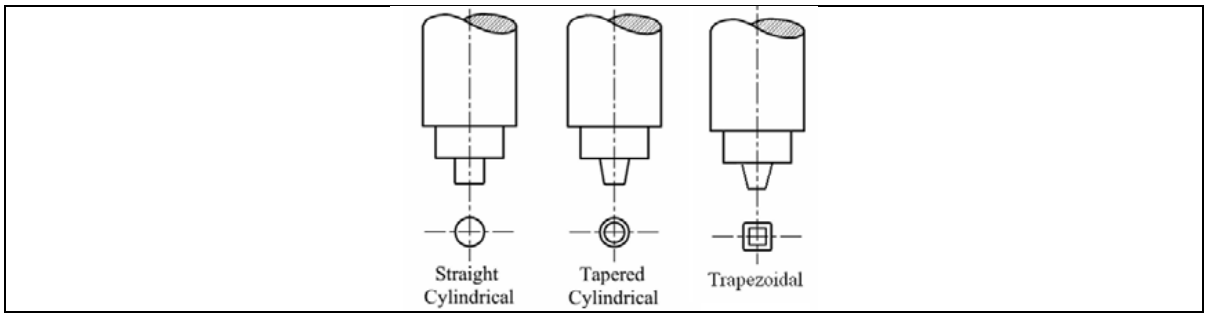

Figure 1.14 Different FSW tool geometries used by (Mohanty et al., 2012)

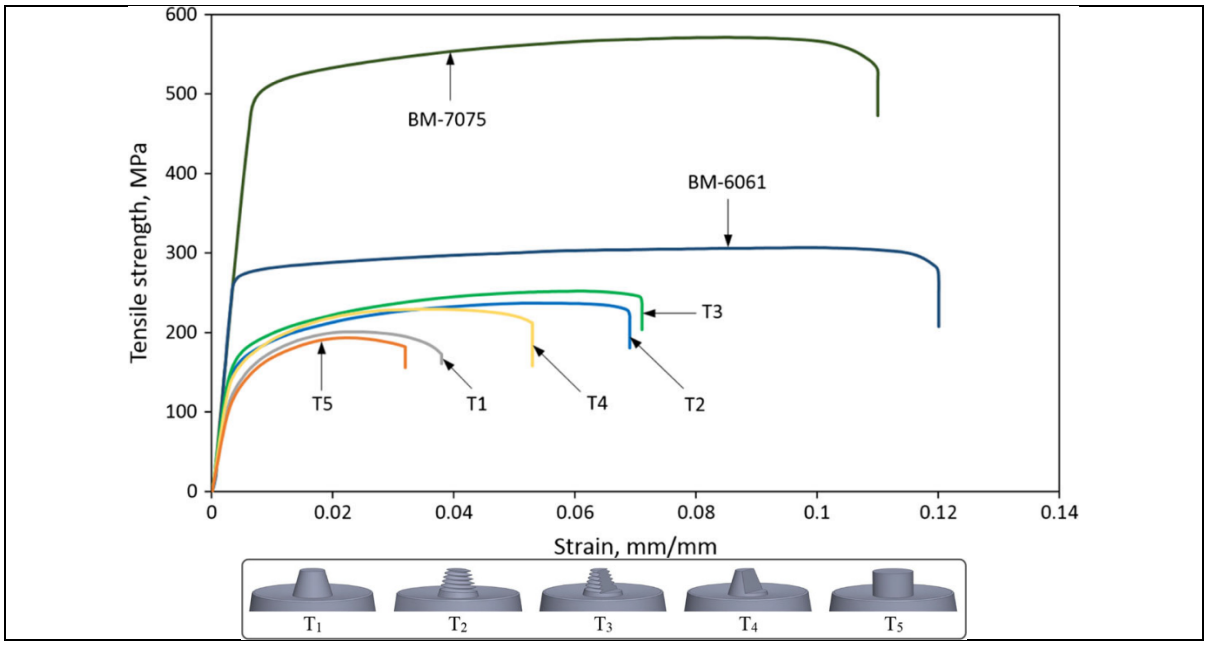

Figure 1.15 Stress–strain curves of the joints between AA7075-AA6061 using the five different pin designs such as cylindrical and tapered, smooth and threaded, flatted and non-flatted (Hasan et al., 2016)

1.2.2.3.2 Shoulder profile

There are three possibilities for shoulder design which are flat, convex and concave profiles. Concave shoulder profile feed the material into the tool shoulder cavity. Hence the concave surface serves as an escape volume or reservoir for the displaced material during welding. The proper, application of concave requires the tilting angle around 3 degrees. In the case of welding machine limitation for creating tilt angle, flat shoulder could be useful. The both flat and convex produces a lot of flash defect because they push the material away from the tool. In order to avoid the flash defect, excessive features such as scroll or groove could be useful. (YN Zhang et al., 2012).

Trueba et al. (Trueba Jr., Heredia, Rybicki, & Johannes, 2015) studied the effect of shoulder features on mechanical properties and surface finish of AA6061-T6 joint. They designed six different tool shoulders in order to improve the metal constraint and flow to the pin. Their shoulder designs had a fan shape could be recessed, raised or ramped in relation to the shoulder surface. Their studies proved that raised fan shoulder (tool C) have the maximum capability for manufacturing defect free welds with perfect finishing surface even under non-ideal welding parameters. Their shoulder designs, resulted finish surface and weld macrograph are shown in Figure 1.16. In similar research (Scialpi, De Filippis, & Cavaliere, 2007), the effect of different shoulder geometries (Figure 1.17) on the mechanical and microstructural properties of a friction stir welded 6082 aluminum joints were investigated. It can be seen, the shoulder with a cavity around pin has less flash defect and highest mechanical properties. However, more flash and low mechanical properties of the joint is related to the flat shoulder profile.

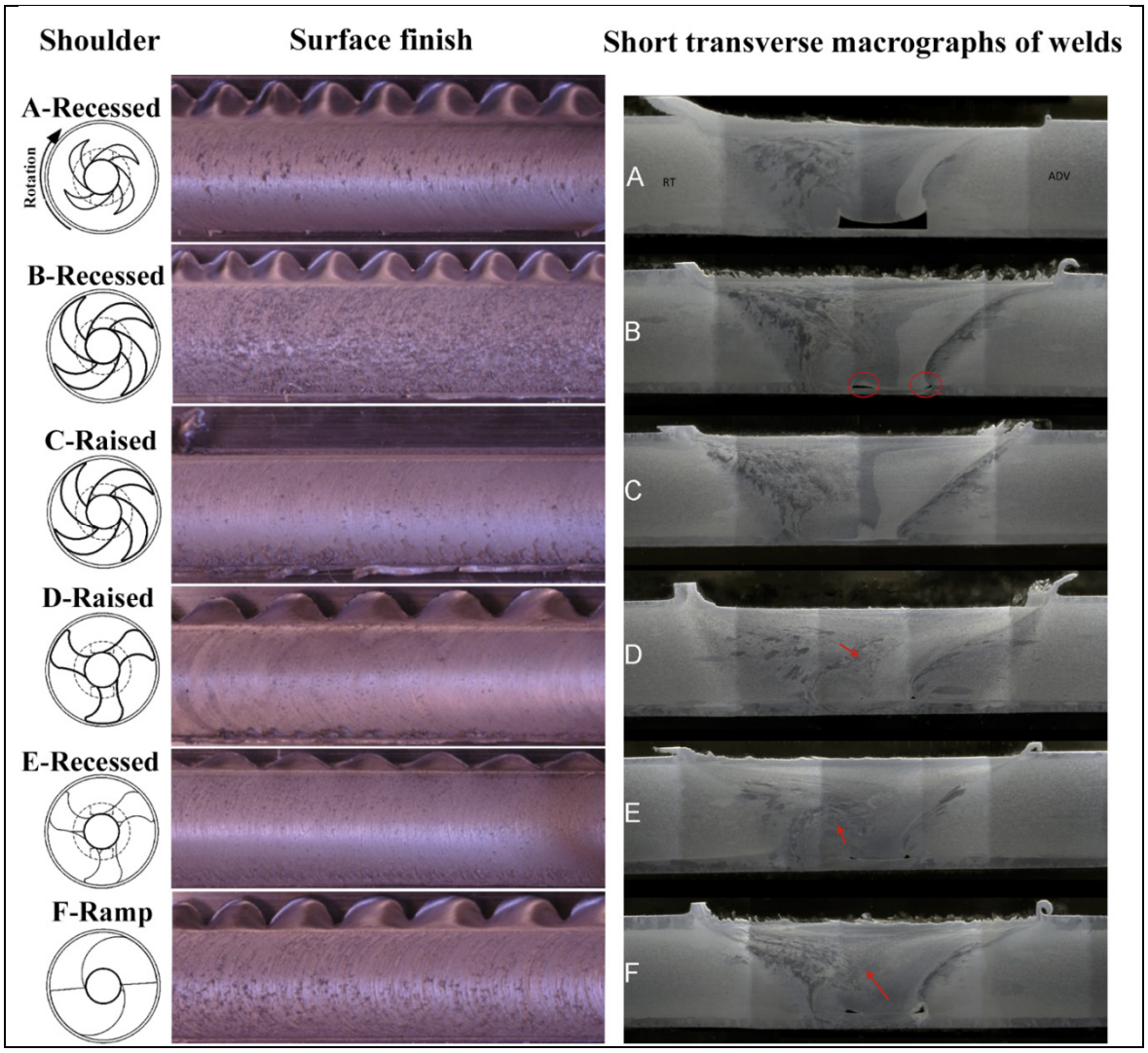

Figure 1.16 Effect of shoulder designs, resulted finishing surface and weld macrograph (Trueba Jr. et al., 2015)

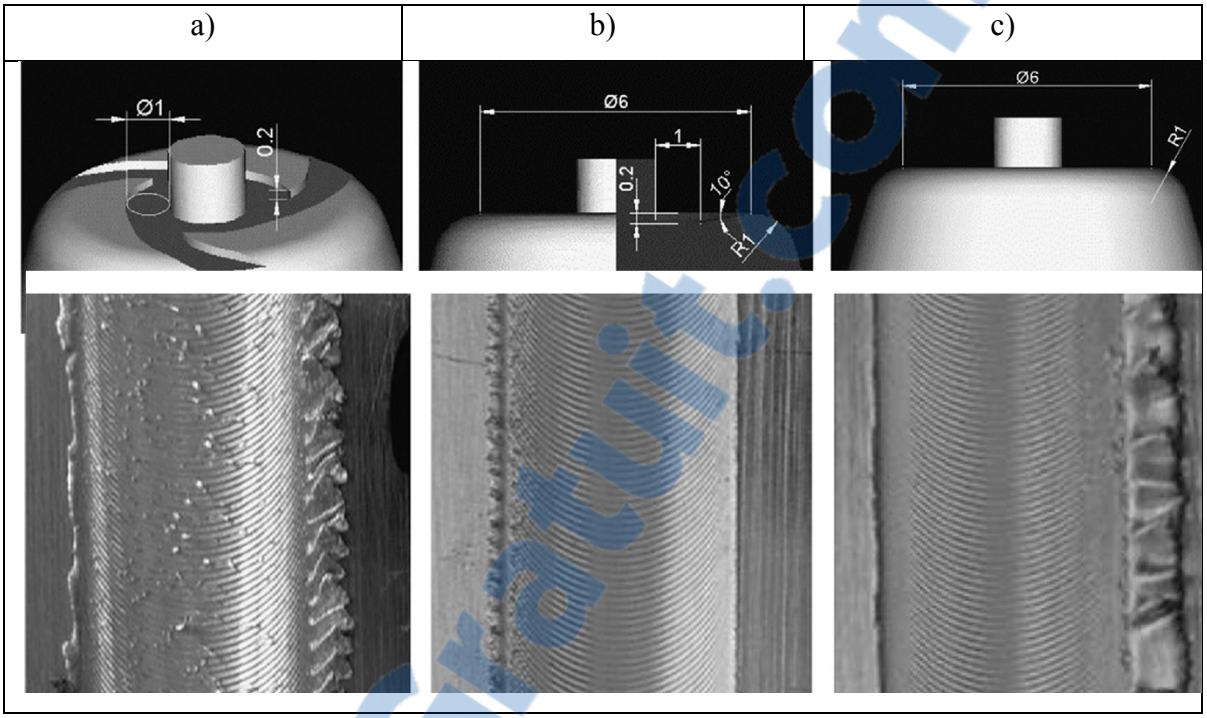

Figure 1.17 Different shoulder designs and resulted surface finish: a) recessed fan shoulder, b) shoulder with circular cavity around pin, c) flat shoulder (Scialpi et al., 2007)

1.2.2.3.3 Tool dimensions

The highest fraction of heat during FSW process is generated by the shoulder and the material should be sufficiently softened for flow by tool. Therefore, shoulder and pin dimensions are important (Rai et al., 2011). The following relationships for calculating the pin and shoulder diameter is proposed by Zhang et. al (YN Zhang et al., 2012) as a function of sheet thickness. They have proposed this formula on the basis of data collected from literature on 53 joints made from various materials includes Al, Mg, Cu, Ti, Ni and steel material.

$$Soulder\ diameter = 2.2 * \text{Plate thickness (mm)} + 7.3 \quad (1.4)$$

$$Pin\ diameter = 0.8 * \text{Plate thickness (mm)} + 2.2 \quad (1.5)$$

It can be seen, the thicker workpiece requires a larger shoulder for higher heat input generation which is required for moving larger material around pin.

Furthermore, recent research on the effect of shoulder to pin diameter ratio on microstructure and mechanical properties of dissimilar friction stir welded AA2024-T6 and AA7075-T6 aluminum alloy joints concluded that the optimum ratio between shoulder and pin diameter is around three (Saravanan, Rajakumar, Banerjee, & Amuthakkannan, 2016).

1.2.2.4 Plunge depth

The plunge depth of tool is important for creating defect free welds with flat shoulders. When the plunge depth is too low, the shoulder of the tool has not enough contact with the workpiece surface, Thus the stirred material cannot move well from the front to the back of the pin by rotating shoulder, resulting in generation of welds with surface lack of fill or tunneling defect. On the other hand, deep plunging creates excessive flash (Mishra & Ma, 2005). Kumar et. al. (K. Kumar & Kailas, 2008) studied influence of the tool plunge depth on the quality of FSW joints, they designed an experimental process where the plunge depth of the tool was continuously was increasing during FSW process . The normal force was measured during process and then the joint macrograph was obtained by metallography at different welding normal forces. Figure 1.18 shows the cross-sections of the joint produced at various tool plunge depth. The experiments showed that normal forces increase by increasing plunge depth. The defect size was reduced by increasing the tool plunge depth. Figure 1.18-f shows normal load higher than 7.4 kN can remove defects thanks to sufficient shoulder contact with the base material. Their study shows the importance of appropriate plunge depth and normal force.

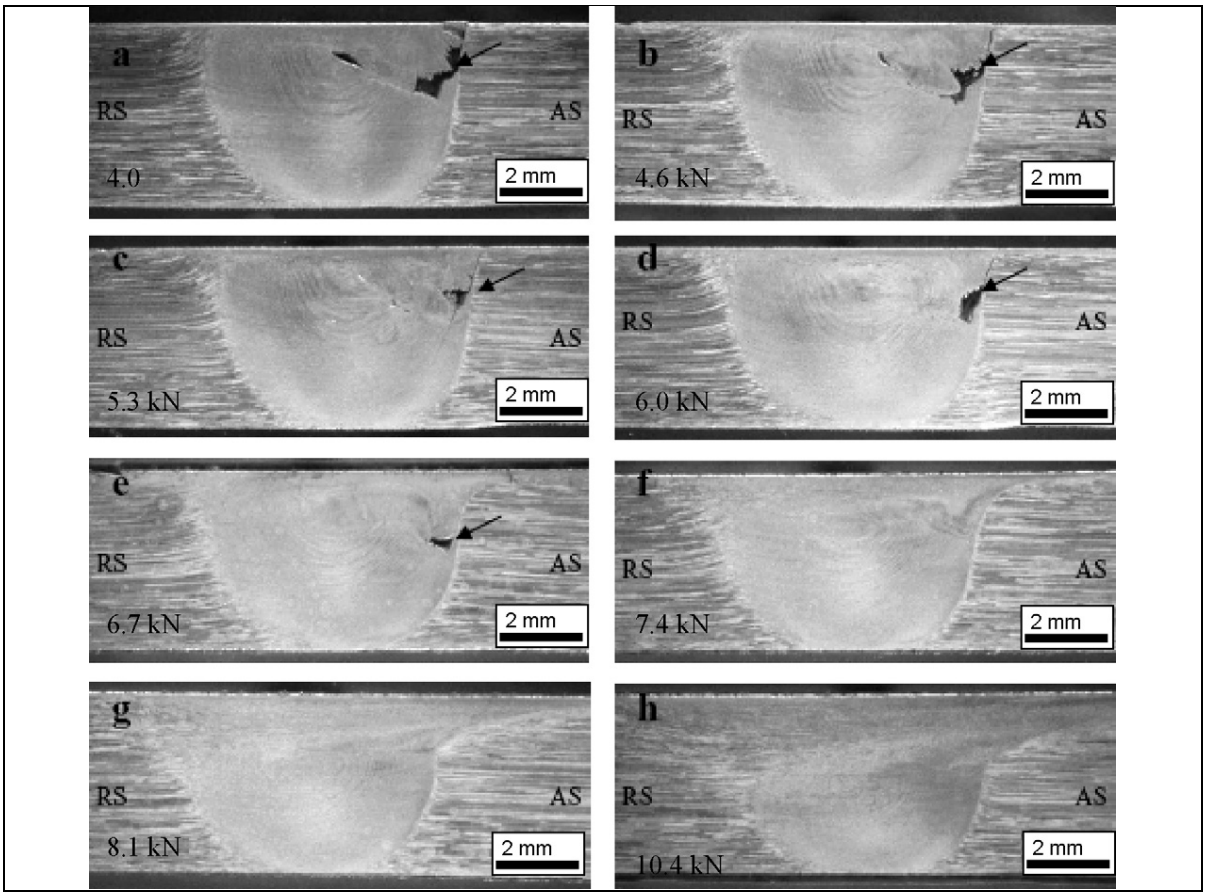

Figure 1.18 Development of weld defect free joint as a function of the shoulder interaction with the base material (K. Kumar & Kailas, 2008)

1.2.3 Friction stir welding imperfections

Imperfection is any deviation from the ideal weld, while defect is an unacceptable imperfection. Welding imperfections are classified according to ISO 6520 ("ISO 6520: Classification of geometric imperfections in metallic materials," 1998) while their acceptable limits are specified in ISO 5817 ("ISO 5817: Welding -- Fusion-welded joints in steel, nickel, titanium and their alloys (beam welding excluded) -- Quality levels for imperfections," 2014) and ISO 10042 ("ISO 10042: Welding -- Arc-welded joints in aluminium and its alloys -- Quality levels for imperfections," 2005). Both mentioned standards are applicable for fusion welding processes and most of defects in conventional welding processes are related to the solidification process. As the basis of FSW process is solid state material flow thus the nature of defects is different compared to the conventional welding processes (Mishra & Ma, 2005).

Most common defects of FSW process are shown in Figure 1.19. It is crucial to expand the knowledge boundaries about FSW process defects and their effect on joint mechanical properties.

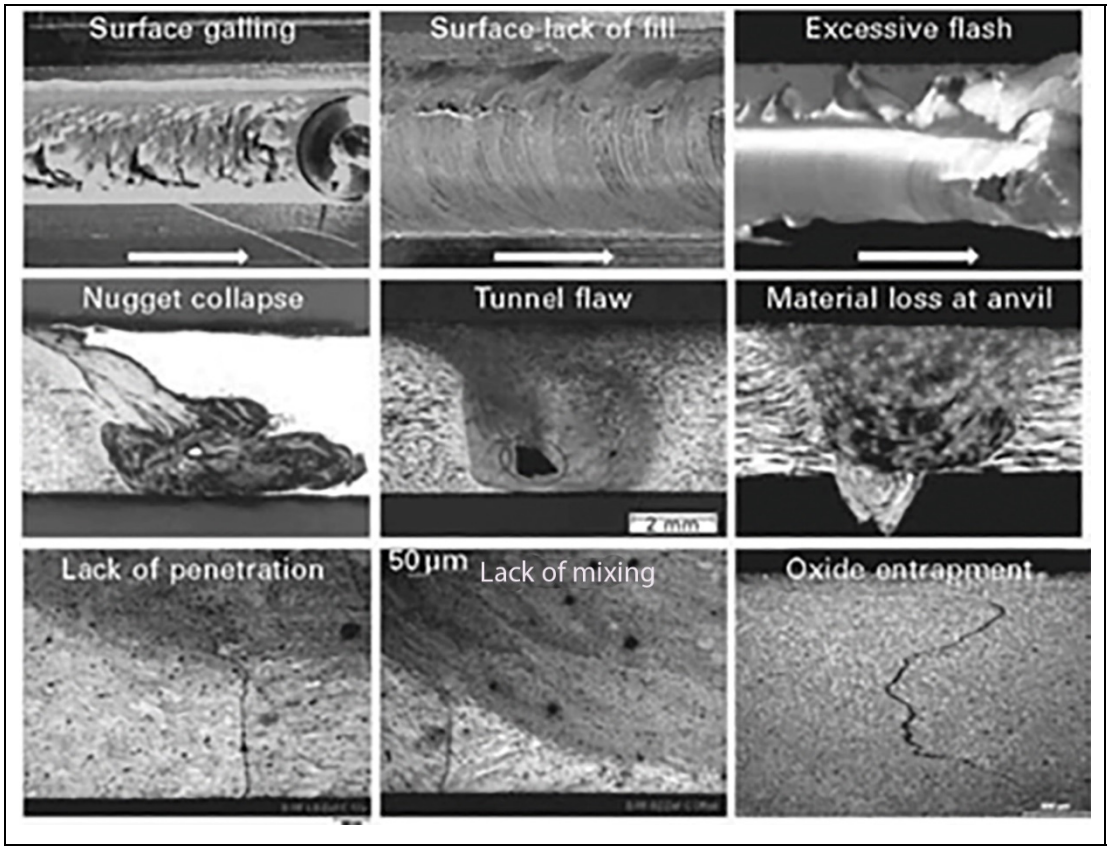

Figure 1.19 The most common defects of FSW process (Lohwasser & Chen, 2009)

Zhoe et al (Zhou, Yang, & Luan, 2006) have compared the fatigue strength of defect free FSW joints with defective joints containing joint line remnant (JLR or oxide entrapment in Figure 1.19) and kissing bond defects. They concluded that the fatigue strength of AA2024 flawed joint decreased by 55% compared to defect free joint. However, they used the published data for fatigue strength of defect free joints so their conclusion may be not accurate because the welding parameters of literature are different and maybe is related to deferent micro-structure due to different heat input history during FSW process. Jolu et al. (Le Jolu, Morgeneyer, Denquin, & Gourgues-Lorenzon, 2015) worked on effects of defects on fatigue lifetime and tearing resistance of AA2198 AL-Cu-Li alloy friction stir welds. In their research, four series

of FSW joints were prepared. (1) Bead on plate (2) FSW on two plates which creates JLR defect due to the surface oxide (3) FSW with short pin on two plates which creates JLR and Kissing Bond defect due to lack of penetration and (4) FSW on two plates with 0.7 mm gap between the plates with short pin which creates JLR, Kissing bond and cavity (Le Jolu et al., 2014) Their results showed that kissing bond and JLR have not a significant effect on fatigue properties but the joints with a gap cause a significant decrease of fatigue strength (about 30%) as shown Figure 1.21. The results have a good agreement with Kadlec's research (Kadlec, Růžek, & Nováková, 2015) who worked on FSW of AA 7475 FSW joint. Also Kadlac (Kadlec et al., 2015) have found kissing bond and JLR do not affect significantly the tensile strength and yield strength but these defects decrease the elongation especially in specimens where the crack initiation site is the kissing bond. This result is in agreement with the result of Jolu et al. (Le Jolu et al., 2015) shown in Table 1.6.

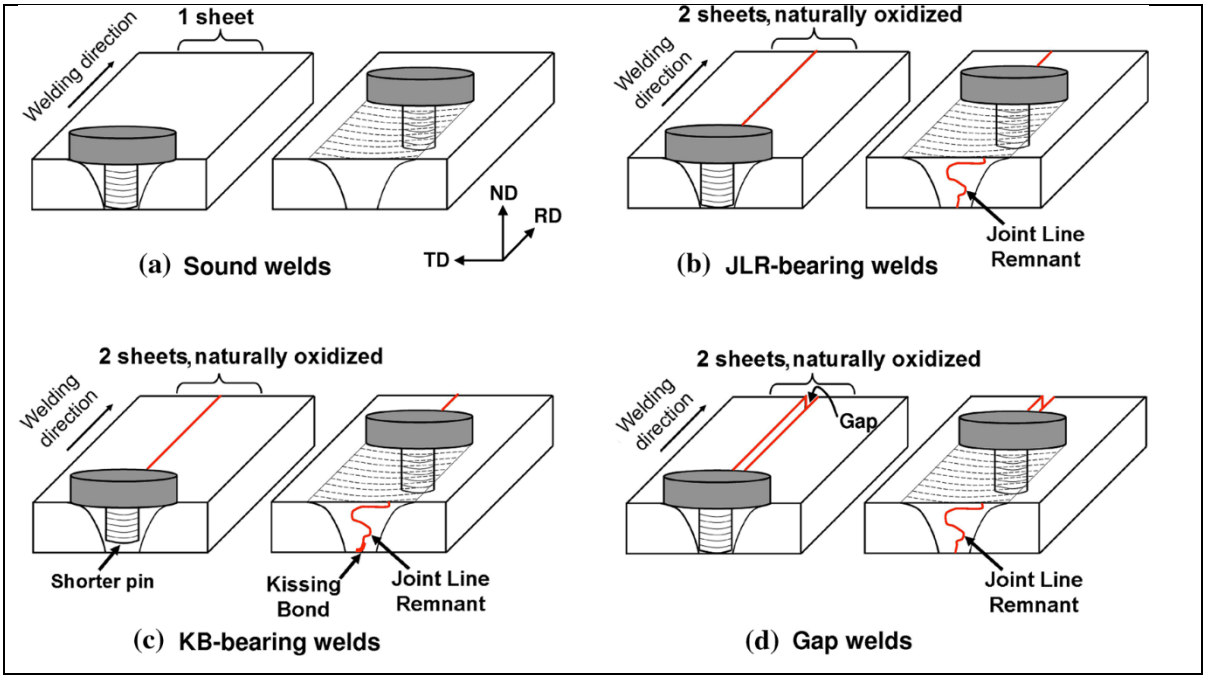

Figure 1.20 Schematic drawing of (a) ''sound'' welds, (b) welds bearing a joint line remnant, (c) welds bearing a kissing bond, (d) welds with a gap left between the parent sheets (Le Jolu et al., 2014)

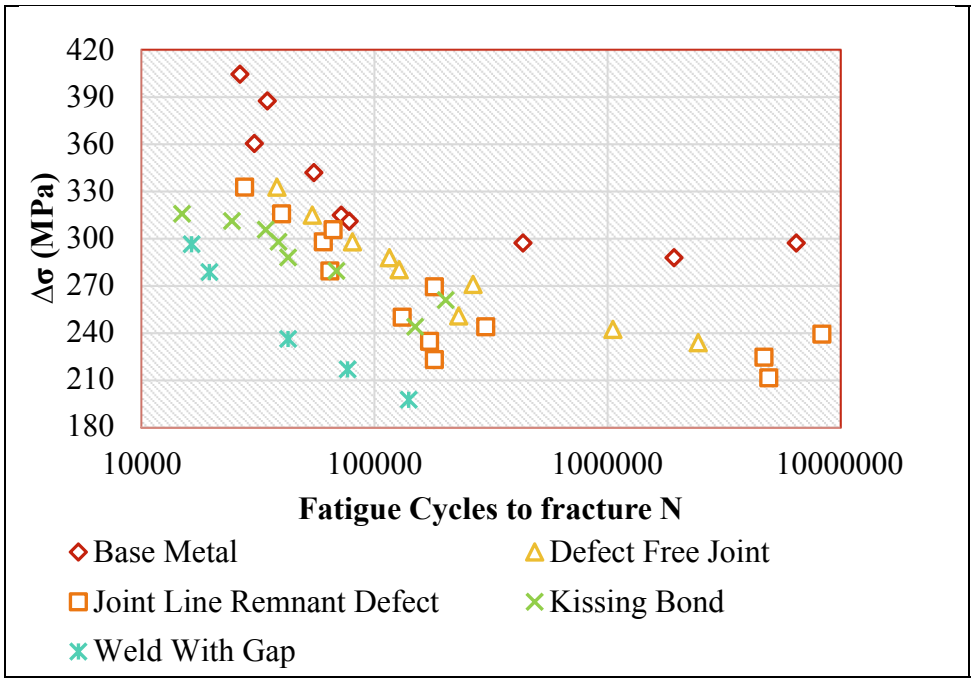

Figure 1.21 The fatigue strength of AA2198 base metal, defect free joint, and joints contain different defects (Le Jolu et al., 2015)

Table 1.6 Tensile properties of the welded joints and 2198-T851 base metal in different direction (Le Jolu et al., 2014)

	YS (MPa)	TS (MPa)	Elongation	Efficiency Ratio	Fracture Locus
Base metal (TD)	470	515	10.0	-	-
sound	282 to 302	412 to 429	19.5 to 22.4	80 to 83	TMAZ (RS)
JLR-bearing	285 to 296	413 to 416	15.7 to 17.5	80	TMAZ (RS) in two cases, TMAZ (AS) in one case
KB-bearing	265 to 287	398 to 410	14.2 to 19.5	77 to 80	weld nugget, starting from KB
Gap0.7	277 to 281	398 to 399	14.8 to 15.4	77	weld nugget, starting from ‘‘sensitive GBs’’

1.2.4 Characterization of AA2198 to AA2024 joint

Microstructural and mechanical characterization of AA2198-T3 and AA2024-T3 joint produced by FSW process, have been investigated by Robe et. al. (Robe et al., 2015). The joint macrograph is shown in Figure 1.22. It can be seen that the nugget is divided into two different zones by S shape border. It was observed left side of S shape border (AA2024-RS) has smaller grain size compare to right side (AA2198-AS). Besides, EDS analysis showed the difference in the magnesium content of the two sides on the border, proving that the nugget is non-mixed. It means a special tool design for a complete mixing between AA2024 and AA2198 is required.

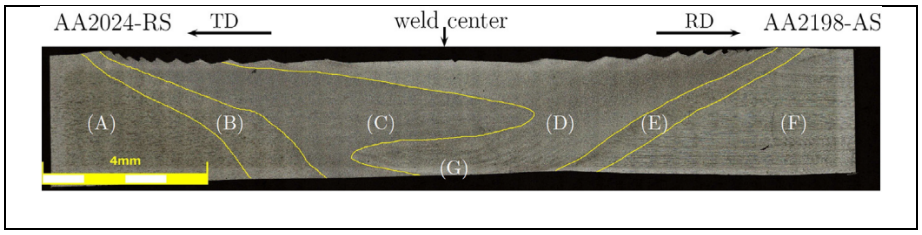

Figure 1.22 The macrograph of joint between AA2198 and AA2024 with higher magnification of different zones (Robe et al., 2015)

In another research (Texier et al., 2016) on the same joint (AA2198-T3 to AA2024-T3), the near surface mechanical heterogeneities of weld has been investigated in CWD-WD plane (Figure 1.23) within the nugget region. The banded microstructure is disappearing by going from top to bottom in normal direction (ND) due to the reduced effect of the shoulder. The band distance along welding direction (WD) is equal to the tool movement in welding direction per tool revolution. This banded structure is not the fracture origin in tensile test, but it could make a weakness point for fatigue strength. The fatigue properties of joint are not examined in the mentioned research.

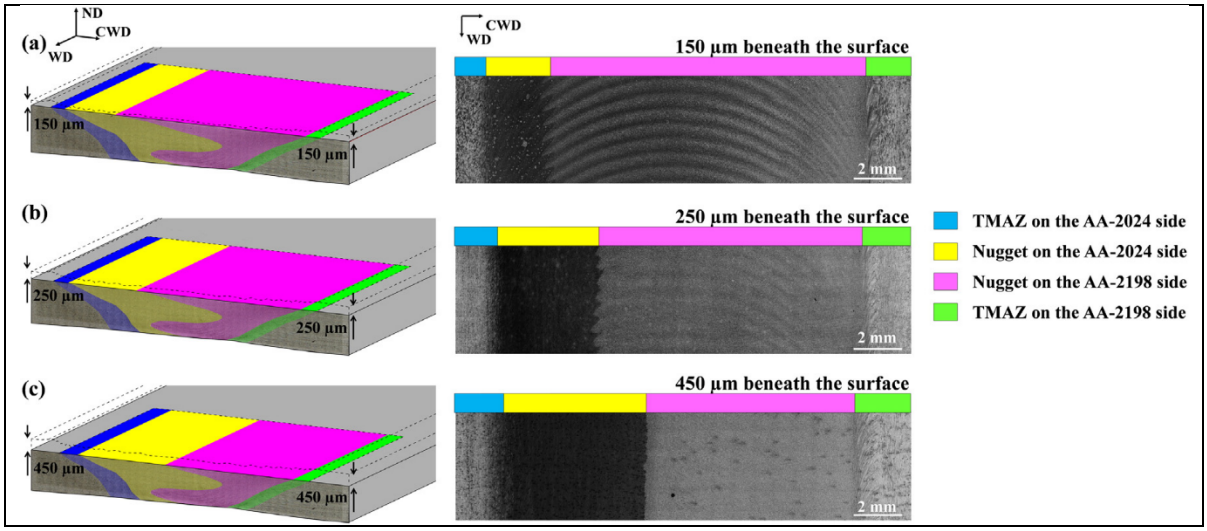

Figure 1.23 Macrograph of the dissimilar joint at various CWD-WD sections showing the presence and the vanishing of banded macrostructures: (a) at 150 µm underneath the top surface, (b) at 250 µm underneath the top surface, (c) at 450 µm underneath the top surface (Texier et al., 2016)

Hardness map of the surface at the top of the weld is shown in Figure 1.24. The minimal hardness is located out of the nugget region on the advancing side at the TMAZ region (AA2198) which is fracture location. Also, digital image coloration (DIC) measurement shows strain localization is located at crack location (Robe et al., 2015). So, special consideration should be taken for AA2024 and AA2198 joint, in order to solve the low hardness problem of AA2198 at advancing side e.g. post weld heat treatment to recover the loss of mechanical properties of AA2198.

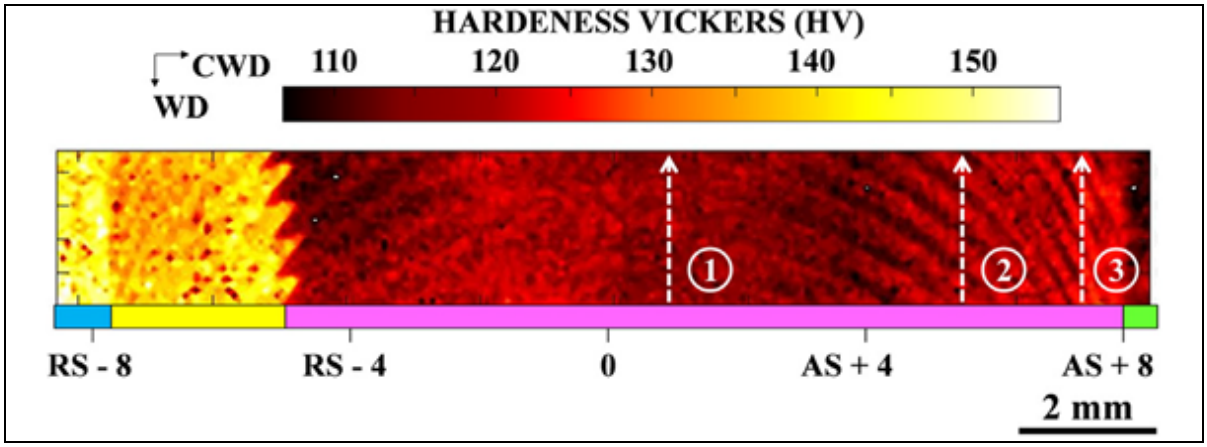

Figure 1.24 Hardness map of the surface showed in Figure 1.23-b (Texier et al., 2016)

1.3 Base metal heat treatment and post weld heat treatment

Many researches on FSW joints showed that the elongations of as-welded joints are only between 20 to 40% of the base metal elongation (Hu, Yuan, Wang, Liu, & Huang, 2011). Using post weld heat treatment (PWHT) could be effective for improving joint mechanical properties. The PWHT can be solution heat treatment and then precipitation or just aging treatment in order to recover the loss of mechanical properties in the joint zone. A few studies on the PWHT of FSW aluminum alloys such as dissimilar joint AA2024 and AA 7075 or similar joint such as 7449 , 6061-O , 2219-O and 2024-T4 showed that the PWHT recovered a large portion of the lost strength in the nugget, but it comes with loss of ductility (Hu et al., 2011; Muruganandam, Raguraman, & Kumaraswamidhas, 2015). The investigations have proved that the fine recrystallized grains of nugget are instable and they become coarse grain structures after PWHT through abnormal grain growth (AGG) (Aydın, Bayram, & Durgun, 2010; Charit & Mishra, 2008; Sullivan & Robson, 2008).

The selection of heat treatment cycles for aluminum alloys depends on the predefined requirements of the aeronautical structures. T3 (solution heat treated, cold worked, and naturally aged) and T8 (Solution heat treated, cold worked, and then artificially aged) are two common heat treatment for aluminum alloys (Hunsicker, 1984). The mechanical properties of AA2024 and AA2198 in both T8 and T3 heat treatment condition is reported in Table 1.7. It can be seen that T8 condition is more appropriate for higher strength application than T3 condition due to higher values of yield strength. It should be noted that applying artificial aging after cold work for T8 heat treatment is expensive.

Table 1.7 Tensile mechanical properties of 2024 and 2198 aluminum alloys (Alexopoulos et al., 2013; Srivatsan, Vasudevan, & Park, 2007).

Material	Heat treatment	YS (MPa)	UTS (MPa)	Elongation (%)
AA2024	T3	391	500	19
	T8	445	476	9
AA2198	T3	315	375	15
	T8	469	510	14

AA2198 in T8 heat treatment condition has been used for aircraft fuselage/pressure cabins (Pieta, dos Santos, Strohaecker, & Clarke, 2014). In these applications, it is possible to use T8

heat treated plates and then join them by FSW process. The disadvantage of this method is the possible loss of strength in the joint area due to the high temperature of welding, which causes fracture at the TMAZ/HAZ regions of FSWed joints. In the case of dissimilar joints, this method has the advantage of applying special designed heat treatment cycle for each material. Another option is applying T8 heat treatment after welding or post weld heat treatment (PWHT). PWHT can only be a solution heat treatment and then precipitation hardening or it can be just aging treatment in order to recover the loss of mechanical properties in the joint zone. The challenge is finding an optimum post weld heat treatment suits the non-homogenized weldments.

1.4 Summaries

The goal of this research is to manufacture a defect free joint between AA2198 and AA2024 materials. The next goal of this research is the improvement of the joint mechanical properties in order to make it reliable for aerospace applications. Hence, frictions stir welding process could be used for joining of 3rd generation Al-Li alloys because it is a solid state welding process without fusion of base metal. Friction stir welding is sensitive to tool design and welding parameters for creating a reliable joint which is free of defect. It means tool design and welding parameters should be designed properly for joining of 3rd generation Al-Li alloys to conventional aluminum alloys. Wrong tool design causes welding defects such as flash, kissing bond and tunneling defects. On the other hand, inappropriate welding parameters causes low mechanical properties of the joint. The 3rd generation of Al-Li alloys are relatively new materials and there is not enough research about their appropriate FSW tool design. There is some information at literature about similar joints of 3rd generation Al-Li alloys. Also there is plenty of information about friction stir welding of conventional aluminum alloys. In contrast, there is a gap for optimized parameters of the joint between the 3rd generation Al-Li alloys to conventional aluminum alloys. This research is going to fill the existed gap of information about the appropriate tool design and right welding parameters of FSW for joining of AA2198 to AA2024. In the light of the fact that the last generation of aluminum alloys is relatively new materials and specifically AA2198 has a good response to aging heat treatment; according to the authors' knowledge, no research on the heat treatment of dissimilar AA2024

and AA2198 joints has been reported in the open literature. So, the effect of PWHT on mechanical properties of AA2198 to AA2024 is going to studied in the current research.

CHAPTER 2

EXPERIMENTAL PROCEDURES, MATERIALS AND METHODS

2.1 Introduction

FSW is currently used as an alternative to riveting for the assembly of airplane fuselages (Mishra & Ma, 2005). However, defects can be found in the FSW joints, such as flash, tunneling, and kissing bond (Lohwasser & Chen, 2009). The key point to produce reliable joints by FSW process is to concurrently select appropriate welding tool and process parameters (Mishra & Ma, 2005). On the other hand, high strength joints are necessary for aerospace industry. Post weld heat treatment can recover the loss of mechanical properties in the joint area. The goal of this chapter is to describe the experimental process for tool selection, FSW parameters optimization and post weld heat treatment of the joint between AA2024 and AA2198.

2.2 Tools and fixture designs

A specific fixture was designed to assure the repeatability of the friction stir welding process, as shown in Figure 2.1. The welding direction, the cross-weld direction and the normal direction are denoted WD, CWD and ND, respectively. Stoppers, supporters, and clamps have been used to fix the plates in the directions WD, CWD, and ND respectively. Clamps and supporters are equipped with screws so they apply opposite force to ND and CWD directions, respectively; while there is no need to apply force in welding direction due to presence of welding force. The manufactured fixture is shown in Figure 2.2.

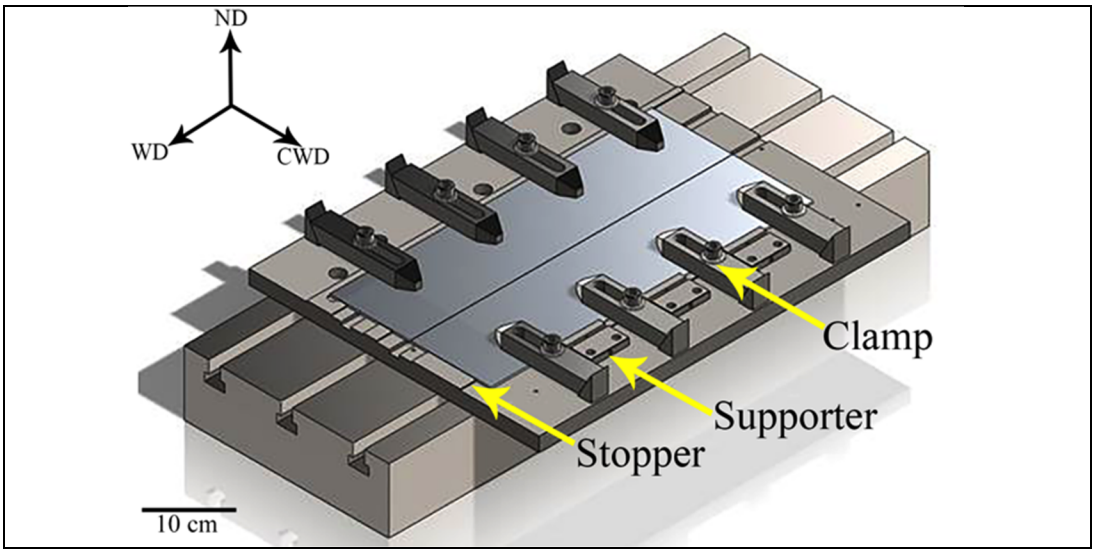

Figure 2.1 Fixture designed for the repeatability of the FSWed joints. The welding plate is fixed by stoppers, supporters, and clamps in the directions WD, CWD, and ND respectively.

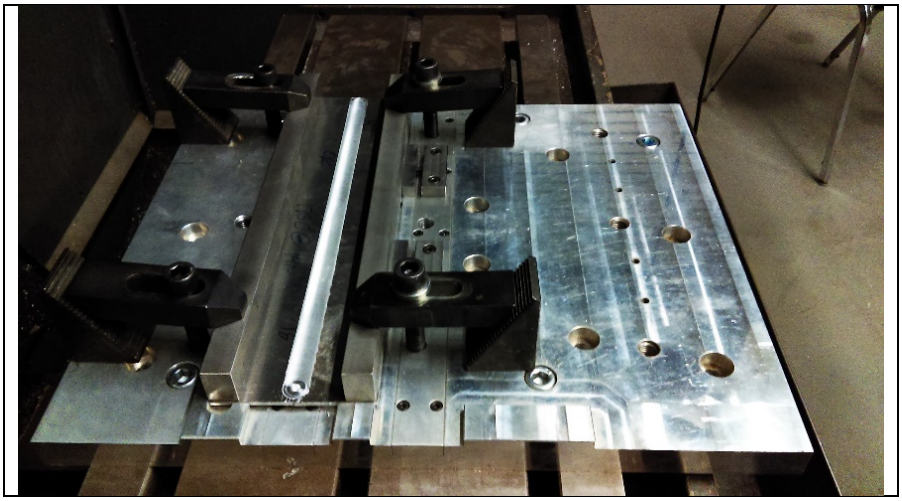

Figure 2.2 Manufactured fixture used for FSW process.

AISI 4340 steel hardened up to 49-HRC by quenching and tempering before machining, was selected for tool material as recommended by (YN Zhang et al., 2012). Seven tool configurations denoted from A to G in Figure 2.3 were designed and manufactured. Tool profile design for different tools has been chosen based on literature review, as shown in Table 2.1. The formulas for the calculation of the tool dimensions are shown in Table 2.2. It is worth

mentioning that tool F is a new tool design emerging from the combination of judicious tool features found in the open literature. The design of this new tool is a combination of conical and straight cylindrical pin concepts.

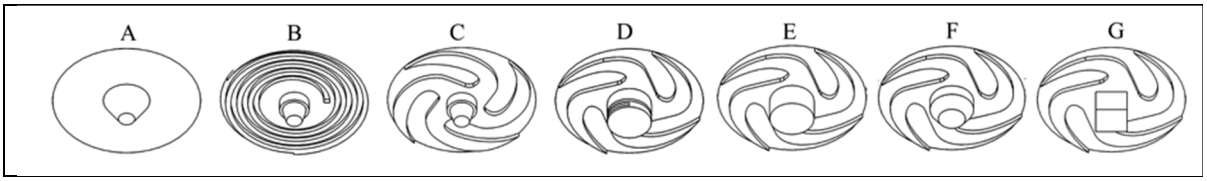

Figure 2.3 Design of the different tool configurations: (A) Flat shoulder with conical pin, (B) Raised spiral shoulder with stepped conical pin, (C) Raised fan shoulder with stepped conical pin, (D) Raised fan shoulder with threaded cylindrical pin, (E) Raised fan shoulder with cylindrical pin, (F) Raised fan shoulder with tapered cylindrical pin, (G) Raised fan shoulder with cubic pin.

Table 2.1 Selected tool profiles for the design of different tools.

Profile	Design	Tool
Shoulder profile	Flat shoulder (Mustafa, Kadhym, & Yahya, 2015)	A
	Recessed spiral shoulder (YN Zhang et al., 2012)	B
	Raised fan shoulder (Trueba Jr. et al., 2015)	C, D, E, F and G
Pin profile	Conical pin (K. Kumar & Kailas, 2008)	A
	Stepped conical pin (Salari et al., 2014)	B and C
	Half-screw pin (Ji et al., 2013)	D
	Straight cylindrical pin (Mohanty et al., 2012)	E
	New tool design	F
	Square pin (Amirafshar & Pouraliakbar, 2015; Elangovan & Balasubramanian, 2008; Kamble, Soman, & Brahmankar, 2012)	G

Table 2.2 Selected dimensions for FSW tool design (*PT = plate thickness = 3.2 mm).

Parameter	Suggested formula	Used value (mm)	Types
Tool Shoulder Diameter	2.2*PT (mm) + 7.3 (YN Zhang et al., 2012)	15.8	All
Pin length	Up to 0.3 mm smaller than PT (Meilinger & Török, 2013)	2.7	All
Max outer pin diameter	Equal to PT (Salari et al., 2014)	3.1	A, B and C
	0.8*PT (mm)+2.2 (YN Zhang et al., 2012)	4.7	D, E, F and G
Min-pin Diameter	0.5 * PT	1.6	A, B and C
	Equal to PT	3.1	F

The dynamic volume of a pin can be computed by it rotation around its axis e.g. rotation of tool G (cubic pin - diameter=4.7mm) around its axis generate the profile of tool F (cylinder pin - diameter of 4.7mm) as shown in Figure 2.4. The nugget size has direct relation with pin dynamic volume. Besides, The ratio between the real volume to dynamic volume of a pin defines the path for the material flow from the leading edge to the trailing edge of the rotating tool pin (Elangovan & Balasubramanian, 2008). So, calculating the real and dynamic volume of pin is helpful for material flow investigation and nugget size.

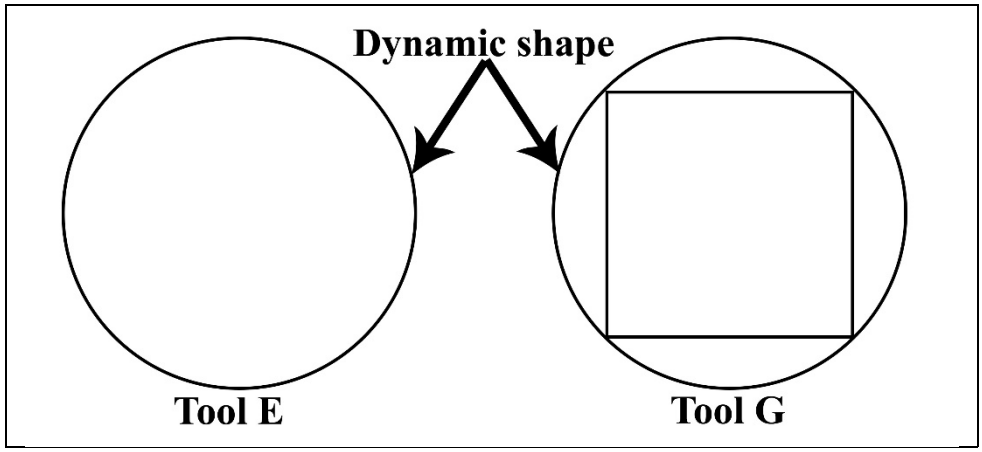

Figure 2.4 The dynamic shapes of tool E and G. The both tool have the same profile with same dimensions during tool rotation.

2.3 Base materials

Base materials AA2024-T3 and AA2198-T3 rolled sheets (thickness of 3.2 mm) were used in the present investigation. The nominal chemical compositions of these base materials are reported in Table 2.3. The microstructures of the two base aluminum alloys are already detailed in a previous study (Robe et al., 2015).

Table 2.3 Chemical compositions of AA2024 and AA2198 alloys in wt.% (Bussu & Irving, 2003; Chen, Madi, Morgeneyer, & Besson, 2011).

Alloy	Cu	Li	Mg	Ag	Mn	Fe	Zn	Si	Ti	Al.
AA2024	3.8-4.9	-	1.2-1.8	-	0.3-0.9	≤0.5	0.2	≤0.5	0.15	Bal.
AA2198	2.9-3.5	0.8-1.1	0.25-0.8	0.1-0.5	≤0.5	≤0.01	≤0.35	≤0.08	-	Bal.

2.4 Welding process

The first goal of the present study is to find appropriate tool geometry for friction stir welding of AA2024-T3 and AA2198-T3. To ensure that the mismatch between plates edges of AA2024 AA2198 do not affect the formation of defects within the joints and any defects present would only be related to the tool design, two series of weld were preliminary produced and investigated. First weld series were made by moving the tool into a seamless AA2024-T3 sheet (i.e. bead-on plate weld). On the basis of metallography and visual examinations of the first weld series (bead-on plate), tools that produce defect free joints were selected for the dissimilar welding of AA2024-T3 and AA2198-T3 plates. Then, the tool that could create a joint between AA2024 to AA2198 with highest yield strength, would be selected as the best candidate.

The bead on plate joins were done by constant welding parameters i.e. the rotation speed, the welding traverse speed, the plunge depth and the tilt angle were 750 RPM, 50 $mm.min^{-1}$, 0.2 mm, and 0 degree, respectively. These selected parameters are close to the parameters recommended in references (Anil Kumar et al., 2015; Bitondo et al., 2011; Ciro Bitondo et al., 2010; Kasman, 2016; Radisavljevic et al., 2013). In order to optimize the welding speeds for selected tool, the combinations of the traverse and rotational speeds used in the present study and their related sample codes are presented Table 2.4. This combination starts from low

traverse speed of 50 mm.min^{-1} in order to guarantee high temperature in the weld (hot weld condition) and complete mix of both base materials which may present different thermomechanical behaviors.

In this dissimilar configuration, AA2024 plates were placed on the retreating side (RS) with the weld direction parallel to the rolling direction (RD). On the advancing side (AS), the AA2198 plates were place with its transverse direction (TD) parallel to the welding direction. This configuration is chosen because both base metals have anisotropic mechanical behavior, the tensile properties of AA2024-T3 in transverse direction is comparable with AA2198-T3 in rolling direction. So, this configuration could maximize the joint efficiency in tension condition (Robe et al., 2015).

Table 2.4 Welding speed parameters.

Sample code	Rotational speed (RPM)	Traverse speed (mm.min^{-1})	Speed ratio (mm.rev^{-1})
F1	750	50	0.1
F2	750	150	0.2
F3	750	300	0.4
F4	750	450	0.6
F5	1000	300	0.3
F6	1000	450	0.5

2.5 Base metal heat treatment and post weld heat treatment

Aluminum alloys with T8 heat treatment condition is more favorable for higher strength applications than T3 condition. T8 condition could be achieved easily by applying artificial aging on plates with T3 conditions. The advised temperature and time for artificial aging of AA2024 are 463 K and 12 hours and for AA2198 are 448 K for 14 hours (Chandler, 1996; S.-f. Zhang et al., 2014). In this investigation, 448K and 12 hours have been selected as proper T8 heat treatment cycle for both base metals AA2024 and AA2198. The dissimilar joint between AA2024 and AA2198 were produced by FSW process (750 RPM and 50 mm/min, tool F) with base metals in T3 and T8 heat treatment condition. 12 samples were extracted from each condition. Subsequently, selected T8 post weld heat treatment applied on 4 welded samples in T3 condition. Other 4 samples in T3 condition were stretched 3% (locally for the

TMAZ area on the basis of DIC results) and then T8 heat treatment applied on them to achieve T851 condition. The used codes for samples are summarized in Table 2.5.

Table 2.5 The summarized codes and their discretion used for samples**.**

Condition	Code	Description
As-welded samples	AW-T3	As-welded samples in T3 heat treatment conditions
	AW-T8	As-welded samples in T8 heat treatment conditions
Post weld heat treated samples	PW-T8	T8 post weld heat treated samples
	PRPW-T8	T8 post weld heat treated samples after 3 % local strain

2.6 Sample preparation

The FSWed samples were prepared for metallographic observations with a standard polishing down to 1 μm diamond paste followed by BUEHLER Vibromet polishing for 48 hours with 0.05 μm colloidal silica solution. A Keller etchant was employed for 15 seconds to reveal the microstructure. Optical micrographs were obtained with an OLYMPUS Lext OLS4100 laser scanning confocal microscope. Tensile specimens were machined from the welded plates so that the loading direction was parallel to the cross-welding direction of the joined plates. Specimens were extracted both from the base materials to provide a reference and from the joints as specified in Figure 3-a (the joint being centered in the specimen gage). Tensile test were performed on dog-bone tensile specimens with the geometry displayed in Figure 2.5-b. Tool plunging into material surface creates sharp edges which are stress concentration sites (Masoumi, Zedan, Texier, Jahazi, & Bocher, 2016); All tensile samples were consequently polished to remove the surface defects. Tensile tests were conducted on a 5kN Kammrath & Weiss micro-tensile device at a constant crosshead displacement rate of 7 $\mu m.s^{-1}$. The specimen elongation along the loading direction was continuously recorded using a Keyence LS-7030M optical extensometer, measuring the displacement in the region between the two TMAZ regions (L_0=16 mm). Tensile tests were repeated three times for each welding condition. In parallel, *in-situ* optical microscope tensile tests were conducted for different loading conditions to evaluate the local strain fields via optical high resolution-digital image correlation technique (OHR-DIC), as explained in (Texier et al., 2016). Optical micrographs were taken with an OLYMPUS DSX-500 optical microscope in an unloaded state to investigate the irreversible

deformation of the joints. DIC calculations were performed with an open source software, called OpenDIC. Local strain analyses from DIC results were analyzed with Fiji software.
Vickers microhardness maps were performed using an automatic microhardness machine (CLEMEX), with a 25gf load applied for 10s. To analyze the hardness distribution through a weld cross-section, 31 profiles of 260 indents have been made with an increment of 80 μm in the CWD and ND, respectively.

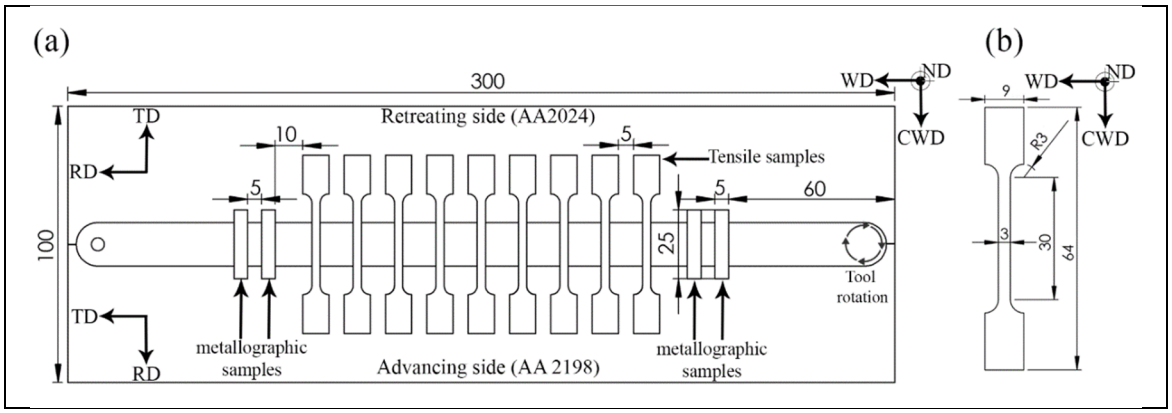

Figure 2.5 Experimental dissimilar friction stir welding process setup: a) Plates size and locations of the samples extraction. b) Geometry of the dog-bone tensile specimens. All the dimensions are in millimeter.

2.7 Temperature measurement

Four K-type thermocouples with a diameter of 1mm were used to record weldment temperatures. The thermocouples located on the weld line and 2 mm from weld line at both advancing side and retreating side to represents the thermal cycles of TMAZ and HAZ, respectively. The thermocouples were placed inside small holes with a diameter of 1mm were drilled on the plate surface. Four thermocouples were fixed with Thermigrease TG 20033 which is a silicone-free hard curing paste material. It optimizes the heat transfer in extremely high temperature conditions up to 1200°C. A digital thermometer, was used to connect six thermocouples to data acquisition system installed on a personal computer to record the temperature histories during FSW process.

CHAPTER 3

TOOL SELECTION FOR JOINING AA2198 TO AA2024

3.1 Introduction

The goal of this section is to describe the results of our efforts for finding appropriate tool design for joining AA2024 to AA2198. The effects of tool geometry on weld morphology, material flow, microstructure, hardness properties, and tensile properties were analyzed. Microhardness maps were also carried out to further document the heterogeneities of the FSWed joint variants and detection of weakness pints of joint. Besides, the relation between weakness points and fracture location of tensile test is investigated.

3.2 Surface finish quality

The surface pattern resulting from the FSW process with the three different shoulders (flat, spiral and fan) is shown in Figure 2.5 for bead on plate of AA2024. The flat shoulder (tool A) has produced flash defects on the welded surface as the flat shoulder is not effective for trapping the flowing material under the bottom shoulder (YN Zhang et al., 2012). On the other hand, raised spiral (tool B) and raised fan (tool C) shoulders prevented flash defect formation because the elliptical surface features bring back the material to the center during the rotation of the tool.

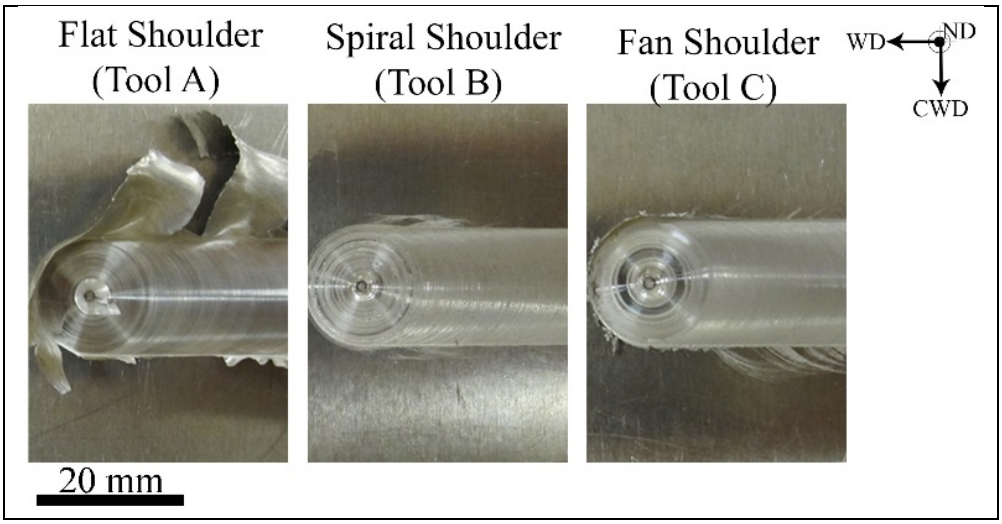

Figure 3.1 Surface morphology related to bead on plate of AA2024 material produced by tools A, B, and C. The spiral (tool B) and fan (tool C) shoulders prevent weld flashes.

3.3 Microstructure and microhardness maps

Metallography and visual examination results corresponding to the occurrence of LOP (lack of penetration), tunneling defects, and flash formation have been summarized in Table 3.1. Examples of LOP and tunneling defects are shown in Figure 3.2. Metallographic observations demonstrated that tools with a min-pin diameter half of the plate thickness (such as tools A, B and C) created LOP defect. When a longer min-pin diameter is used (equal to the plate thickness) such as tools D, E, F, and G, no LOP defect were found. It can be explained that material flow across the weld centerline amplifies with increasing the pin diameter for a fixed welding speed, insuring the mixing of the material at the bottom of weld (Mishra & Ma, 2005). Furthermore, the interfacial heat energy generation at the bottom of the joint is function of the cone diameter with higher diameter resulting in higher heat input (Gadakh & Adepu, 2013; Shi & Wu, 2017). The results of the half-threaded cylindrical pin (tool D) show the presence of a small tunneling defects, whereas no such defects were found in the straight cylindrical tool (tool E). Generally, pin threads decrease the probability of tunneling defects (Ji et al., 2013; Reza-E-Rabby & Reynolds, 2014), which suggest that the tool geometry could be used if the size of thread pitch was optimized for avoiding the formation of tunneling defect (Reza-E-Rabby & Reynolds, 2014).

Table 3.1 Defects produced as a result of tool design related to bead on plate of AA2024.

Tool	LOP defect	Flash defect	Tunneling defect
A	×	×	×
B	×		
C	×		
D			×
E, F and G	Defect-free		

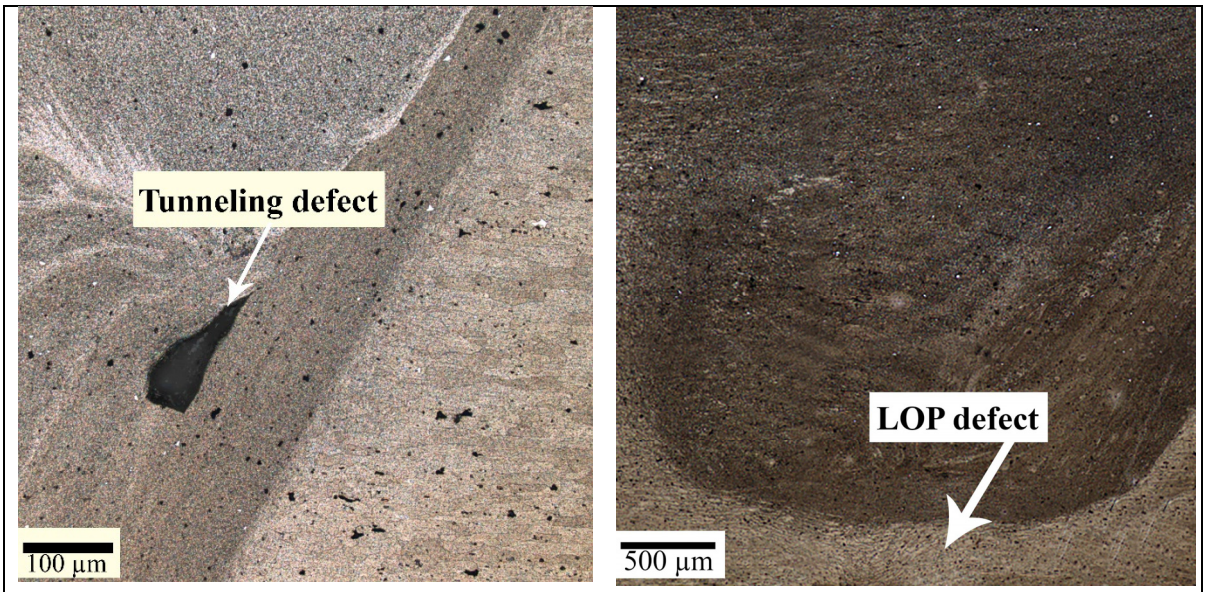

(a) (b)

Figure 3.2 Defects produced by tool A in the bead on plate welds : a) tunneling defect b) LOP defect.

On the basis of results of Table 3.1 only tool E, F and G are able to produce defect free bead on plate welds. They selected for joining AA2024 and AA2198 and the metallography examination showed the produced joints between AA2024 and AA2198 are free of defect. The AA2024 and AA2198 joints made by tools E, F, and G were denoted codes E1, F1 and G1 to, respectively and their macrograph cross-section observations in planes CWD-ND can be seen in Figure 3.3-a. The four different microstructure zones can be created by FSW process, denoted nugget, thermo-mechanically affected zones (TMAZ), heat affected zones (HAZ) and base materials. Tracking the boundaries between the base metal, HAZ, and TMAZ using grey contrast, grain size, or morphology is a challenge. The transition between the base metal and the nugget region on the AA2198 side is straightforward as small recrystallized grain

microstructures are found in the nugget region. This transition between the two regions is drawn with a yellow line on Figure 3.3-a. On the other hand, a transition band - rather than a singular boundary - was found on the AA2024 side. An easy recognizable boundary between TMAZ and nugget can be found on the advancing side, whereas a thick band of transition is found on the retreating side. It should be noted from Figure 3.3-a that the nugget zone of all the joint variants is composed of three different regions revealed with different color after etching on the CWD-ND planes. These three regions are denoted Z1, Z2, and Z3 in Figure 3.3-a. Furthermore, a sharp interface is present for sample E1 in Figure 3.3-a. This sharp interface of sample F1 is not as irregular as sample E1 with smaller min-pin diameter. It can be explained that material flow at the bottom of joint amplifies with increasing the pin diameter for a fixed welding speed, so it caused a sharp interface (Mishra & Ma, 2005).

The microhardness maps of defect free joints shown in Figure 3.3-b reflect the weld macrographs appearance in Figure 3.3-a. It can be seen joint is non-homogeneous. The maximum hardness is related to base metal of AA2024 and then AA2198 base metal. Furthermore, TMAZ of advancing side (AA2198) has lower hardness of retreating side (AA2198). Besides, Zone Z2, TMAZ, and the shoulder-affected region on AA2198 side have the minimal hardness values (90 $HV_{0.25}$), regardless of the pin geometry.

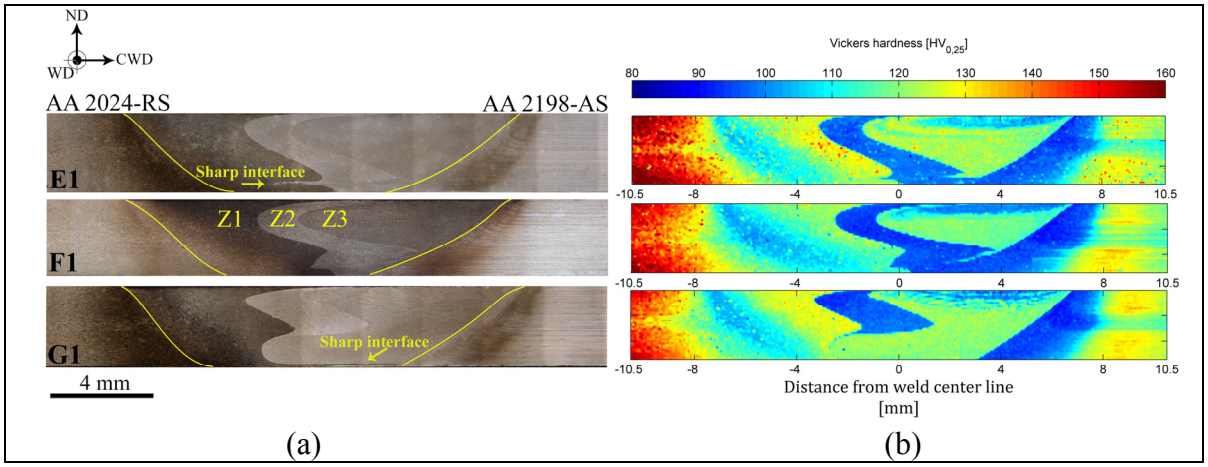

Figure 3.3 Cross-section observations of samples E1, F1, and G1 produced with tool E, F, and G (Figure 2.3): a) nugget region delimited with yellow solid lines on CWD-WD cross-section where the different colors resulting from etching are denoted zones Z1, Z2, and Z3. b) Corresponding microhardness maps showing minimal hardness values in Z2 zone, shoulder affected area, and TMAZ on the AA2198 (retreating) side.

The metallography images with higher magnification from Z1/Z2 boundary, inside Z2 and Z3 zones are shown in Figure 3.4. It can be seen that grains of AA2198 side (Z2) are coarser than AA2024 side (Z1) in the nugget region (Figure 3.4-a). The delimitation between both materials in the nugget is very clear. Comparing the microstructure of Z2 and Z3 zones in Figure 3.4-b and c shows that there is no significant difference between grain size for the two zones and Z2 and Z3 are mainly AA2198-T3.

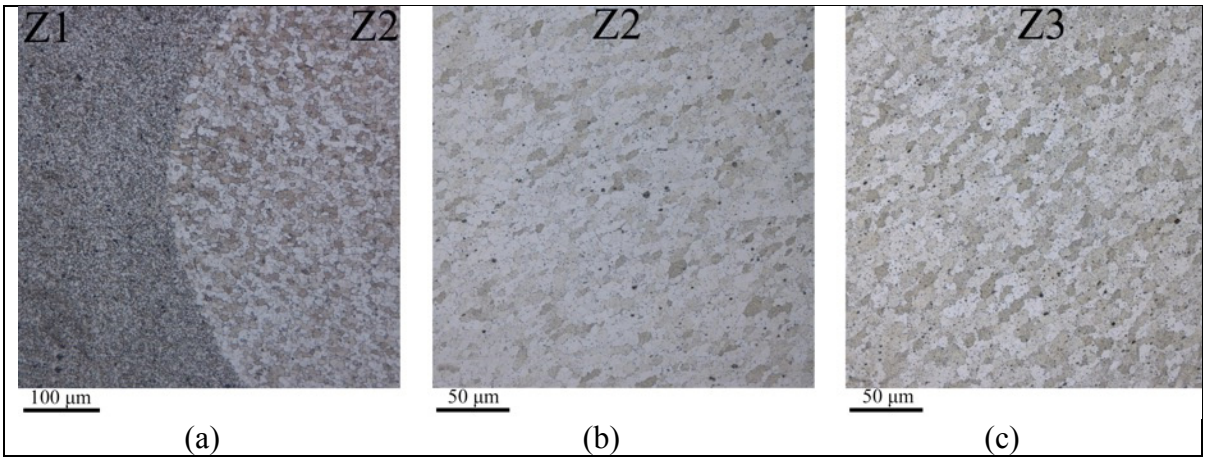

Figure 3.4 a) Cross-section optical metallography images of samples F1, a) Z1/Z2 boundary, b) inside Z2 and c) inside Z3. Zone Z2 and Z3 have coarser grain size than zone Z1 while there is not significant grain size difference between zones Z2 and Z3.

3.4 Tensile test

Tensile tests were performed for the dissimilar joints produced by three selected tools E, F, and G. The elongation (A%), the 0.2 % offset yield strength (Y.S.) and the ultimate tensile strength (U.T.S.) of the joints tested in the as-weld condition for samples E1, F1 and G1 are shown in Figure 3.5. It can be seen that tensile properties are similar, although the joint produced with tool F demonstrated both, a higher yield strength and higher elongation. The mechanical response of different tools (Figure 3.5) shows that the pin shape does not significantly affect the joint mechanical properties when joining materials with relatively low deformation resistance which is consistent with conclusions in ref. (Fujii, Cui, Maeda, & Nogi, 2006). All tensile specimens of samples E1 and G1 failed at the advancing side (AA2198) in

the TMAZ. Some F1 specimens failed at the same location (AA2198 TMAZ) and some others in the middle of the joint. The both modes of fracture is shown in Figure 3.6.

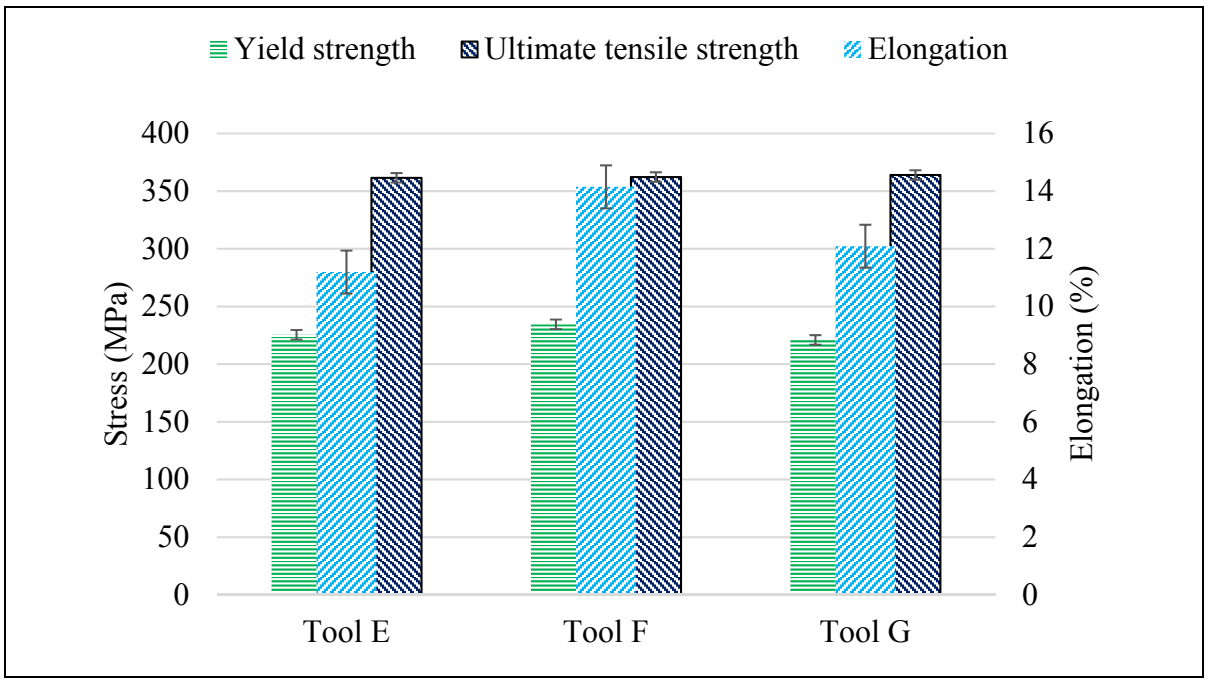

Figure 3.5 Mechanical properties of FSW joints produced by tool E, F and G at 750 RPM and 50 mm/min. The joint produced with tool F demonstrated higher mechanical strength and elongation.

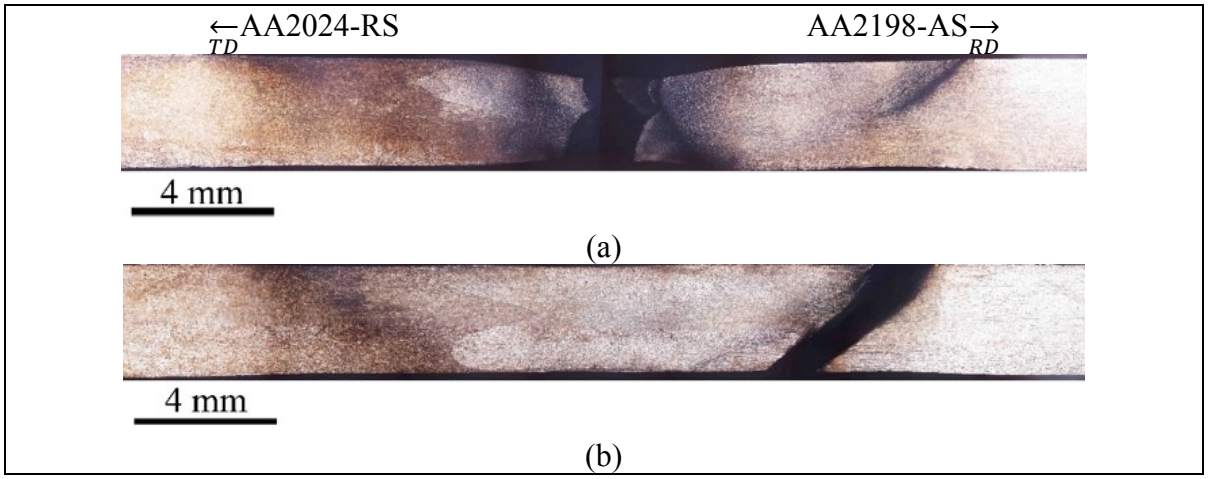

Figure 3.6 Fracture locations after monotonic tensile tests found in the middle of the joint or on the advancing side in the TMAZ. a) sample F1, b) sample G1. The fracture locations correspond to the locations with lowest hardness values in Figure 3.3-b.

3.5 Fractography

Fractography micrographs using SEM after monotonic tensile tests are reported in Figure 3.7. Figure 3.7-a shows a ductile fracture and Figure 3.7-b shows the small dimples and very small precipitates. Figure 3.7-c shows a ductile fracture, besides no evidence of dimple can be seen in the higher magnification of Figure 3.7-d. The difference between Figure 3.7-a and c could be related to the microstructure difference between middle of joint and TMAZ of AA2198. Middle of joint composed of fine recrystallized grains with re-precipitation of small precipitates which cause small dimples while TMAZ is composed the large and elongated grain structure of AA2198 with dissolution of precipitates, so no dimple can be seen.

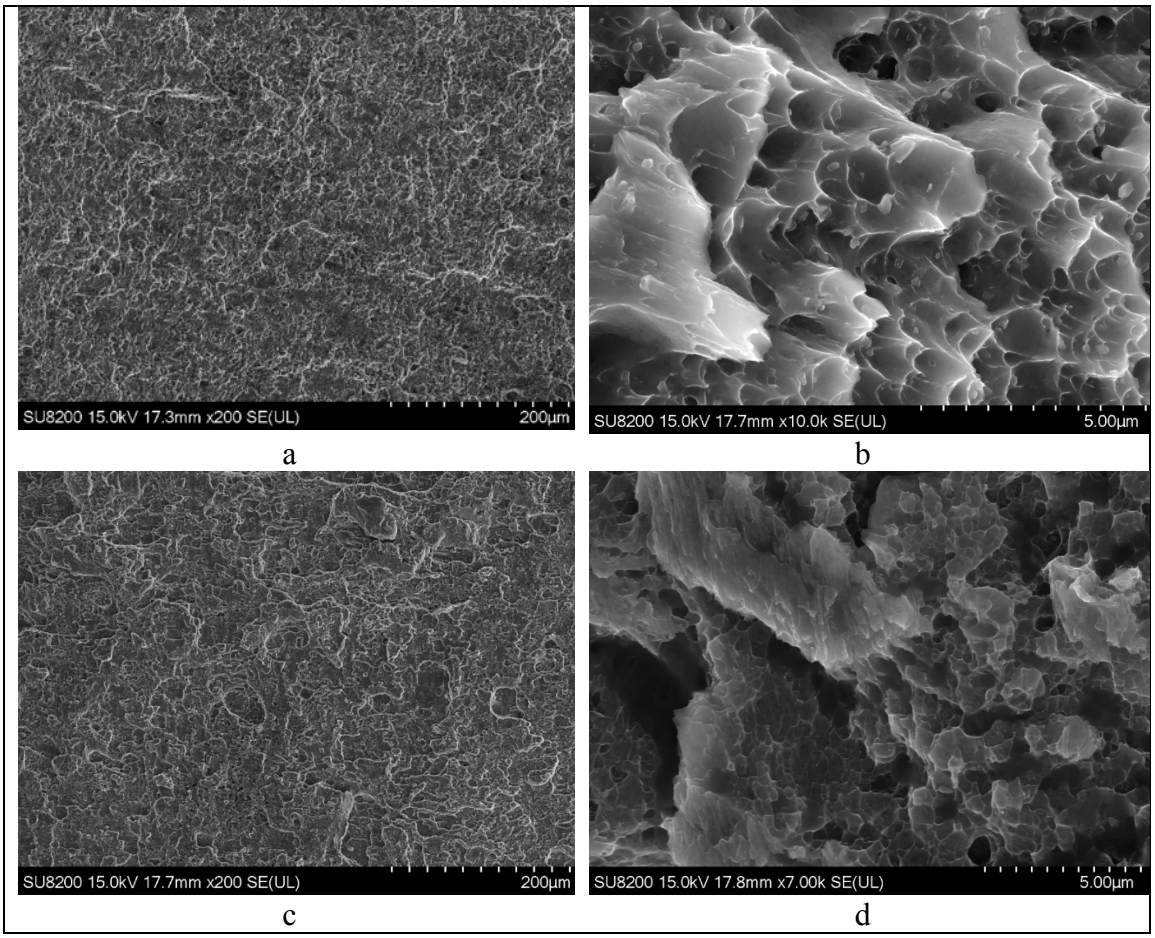

Figure 3.7 Typical fractography micrographs observed by SEM after monotonic tensile tests. a) sample F1 with a fracture in the middle of the joint, b) higher magnification from a, c) sample G1 with a fracture on the advancing side in the TMAZ of AA2198, d) higher magnification from c.

3.6 Nugget size and material flow

The nugget area (calculated from macrograph images of Figure 3.3-a) and dynamic volume of pins (explained in the section 2.2) is presented in Table 3.2. It can be seen that all the tools have created the same nugget size due to the approximately same dynamic volume of pins. It shows the dynamic volume of pin controls the dimensions of the nugget independently of pin profile.

It can be seen in Figure 2.4 and Table 3.2 that the tools E and G are completely equal during rotation; while the nugget of sample G1 is different in comparison to nugget of sample E1 as shown in Figure 3.3-a. The differences are: 1) the sharp interface of joint E1 at the bottom located in retreating side while the sharp interface of joint G1 located in retreating side; 2) higher volume of AA2198 material has gone inside to AA2024 at the bottom of joint G1 in comparison to joint E1. The mentioned differences cannot be seen between joint E1 and F1. The similarity between E1 and F1 nugget and their differences with nugget G1 can be explained by dynamic to real volumes ratio of pins. The pins of tools E and F have the same dynamic to real volumes ratio, so they have formed similar nugget profiles, while the ratio is higher for pin of tool G and it causes a different material flow and nugget profile.

Table 3.2 Relation between pin profile and joint cross-section area.

Tool code	real pin volume (mm^3)	Dynamic pin volume (mm^3)	Dynamic to real volumes ratio	Joint area (mm^2)
Tool E	47.7	47.7	1	33
Tool F	40.0	40.0	1	30
Tool G	30.3	47.7	1.6	31

3.7 Conclusions

Different tool designs were used for bead on plate of AA2024. Tools E, F and G could produce bead on plate welds free of defect. Subsequently, they used for joining AA2024 and AA2198 dissimilar and the all produced joints were free of defect. The tensile test performed on the defect free joints. Tool F demonstrated both, a higher yield strength and higher elongation, so, it could be considered as a better design for joining AA2024 to AA2198. The next chapter will investigate the optimization of the welding speed parameters for tool F.

CHAPTER 4

OPTIMIZATION OF WELDING SPEED PARAMETERS

4.1 Introduction

Inappropriate FSW welding speeds produce defective joints. Besides, the speed parameters determine the heat input of process, while the 3rd generation of aluminum alloys are sensitive too high temperatures. Thus, the optimization of welding speeds is a necessity for producing a defect free joint with high mechanical properties. The goal of this chapter is to show the followed steps for optimizing the welding speed parameters between AA2198 and AA2024.

4.2 Joint macrograph

Macrograph analysis was conducted on the produced joints with varies welding parameters (Table 2.4) as shown in Figure 4.1. Tunneling defect was found only for the joint processed with the highest welding speeds (Joint F6: rational speed=1000 RPM; traverse speed=450 $mm.min^{-1}$). It is found that increasing the rotational speed at a constant traverse speed (joints F4 vs. F6) raises the possibility of tunneling defects (Reza-E-Rabby & Reynolds, 2014). All the samples welded at traverse speed higher than 150 $mm.min^{-1}$ contain kissing bond defects because the weld was not hot enough to allow material flow in the root of the weld. Thus, it can be concluded that the tool length has to be increased at higher welding speeds to avoid the formation of kissing bond defect.

The morphology of the nugget region varies by changing the welding parameters due to different material flow. For both samples of F3 and F5 (same traverse welding speeds but different rotation speeds), onion rings on the top of the nugget can be seen, while there are no onion rings for the rest of the samples. It can be concluded that onion rings can be removed by optimizing the welding speed parameters.

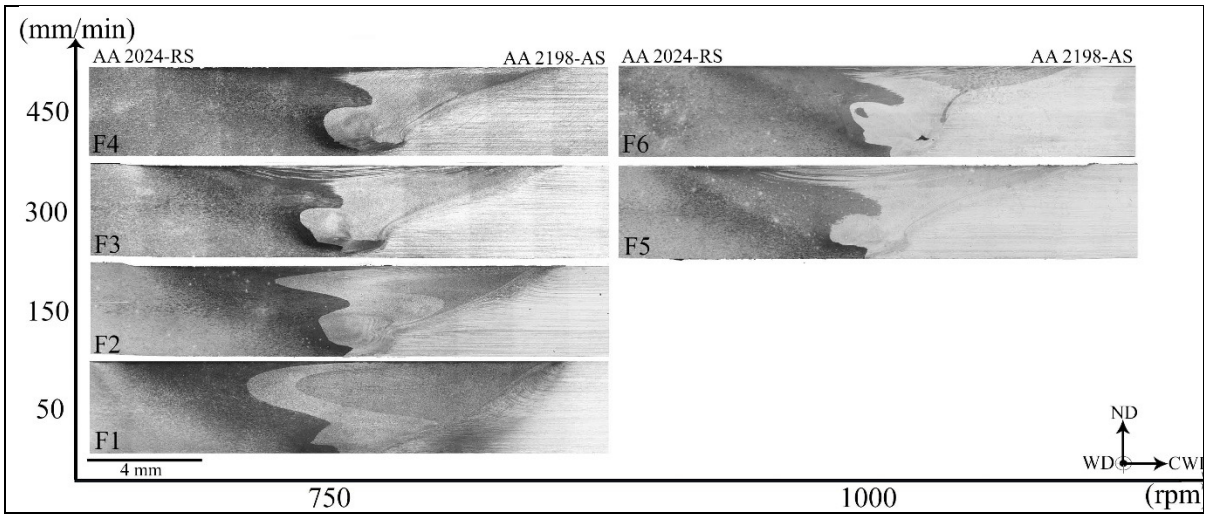

Figure 4.1 Cross-sectional macrographs of joints produced by tool F with parameters of Table 2.4. The tunneling defect was found only in the joint F6 with highest rational speed (1000 RPM) and highest traverse speed (450 mm/min).

4.3 Microhardness map

Two dimensional hardness map across the ND-CW section through the weld joints of samples F1, F2 and F4 (traverse speeds of 50, 150 and 450 $mm.min^{-1}$ at the same rotational speed (750 RPM) is shown in Figure 4.2. It can be seen that the traverse speed decreases the size of Z3 zone (Table 4.1). It could be as a result of different material flow around pin. The material rotates around pin from advancing side to retreating side and then it comes back to advancing side behind of tool. The material which is closer to tool experiences higher flow speed and deformation. This result is consistent with material flow simulation that shows the area covered by the pin movement and experiences higher deformation, enlarges by decreasing the traverse welding speed or increasing rotational speed (Shi & Wu, 2017).

The microhardness of samples F1 and F4 at different locations of the joint is extracted from Figure 4.2 and is shown in Table 4.1. It can be seen that the hardness of TMAZ at both AA2198 and AA2024 sides have increased about 16 $HV_{0.25}$ and 35 $HV_{0.25}$ by increasing the traverse speed from 50 mm/min to 450 mm/min. Besides, the hardness of nugget center has increased about 17 $HV_{0.25}$. Heat input has a reverse relation with traverse speed on the basis of eq. 1.1. The heat input of sample F4 is 9 times less than F1 sample. Indeed, the less heat input at higher

traverse speed leads to less precipitate solution/coarsening followed by higher hardness of the joint F4 (R. Kumar, Singh, & Pandey, 2012).

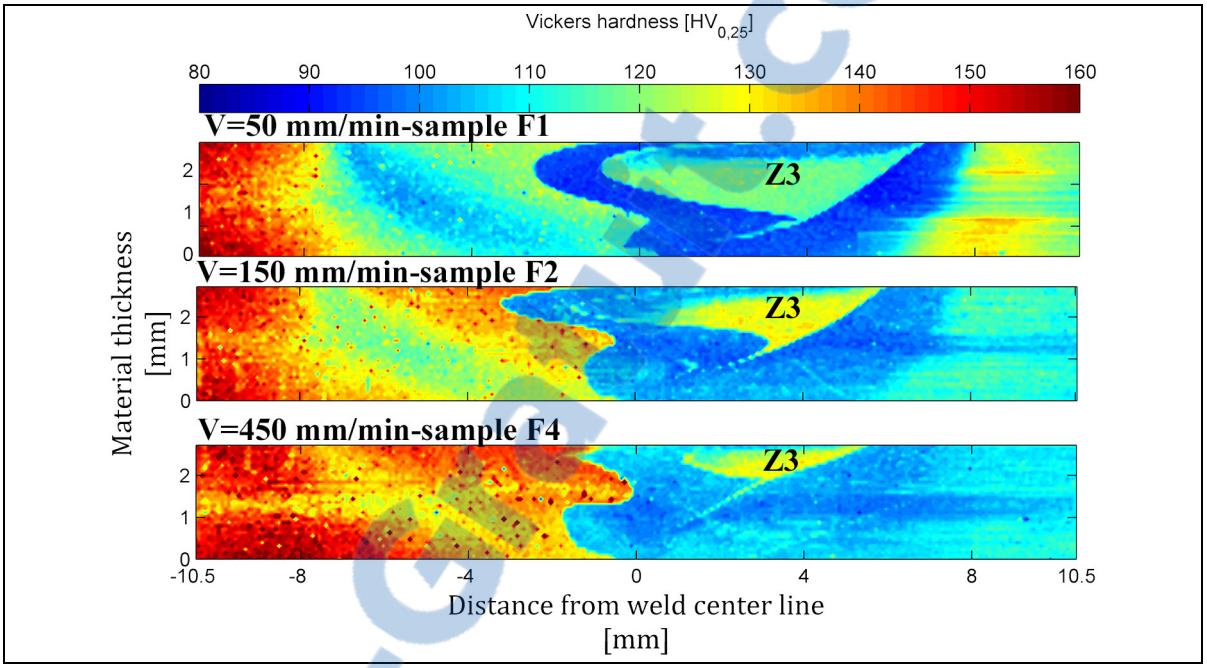

Figure 4.2 Two dimensional hardness map across the ND-CW section through the weld joints of samples F1, F2 and F4. Higher welding speed increases the general hardness of joint.

Table 4.1 The microhardness of samples F1 and F4 at different locations of the joint.

Welding traverse speed	Nugget center	TMAZ AA2198	TMAZ AA2024
50 mm/min (sample F1)	91	93	108
450 mm/min (sample F4)	108	109	133
$\Delta H_{0.25}$	17	16	35

Table 4.2 The size of Z3 zone at different welding traverse speed.

Sample F1 (50 mm/min)	Sample F2 (150 mm/min)	Sample F4 (450 mm/min)
9 mm^2	5 mm^2	2 mm^2

4.4 Mechanical response

The mechanical properties of FSW joints with different welding speeds are reported in Figure 4.3. Increasing the rotational speed at the same traverse speed (sample F3 and F5) was shown to have no significant effect on the mechanical properties of the joint. This result is in good

agreement with investigations done by Dubourg *et. al.* (Dubourg, Amargier, & Jahazi, 2008). As depicted in Figure 4.3, with the same rotational speed (750 RPM), increasing the traverse speed from 50 mm.min^{-1} to 450 mm.min^{-1} increases the joint yield strength from 235 MPa to 286 MPa, respectively (about 22% improvement). This latter result is consistent with a previous study on AA2198-T8 (Ma et al., 2013). Sample F6 has the lowest elongation and ultimate tensile strength due to tunneling defect despite a relatively good yield strength compared to other conditions. The fracture locations of all samples are located at nugget area inside AA2198 material. Results also show that the optimum rotational and traverse speeds to achieve the highest yield strength are 750 RPM and 450mm.min^{-1}, respectively. The welding parameters correspond to the smallest welding speed ratio (Table 2.4).

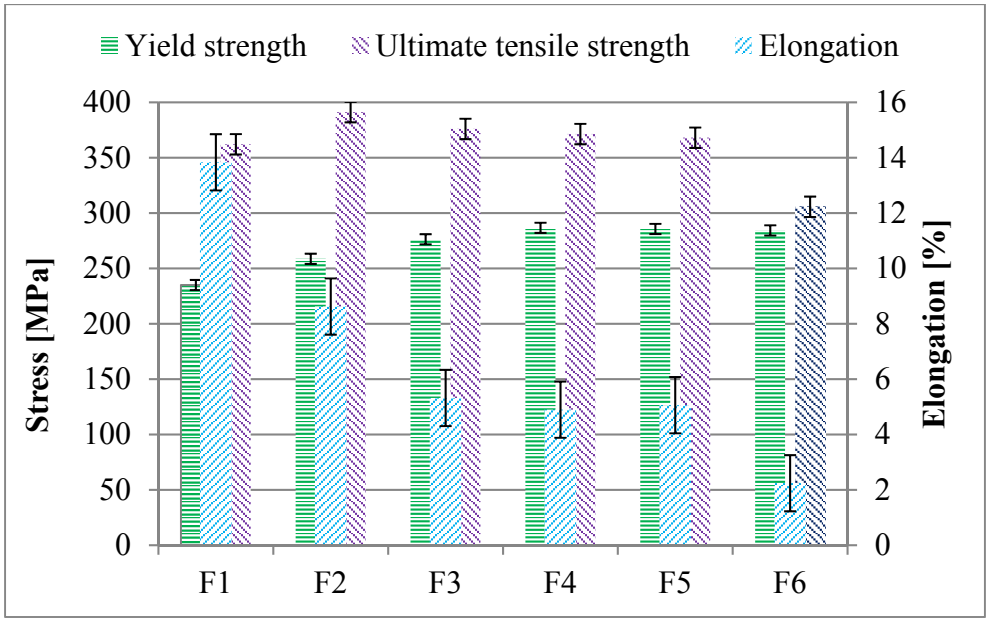

Figure 4.3 Mechanical properties of FSW joints produced by tool F according to welding conditions in Table 2.4 Welding speed parameters.. The parameters of 750 RPM and 450mm/min produced the joint with highest yield strength.

The joint efficiency (the ratio between yield strength of the joint and the weakest base metal) is shown in **Erreur ! Source du renvoi introuvable.**. It can be observed that an increase from 50 mm.min^{-1} to 450 mm.min^{-1} at 750 RPM has improved the joint efficiency from 63% to 78 %.

4.5 Conclusions

In the present chapter the influences of traverse and rotational speeds on the AA2198/AA2024 dissimilar joint yield strength efficiency for the optimal tool were documented. The following points are the main conclusions of this chapter:

- The optimum welding speed parameters in the range of tested parameters are 750 RPM and 450 $mm.min^{-1}$ for achieving the highest yield strength and the joint efficiency can reach up to 78%.

-The formation of tunneling defects occurs when increasing the rotational and traverse welding speed over 750 RPM and 450 $mm.min^{-1}$, respectively.

-The formation of kissing bond defects occurs when increasing the traverse welding speed over 150 $mm.min^{-1}$. In this case increasing the pin length could solve the problem.

- Higher traverse speeds increase the hardness of nugget, TMAZ and HAZ.

The next chapter will investigate the possibility of increasing the joint strength by applying heat treatments before and after welding.

CHAPTER 5

INFLUENCE OF POST WELD HEAT TREATMENT ON MECHANICAL PROPERTIES OF AA2024 AND AA2198 JOINT

5.1 Introduction

In this chapter, the following questions in relation to FSW of AA2198 to AA2024 will be answered: 1) Should T8 heat treated plates be used for welding even if there is a possibility of local strength loss after welding or is it better to apply artificial aging after welding? 2) To which extent post weld heat treatment can improve the loss of mechanical properties in the joint area? 3) Can cold stretching, applied before artificial aging, improve the joint strength?

The various characterization methods were used to find the answer to above questions. The joint macrograph revealed the presence of possible weld defects. Tensile test provided the yield strength, elongation and ductility of the joint. Details about the fracture mode of joints were obtained using the SEM images. A combination of microhardness maps and digital image correlation (DIC) results were used to study the joint mechanic properties and their relation to fracture location.

5.2 Joint macrograph

As-welded macrographs are shown in Figure 5.1 for joint between AA2024-T3 and AA2198-T3 plates (AW-T3) and joint between AA2024-T8 and AA2198-T8 (sample AW-T3). The both macrographs are similar to what is already explained in section 3.3. The S shape zone (or zone Z2 in section 3.3) in the middle of joint can be seen for both joints. It worth to mention that the S shape zone was the fracture location due to lower hardness in previous chapter. It can be seen that there is no observable defect in the joints. The as-welded joint between AA2024-T3 AA2198-T3 (sample AW-T3) were used for aging post weld heat treatment with pre-straining (PRPW-T8) and without pre-straining (PW-T8). The codes and heat treatment conditions is already explained in section 2.5.

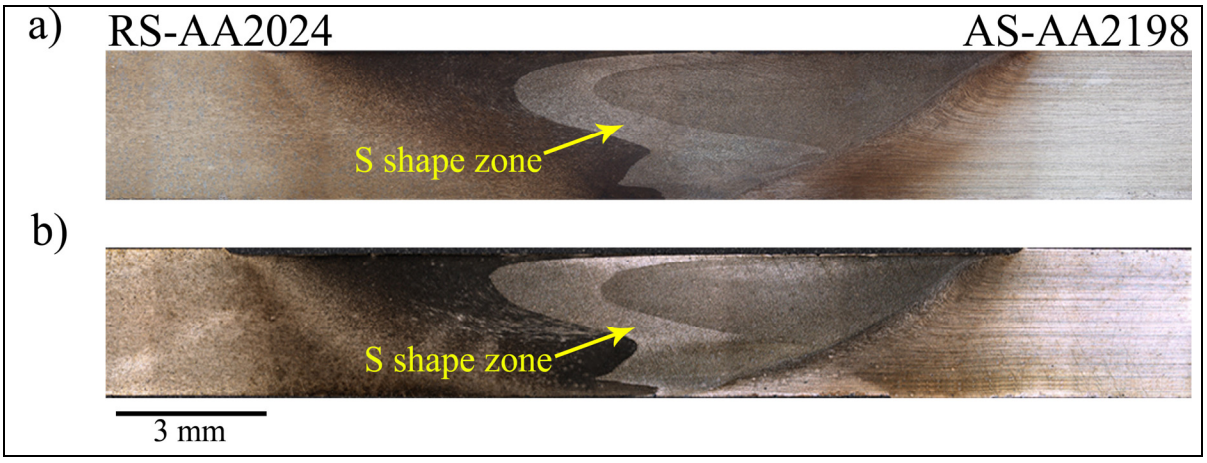

Figure 5.1 Cross-section observations in CWD-ND plane of as-welded samples: a)AW-T3 and b)AW-T8. The both micrograph are similar and S shape zone with lighter color can be seen in the center of nugget.

5.3 Microhardness maps

Two dimensional microhardness map across the ND-CW section through the joint area for as-welded samples (AW-T3 and AW-T8) and post weld heat treated samples (PW-T8 and PRPW-T8) are shown in Figure 5.2. The microhardness maps of as-welded samples (Figure 5.2 a and d) show S shape zone, TMAZ/HAZ and the shoulder affected region, on the advancing side (AA2198) having the minimum hardness values. The results also show that using T8 plates (sample AW-T8 in Figure 5.2-d) compared to T3 plates (sample AW-T3 in Figure 5.2-a) does not bring any significant hardness improvement in the joint area. Figure 5.2-b (PW-T8) shows that applying aging post weld heat treatment on T3 joint (sample AW-T3 in Figure 5.2-a) has significantly improved the hardness of TMAZ on the advancing side and removed the S shape zone resulting a more homogenous nugget but it has not positive effect on the hardness of TMAZ zone on the retreating side of AA2024 . Figure 5.2-c shows that applying deformation before aging treatment improved significantly the hardness of the advancing side generating the highest hardness for all areas of the joint. Besides, the low hardness problem of as-welded sample in the advancing side has been solved and the size of low hardness area in the retreating side is decreased by applying deformation before the post weld heat treatment.

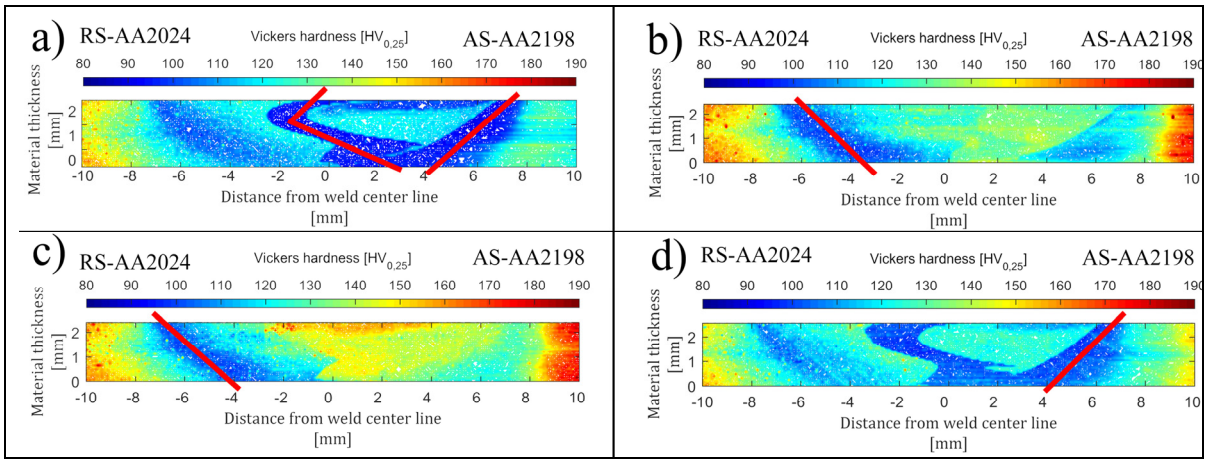

Figure 5.2 Two dimensional hardness map across the ND-CW section through the weld joint: a) AW-T3 b) PW-T8 c) PRPW-T8 and d) AW-T8. The red lines are fracture locations.

5.4 Mechanical response

Yield strength (YS, 0.2 pct. offset), ultimate tensile strength (UTS) and nominal strain (A%), of as-welded and post weld heat treated joints are shown in Figure 5.3. The average values are reported in Table 5.1. As it can be seen, there is no difference between yield strength of as-welded samples which means that using plates with T8 heat treatment before welding has not any advantage than plates in T3 conditions; as the opposite, the joint elongation is decreased. Applying T8 post weld heat treatment (PW-T8 sample) improved negligibly the yield strength in comparison to the as-welded samples (AW-T8 and AW-T3). Combination of pre-straining and post weld heat treatment (PRPW-T8) has the highest yield strength between all samples with about 18% more than as-welded samples.

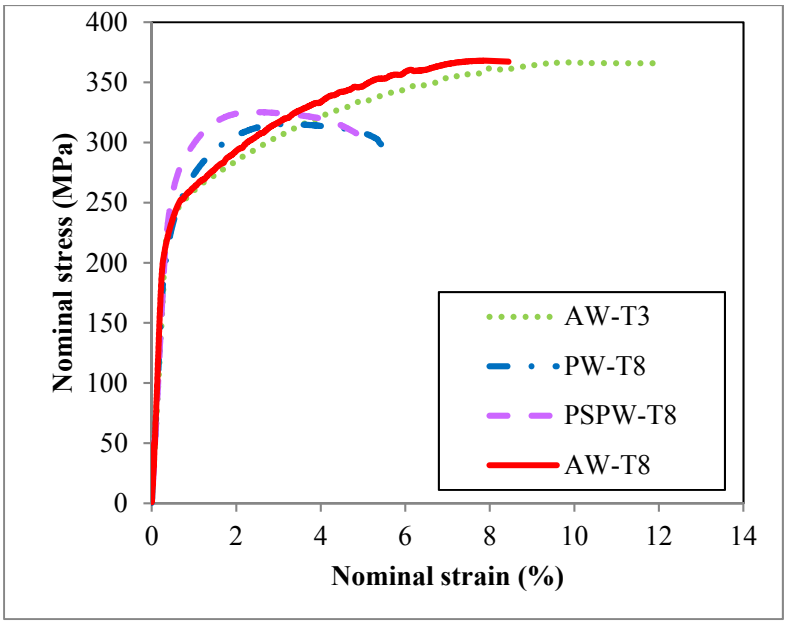

Figure 5.3 Mechanical properties of FSW joints in as welded and post weld heat treated conditions.

Table 5.1 Average mechanical properties of FSW joints in as welded and post weld heat treated conditions.

Sample code	Yield strength (MPa)	Ultimate tensile strength (MPa)	Elongation (%)
AW-T3	234	362	14
PW-T8	242	316	6
PSPW-T8	275	324	5
AW-T8	232	361	8

5.5 Fractography

The fracture locations of tensile test samples are shown by solid red line in Figure 5.2. All tensile specimens in as-welded conditions failed at the advancing side (AA2198) in the TMAZ except two of four tensile specimens of AW-T3 samples which failed at center of nugget (in the S shape located inside AA2198 material). All post weld heat treated samples failed at the retreating side (AA2024). This means that the fracture location has been transferred from AA2198 to AA2024 side by post weld heat treatment process.

The fractography in the middle of joint is already discussed in section 3.5. The fractures in TMAZ discuss here. The fractography images are reported in Figure 5.4. It can be seen that the as-welded fracture surfaces (Figure 5.4-a and d) are ductile with no evidence of dimples (location TMAZ AA2198). In contrast, the fracture of post weld heat treated samples are ductile with big dimples (location TMAZ AA2024). The back scattered images of the fracture surface in Figure 5.5 shows the dimples are caused by coarse intermetallic particles which is already reported by (Robe et al., 2015).

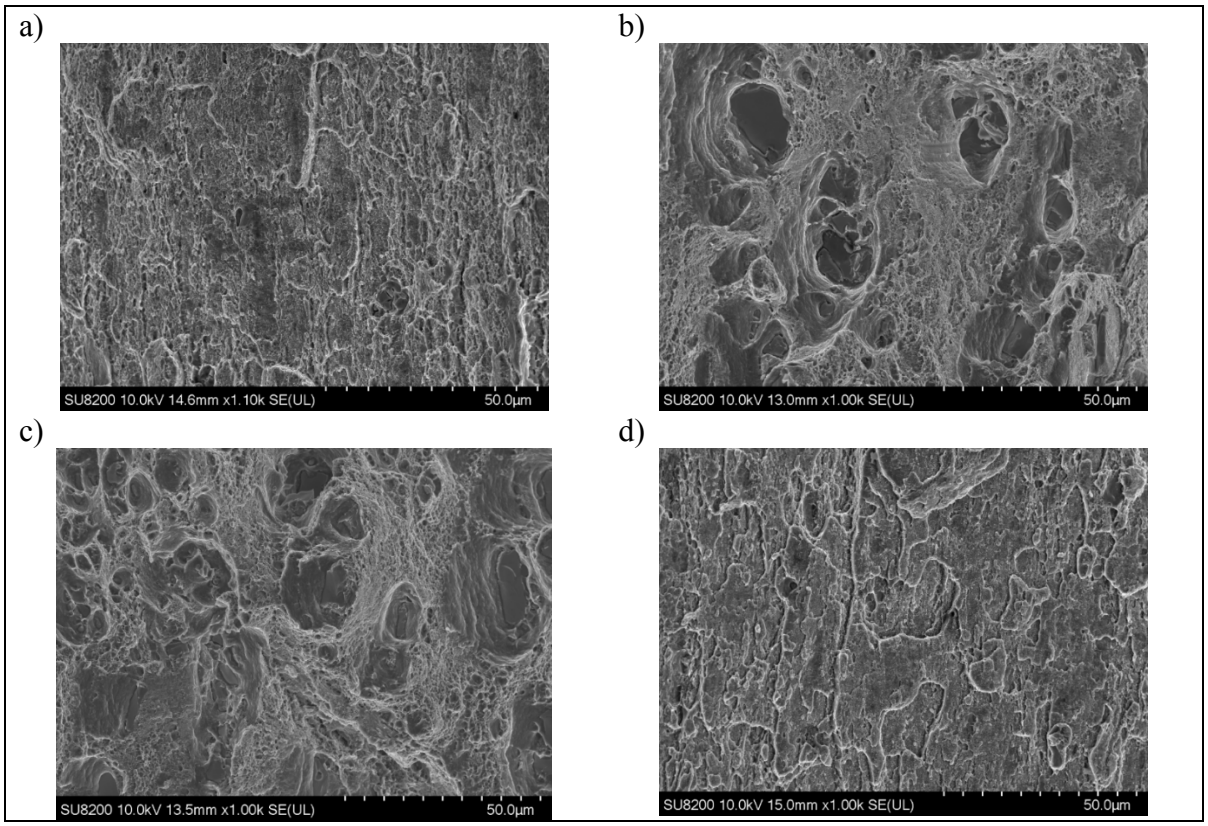

Figure 5.4 Fractography micrographs observed by SEM after monotonic tensile tests of as-welded and post weld heat treated samples: a) AW-T3 (location: TMAZ of AA2198) b) PW-T8 T3 (location: TMAZ of AA2024) c) PRPW-T8 T3 (location: TMAZ of AA2024) d) AW-T8 T3 (location: TMAZ of AA2198)

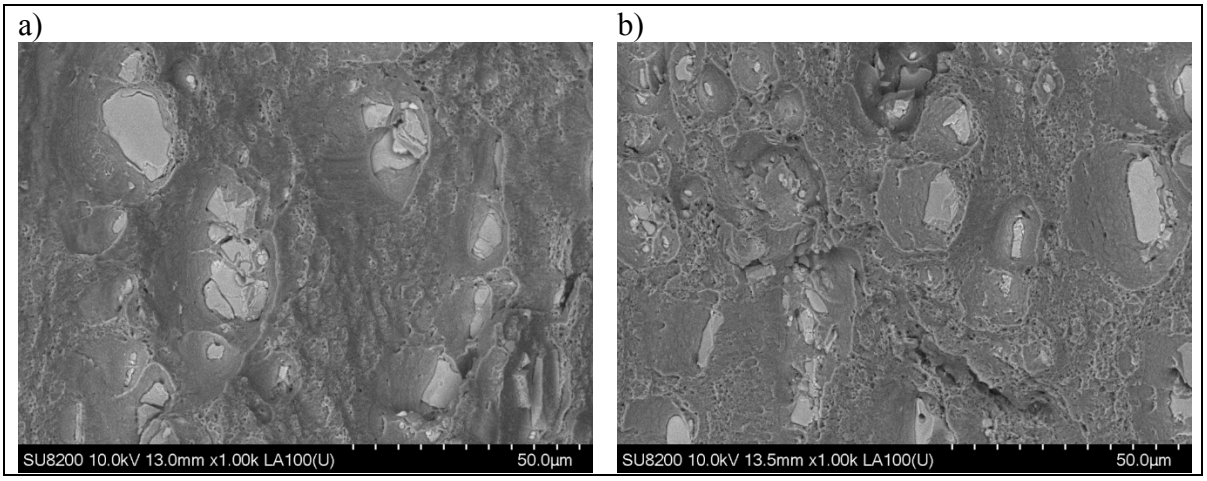

Figure 5.5 SEM back scattered images of fracture surface for heat treated samples by SEM after monotonic tensile tests. a) PW-T8 b) PRPW-T8

5.6 Digital image correlation

Strain maps in the principal loading direction obtained from digital image correlation (DIC) of samples in as-welded and post weld heat treated conditions are depicted in Figure 5.6 for various macroscopic stress levels. This finding confirms that the deformation of the joint is heterogeneous. The strain localization is located in S shape zone and TMAZ of advancing side (AA2198) for as-welded samples (AW-T3 and AW-T8), while is located in the TMAZ of retreating side (AA2024) for post weld heat treatment (PW-T8 and PRPW-T8). It was found that early plastic deformation starts in the AA2198 TMAZ/HAZ region of as-welded samples for macroscopic stress as low as 200MPa. For higher stress levels (above 240 MPa), irreversible deformations develop conjointly in the S shape zone and in the AA2198 TMAZ/HAZ region with equivalent strain levels but final rupture happens in the TMAZ of AA2198. T8 post weld heat treatment (PW-T8) has improved the uniformity of nugget as there is no strain localization in the S shape zone but a severe strain localization takes places in the AA2024 TMAZ/HAZ region. The combination of pre-straining and post weld heat treatment (PRPW-T8) has removed the strain localization for both AA2198 TMAZ/HAZ and S shape zones. All fracture locations correspond to the area with the lowest hardness values (Figure 5.2) and highest strain localization regions (Figure 5.6). Lower local mechanical properties are commonly reported for the TMAZ/HAZ regions (Robe et al., 2015; Texier et al., 2016). The fracture of as-welded samples have the same location as reported in the literature i.e. TMAZ

of AA2198 (Ma et al., 2013; Robe et al., 2015) despite some samples have broken in the middle of joint (in the AA2198 side) for sample AW-T3.

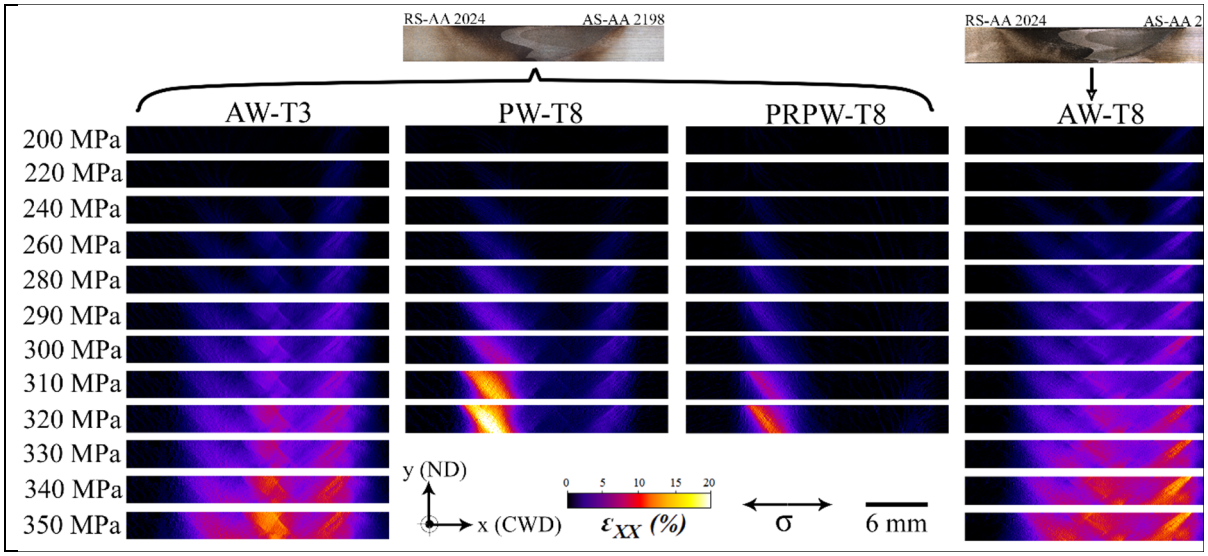

Figure 5.6 Local in-plane strain distribution obtained with DIC. The strain localization for as-welded samples are same (nugget center and AA2198 TMAZ/HAZ) while applying post weld heat treatment changed the strain localization to AA2024 TMAZ.

5.7 Temperature measurement

Temperature measurements of the different regions of the weldment, particularly the HAZ/TMAZ regions, can help understanding the root cause of low hardness observed in the joint areas by comparing the solution temperature of strengthening precipitates. Temperature measurement around HAZ and TMAZ are reported in Figure 5.7. The peak temperatures were extracted from Figure 5.7 and are shown in Table 5.2. It can be seen that the temperature in the advancing side slightly is less than the retreating side for both TMAZ and HAZ while it is reported that the temperature slightly is higher in advancing side (Hwang, Kang, Chiou, & Hsu, 2008; Shi & Wu, 2017). The reason is that thermocouples in the advancing side have been located near to the starting place of weld while the retreating side are close to the ending point of weld so the measurements are in transient situation. Therefore, steady state temperatures are between the reported measurements.

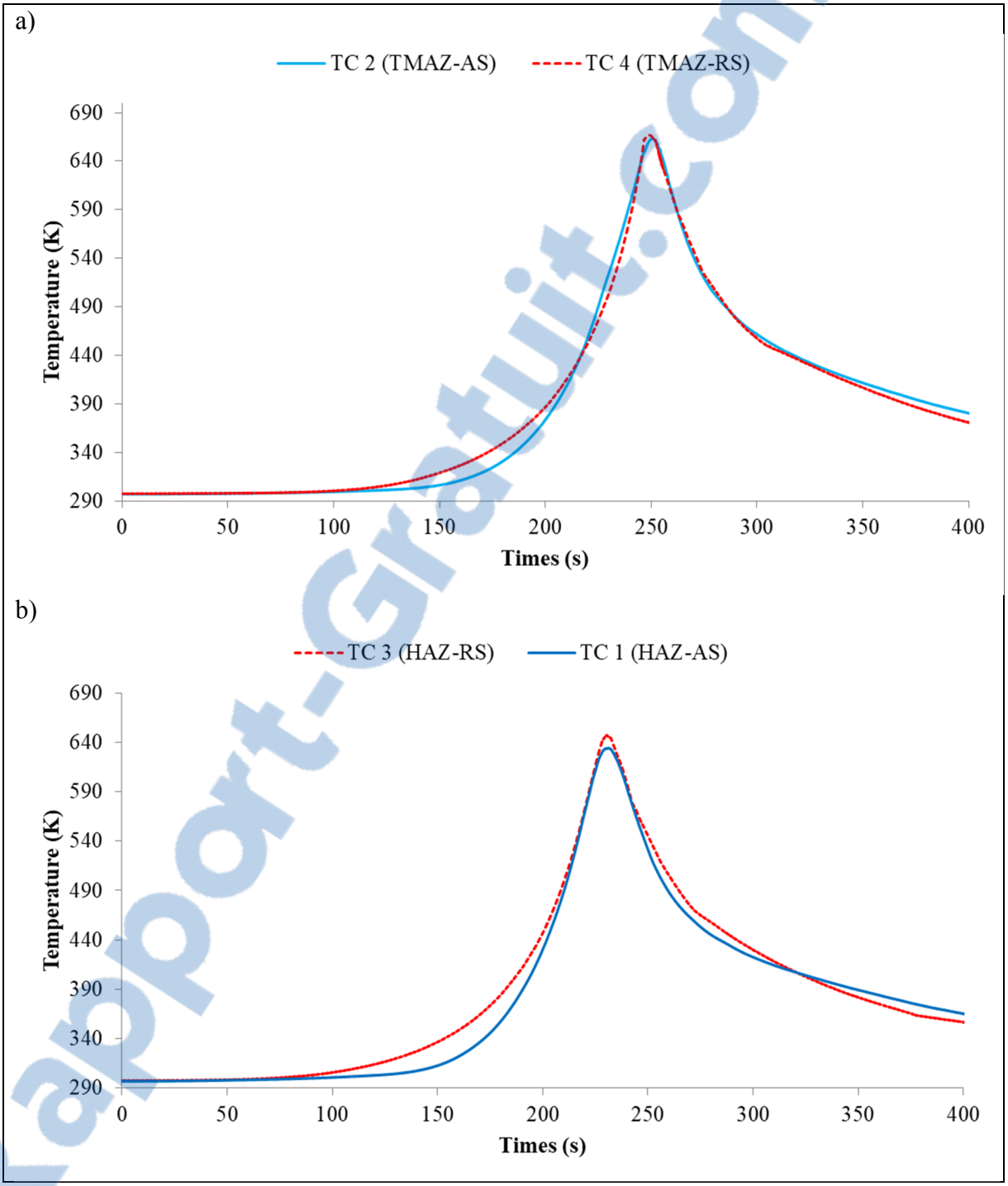

Figure 5.7 Temperature measurement of TMAZ and HAZ during FSW process. a) TMAZ-thermocouple is located on weld edge. b) HAZ- thermocouple is located 2mm far from weld edge.

Table 5.2 Maximum temperate in different locations of the sample AW-T3.

Location	HAZ	TMAZ
Retreating side (AA2024)	633 (TC 1)	662 (TC 2)
Advancing side (AA2198)	646 (TC 3)	666 (TC 4)

5.8 Discussion

The AA2024 main strengthening phase is S (Al_2CuMg) precipitates, and their precipitations and thickening occurs around 538 K. The solution temperature of S phase is around 743 K (Dixit et al., 2009; Genevois, Deschamps, Denquin, & Doisneau-cottignies, 2005). The maximum measured temperature at HAZ and TMAZ (Table 5.2) of AA2024 is higher than the precipitation of S phase and bellow its solution temperature, resulting possible coarsening during the heat exposure.

The AA2198 main strengthening phase is T_1(Al_2CuLi) precipitates and the solution temperature of T_1 phase is around 648 K (Dorin, Deschamps, De Geuser, Lefebvre, & Sigli, 2014). The maximum temperatures in HAZ and TMAZ in AA2198 (Table 5.2), are higher than the solution of T_1 phase and therefore, it can partially dissolve them. Hence, the coarsening of S phase in 2024 and partial dissolution of T_1 precipitates during FSW process are probably the reasons for observed lower hardness of as-welded samples in TMAZ/HAZ areas (Figure 5.2).

The hardness of HAZ/TMAZ and nugget at AA2198 side (advancing side) has significantly improved in post weld heat treated samples. The reason could be related to the re-precipitation of T_1 phase in the nugget and TMAZ/HAZ (S.-f. Zhang et al., 2014) while the low temperature of the post weld heat treatment has not significant effect on 2024 precipitates as the hardness in AA2024 did not change significantly.

The microhardness maps discover the fact that the PWHT could be effective for the similar joint of AA2198. Furthermore, in the applications that high mechanical properties of similar joint AA2198 is demanded; it is logical to use T3 plates and then apply aging treatment on the whole of structure (due to loss of mechanical properties at joint area). If applying PWHT is not possible due to big dimensions of the structure, T8 plates can be used for welding followed by locally aging treatment on the joint area to recover the mechanical properties of the joint. It should be noted it is a proposal on the basis of current experimental data and experimental plan should be done for its validation.

5.9 Conclusions

The FSW process were done on the joint between AA2024 and AA2198 in both T3 and T8 heat treatment conditions. Subsequently, T8 post weld heat treatment with and without pre-straining was applied on welded samples in T3 conditions to investigate the possibility of joint mechanical properties improvement. The following conclusions was extracted:

-Using AA2024 and A2198 plates in T8 and T3 will create joints with similar mechanical properties due to loss of mechanical properties during FSW process, so using T3 plates from economical points of view is recommended.

-Applying post weld heat treatment for a dissimilar joint is complex. PWHT for dissimilar joint between AA2024 and AA2198 without pre-strained is not effective for global mechanical properties improvement.

- PWHT for dissimilar joint between AA2024 and AA2198 with pre-strained could improve the yield strength, but it is mostly the result of hardworking not post weld heat treatment.

-PWHT improves the mechanical properties in AA2198 side but it has not any positive effect on AA2024 side of joint, even the strain localization happens at lower stresses.

-Higher hardness in the advancing side (AA2198) and lower hardness in the retreating side (AA2024) of heat-treated samples compared the to as-welded samples could be related to T_1 precipitation and coarsening of S phase, respectably.

-The fracture locations of as-welded samples are TMAZ of AA2198 and center of nugget. Applying PWHT changes the fracture location to TMAZ of AA2024 due to improvement of hardness in the TMAZ of AA2198.

-The fracture surface of post weld heat treated samples contains big dimples which confirms the presence of overaged precipitates in the AA2024 side.

The next chapter is going to investigate the heat transfer simulation of FSW process to obtain the temperature distribution of the joint area. By using simulation, it is possible to study the possibility of using active cooling during welding to prevent heat exposure which causes precipitates dissolution/coarsening.

CHAPTER 6

SIMULATION OF FRICTION STIR WELDING

6.1 Introduction

It is important to estimate the peak temperature during FSW process and eventually minimize it, in order to managing precipitation dissolution in the joint area. AA2198 material is more sensitive to high temperature than AA2024. The solution temperature of S (Al_2CuMg) phase for AA2024 is around 743 K while the solution temperature of T_1 (Al_2CuLi) phase for AA2198 is around 648 K (Dixit et al., 2009; Dorin et al., 2014; Genevois et al., 2005). It is possible to use a cooling jet such as air, mixture of air and water, liquid CO_2, or liquid Nitrogen to cool the joint area.

The numerical simulations will reduce the R&D cost and time to find the optimized welding process without experimental process. The following parts discuss the assumptions of heat transfer model, numerical equations and simulation results for modeling of heat transfer during the friction stir welding of AA2024-T3 to AA2198-T3.

6.2 Numerical details

6.2.1 Simulation assumptions

The following assumption were taking into account for simulation process:

1) The friction stir welding tool moves with a constant welding speed during the process of joining. In order to simulate the FSW process, it is more convenient to consider a moving coordinate instead of a stationary coordinate system that transports with the tool movement. In this case it is possible to change the transient heat transfer of FSW process to steady state heat transfer. In other words, it is assumed that the aluminum plates are infinitely long, thus the analysis neglects the edges at the starting and ending of welding process which is rational proposition to reduce the complexity of simulation and the computational cost.

2) A symmetric geometry for workpiece modeling reduces the computational cost. Therefore, in the present simulation only AA2024 side of plate has been modeled. It means the joint was considered a similar AA2024 joint not a dissimilar AA2198-AA2024 joint.
3) Heat flow from tool into the workpiece stops if the local temperature reaches the material melting point.

6.2.2 Computational domain and grid generation

Figure 6.1 depicts the computational domain of present FSW numerical simulation which is designed in accordance to the experimental setup of the present project (presented in Figure 2.1). A summary of computation domain is presented in Table 6.1. To simulate the present domain, non-uniform grid configuration was generated in COMSOL Multiphysics. A total number of 60830 non-uniform (hexahedral, triangular and quadrilateral) meshes were selected for the simulation (see Figure 6.1). Convergency criteria of 10^{-5} has been considered for all the simulations.

Table 6.1 Computational domain details

Domain	Dimensions
Tool shoulder diameter (mm)	15.8
Pin diameter (mm)	4.7
Pin length (mm)	2.7
Workpiece density (g/m3)	2.78
Workpiece length (mm)	300
Workpiece width (mm)	100
Workpiece thickness (mm)	3.18

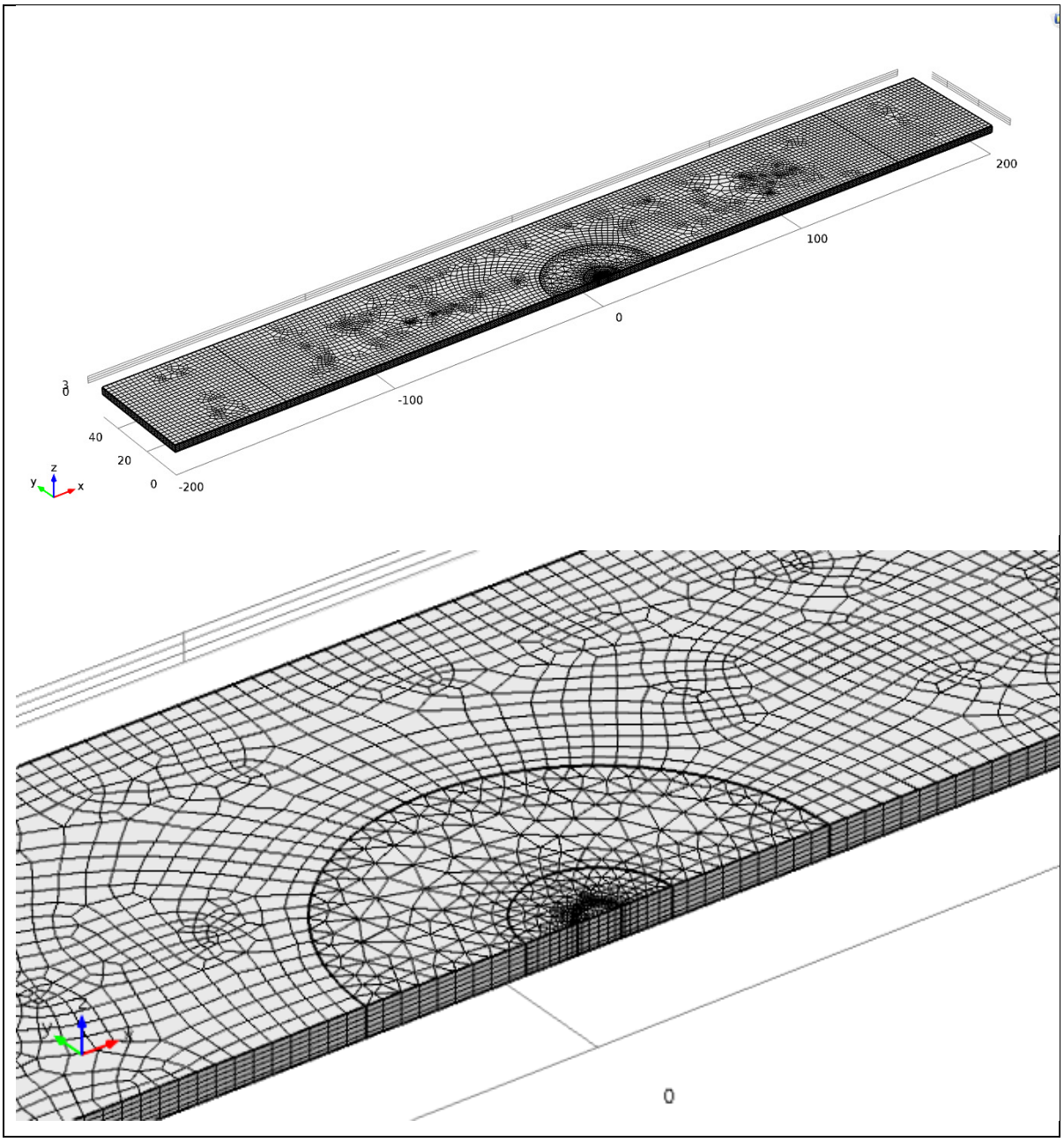

Figure 6.1 Work price geometry and meshing around the pin area. The dimensions are millimeter.

6.2.3 Numerical equations

6.2.3.1 Heat transfer equation

The heat transfer equations for welding in a moving coordinate can be written as:

$$\nabla.(-k\nabla T) = Q - \rho c_p v.\nabla T \tag{6.1}$$

where T is the temperature, $c_p$is the heat capacity, ρ is the density, k is the heat conductivity, and v is the domain velocity. Domain velocity far from the tool is equal to welding traverse speed while the velocity around the pin is different. Schematic representation of velocity field as a result of welding traverse and rotational speeds around pin is shown in Figure 6.2. The following analytical equation has been used for considering the material flow around pin (Tongne, Jahazi, Feulvarch, & Desrayaud, 2015).

$$v_x = v_{weld}\left(1 - R_{pin}\frac{(x^2 - y^2)}{(x^2 + y^2)}\right) - \omega {R_{pin}}^2\left(\frac{y}{x^2 + y^2}\right) \tag{6.2}$$

$$v_y = v_{weld}\left(-2R_{pin}\frac{(xy)}{(x^2 + y^2)}\right) - \omega {R_{pin}}^2\left(\frac{x}{x^2 + y^2}\right) \tag{6.3}$$

$$v_z = 0 \tag{6.4}$$

where R_{pin} is the pin radios, ω is the rotational speed of the tool, v_{weld} is welding speed and x and y are the distances from origin of Cartesian coordinate which is located on the center of moving tool.

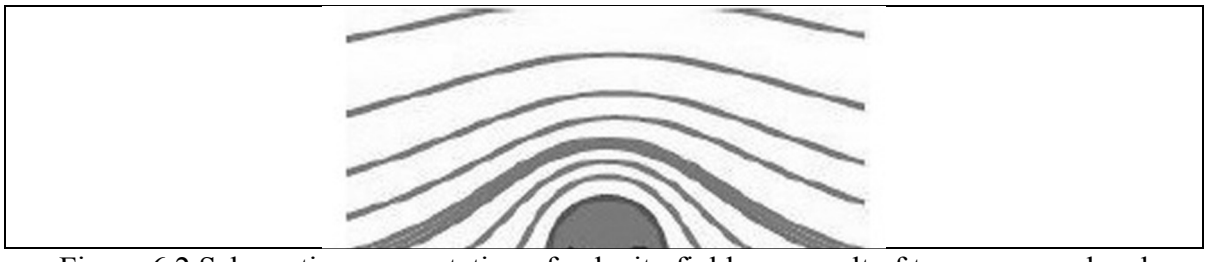

Figure 6.2 Schematic representation of velocity field as a result of traverse speed and rotational speed.

6.2.3.2 Heat generation modeling

In the present model, two different heat generation sources have been considered. The first heat generation source is due to the interface of tool shoulder and workpiece surface and the second one is due to the interface of pin and workpiece. Song equations (Song & Kovacevic, 2003) has been used for the modeling of the heat generation. The heat due to frictional work at the interface of tool shoulder and workpiece is calculated as follows:

$$q_{soulder}(r,T) = 2\pi\mu F\omega r \tag{6.5}$$

where r is the distance from the calculated point to the axis of the rotating tool, F is normal force of welding and μ is the coefficient of friction.

Shearing of the material by pin movement, friction on the threaded surface of the pin and friction on the vertical surface result in the following equations 6.6-6.10.

$$q_{pin}(T) = 2\pi R_{pin} h\bar{Y}\frac{V_m}{\sqrt{3}} + \frac{2\mu\pi\bar{Y}R_{pin}hV_{rp}}{\sqrt{3(1+\mu^2)}} + \frac{4F_p\mu V_m\cos\theta}{\pi} \tag{6.6}$$

$$\theta = \frac{\pi}{2} - \gamma - \tan^{-1}\mu \tag{6.7}$$

$$V_m = \frac{\sin\gamma}{\sin(\pi-\theta-\gamma)}v_p \tag{6.8}$$

$$V_{rp} = \frac{\sin\theta}{\sin(\pi-\theta-\gamma)}v_p \tag{6.9}$$

$$v_p = R_{pin}\omega \tag{6.10}$$

where R_{pin}, h, $\bar{Y}, F_p$ and γ are the radius of the tool pin, material thickness of base metal, average shear stress of the material, the translation force during the welding and the thread helix angle of pin, respectively. Tool pin in this investigation was considered thread-less so, only the second term in the equation 4.6 is calculated as the heat input from the tool pin.

6.2.3.3 Cooling modeling

Natural convection has been applied on upper and lower surfaces of the aluminum plates. The following heat flux expression for these surfaces were used:

$$q_{\text{Natural convection}} = h(T_{amb} - T) \tag{6.11}$$

where h is the heat transfer coefficients of natural convection, T_{amb} is the ambient air temperature. It is worth to mention that the convective coefficient being higher for the bottom of workpiece due to presence of steel bottom backing plate (Shi & Wu, 2017).
Surface-to-ambient radiation has been applied on upper surface of the aluminum plates. The corresponding heat flux expressions for this surface were used:

$$q_{Radiation} = \varepsilon\sigma(T_{amb}^4 - T^4) \tag{6.12}$$

where ε is the surface emissivity and σ is the Stefan-Boltzmann constant.
The cooling of the joint during the welding process was considered a uniform convective heat flux in the simulation. Cooling affects the circular area on the workpiece surface and moves with the same welding traverse speed. The cooling rate of workpiece can be calculated as follows:

$$q_{medium} = h_{medium}(T - T_{medium}) \tag{6.13}$$

where T_{medium} corresponds to medium temperature, and $h_c$is the interfacial heat transfer coefficient. Several parameters influence the h_c such as ambient temperature, weld temperature, flow rate of cooling jet, welding traverse speed (Yi Zhang, Ying, Liu, & Wei, 2016).

6.2.4 Boundary and initial conditions

The welding speeds of 50 mm/min with 750 RPM was used as “hot weld” condition while 450 mm/min with 750 RPM is a “cold weld” condition for simulation. On the pin and workpiece interface the following boundary condition has been applied:

$$K\frac{\partial T}{\partial n}\Big|_{\Gamma} = q_{pin} \tag{6.14}$$

While on the shoulder and workpiece interface the used boundary condition goes as follows:

$$K\frac{\partial T}{\partial n}\Big|_{\Gamma} = q_{shoulder} \tag{6.15}$$

The following boundary condition is applied on the top of workpiece.

$$K\frac{\partial T}{\partial n}\Big|_{\Gamma} = q_{\text{natural convection}} + q_{radiation} \tag{6.16}$$

The bottom of workpiece has the following boundary condition.

$$K\frac{\partial T}{\partial n}\Big|_{\Gamma} = q_{\text{natural convection}} \tag{6.17}$$

The following boundary condition is applied on a circular area on the surface around pin of the workpiece for considering the effect of cooling jet.

$$K\frac{\partial T}{\partial n}\Big|_{\Gamma} = q_{medium} \tag{6.18}$$

Details of the data used for the simulation is shown in Table 6.3 and Table 4.3. It should be noted the liquid CO_2 jet was considered as cooling in the simulation. In order to employ reliable values for cooling, the calibration of ref. (Richards et al., 2010) is used for current simulation.

Table 6.2 Data used for simulation

Parameter	sambal	Value	Reference
AA2024 density (gm^{-3})	ρ_{AA2024}	2.78	Comsol database
AA2024 incipient melting temperature (K)	T_{melt}	773	
Specific heat of AA2024 ($J\ kg^{-1}\ K^{-1}$)	$c_{p,AA2024}$	875	
Thermal conductivity of AA2024 ($W\ m^{-1}\ K^{-1}$)	K_{AA2024}	121	
Tool density (gm^{-3})	ρ_{tool}	7.85	
Specific heat of tool ($J\ kg^{-1}\ K^{-1}$)	$c_{p,tool}$	475	
Thermal conductivity of tool ($W\ m^{-1}\ K^{-1}$)	K_{tool}	44.5	
Normal force of welding (kN)	F	10	(K. Kumar & Kailas, 2008)
Stefan-Boltzmann constant ($Wm^{-2}\ K^{-4}$)	σ	5.670367×10^{-8}	(Shi & Wu, 2017)
External emissivity	ε	0.2	(Shi & Wu, 2017)
Heat transfer coefficient at the bottom and sides of the workpiece ($W\ m^{-2}\ K^{-1}$)	h_{bottom}	300	(Shi & Wu, 2017)
Heat transfer coefficient at the top of the workpiece ($W\ m^{-2}\ K^{-1}$)	h_{top}	50	(Shi & Wu, 2017)
Heat transfer coefficient of liquid CO_2 jet ($W\ m^{-2}\ K^{-1}$)	h_{medium}	8000	(Richards et al., 2010)
Boiling temperature for liquid CO_2(K)	T_{medium}	202	(Richards et al., 2010)
Circular area radius affected by cooling liquid CO_2 jet (mm)	R_{medium}	25	(Richards et al., 2010)

Table 6.3 Yield strength of AA2024 at different temperatures (Lipski & Mroziński, 2012).

Data	Values							
Temperature (K)	300	325	350	375	400	425	450	475
Yield strength (MPa)	323	320	314	307	279	305	306	270

6.3 Results and discussion

Temperature distribution of workpiece in hot (50 mm/min) and cold (450 mm/min) welding conditions with and without cooling are shown in Figure 6.3 in an isometric view. The maximum width of HAZ in ZY plane is extracted from Figure 6.3 and shown in Table 6.4, on the basis of the fact that HAZ defined as the zones achieve 648 K (the dissolution temperature of T_1 precipitates for AA2198). It could be seen that HAZ size does not change significantly by increasing the traverse welding speed. It is difficult to discuss on the HAZ size just on the basis of dissolution temperature and it should be noted time (kinetic) and temperature

(thermodynamic) are two determining factors for precipitates dissolution and coarsening. It means it is possible that the HAZ is smaller in the reality for higher advancing speed because the heat exposure time is less. Applying cooling on the joint removes the HAZ zone in the light of fact that the shoulder radios is around 8 mm and the temperature above 648K are located inside the nugget.

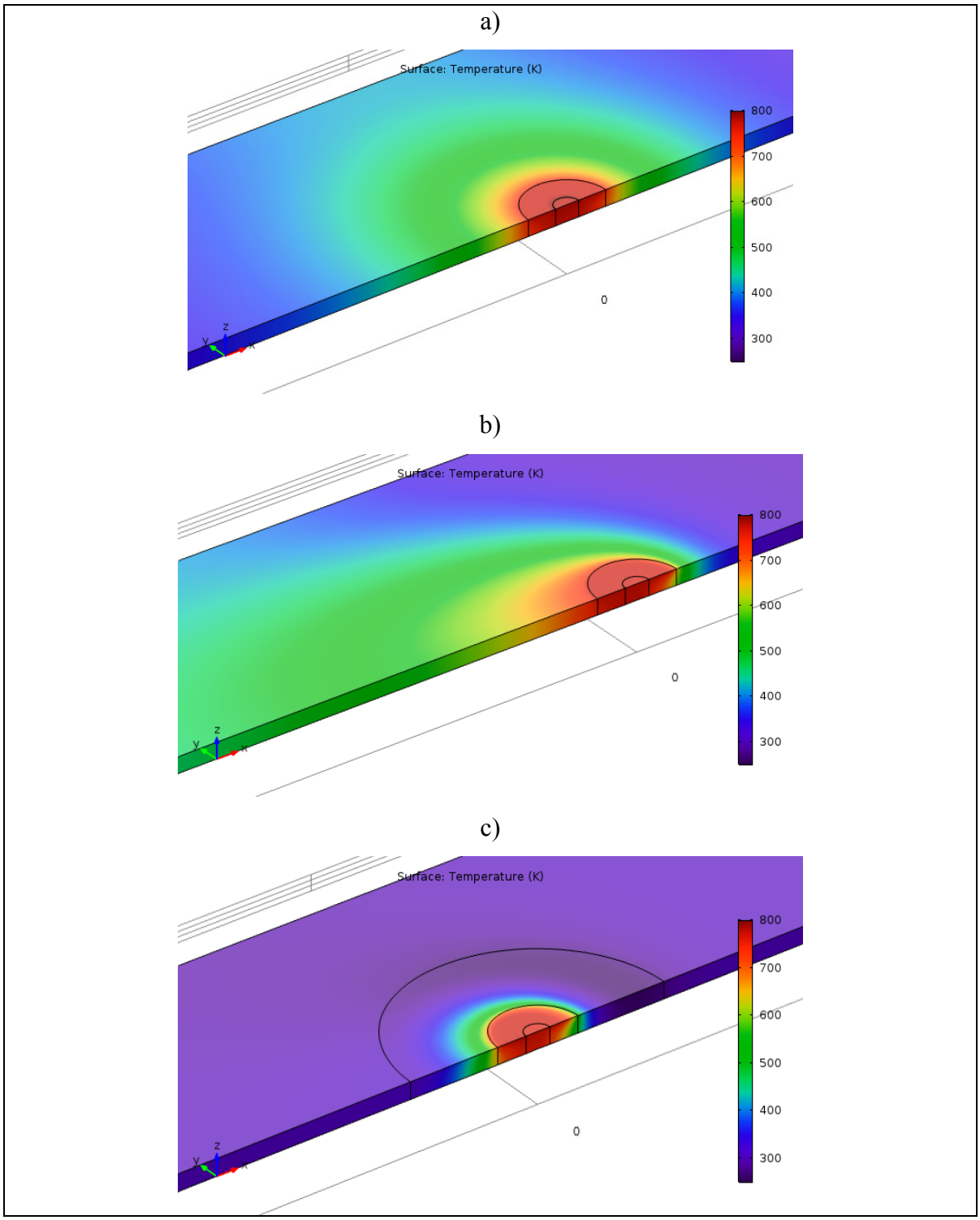

Figure 6.3 Temperature distribution of workpiece in different welding traverse speed and same rotational speed of 750 RPM with and without cooling: a) 50 mm/min b) 450 mm/min c) 450 mm/min with cooling

Table 6.4 Maximum HAZ width in different welding condition.

50 mm/min	450 mm/min	450 mm/min with cooling
11.3 mm	10.3 mm	7.8 mm

The thermal history of a point 2 mm far from the shoulder on the workpiece surface which corresponds to the HAZ for welding speed of 50 mm/min and 750 RPM is reported in Figure 6.4. As it can be seen, simulation results show good agreement with the experimental data measured at both advancing side and retreating side. The over predicted temperature (about 5%) of simulation could be a result of high welding normal force which requires more experimental process to be determined exactly. Besides, other parameters such as accuracy of thermocouples (4% error for type k thermocouples) and experimental process errors such as exact attachment of thermocouples to the predefined location can be the other sources of discrepancies in the results. Faster cooling rate at the end of graph could be result of high considered heat exchange rate for backing plate. More experimental measurement for determining the accurate constants of heat exchange is required to adapt the model with reality.

The effect of welding traverse speed on the thermal history of TMAZ is depicted in Figure 6.5. It should be noted the TMAZ location changes by increasing the traverse speed due to smaller nugget. The edge of TMAZ is calculated from the metallography images (Figure 4.1) and it is 6.5 and 4.5 mm far from the edge of plates for welding speeds of 50 mm/min and 450 mm/min, respectively. It can be seen that 9 times increase in the welding traverse speed (50 mm/min compare to 450 mm/min) cannot decrease the peak temperature, however it decreases significantly the heat exposure time. Therefore, increasing the traverse speed is beneficial and decreases the risk of loss of mechanical properties. However, as mentioned above, even for cold weld conditions, the base metal (HAZ and TMAZ) locally will result in experience temperatures around 750 K which are high temperatures for AA2198 precipitates and result in over aging for AA2024.

The effect of liquid CO_2 cooling jet on the thermal history of a point inside TMAZ is also depicted in Figure 6.6. The point is located at the same place for the three curves, 8 mm far from edge of plates in the middle of thickness (shoulder radios is about 8 mm). This graph demonstrates that the TMAZ of the joint in the cold weld condition with liquid CO_2 cooling jet experiences a peak temperature around 550 K over a shorter time compared to the welding

without external cooling source. This temperature is not harmful for coarsening of AA2024 precipitates or dissolution of AA2198 precipitates. Therefore, the external cooling can solve the loss of mechanical properties in TMAZ of Figure 4.2 at both advancing and retreating sides.

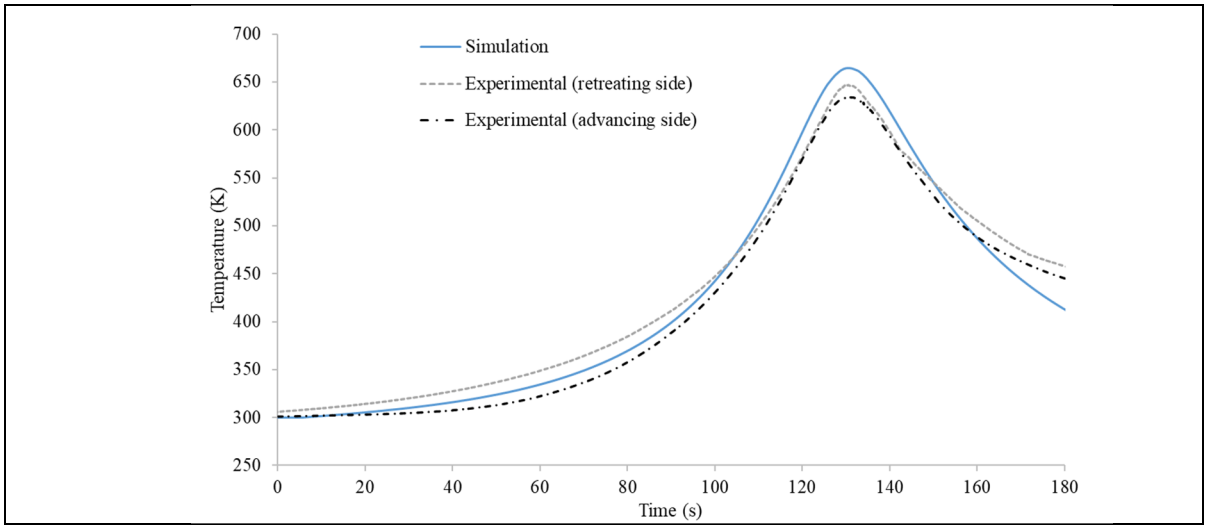

Figure 6.4 The comparison of measured and simulation thermal history of a point 2 mm far from the shoulder (HAZ,750 RPM, 50 mm/min) .

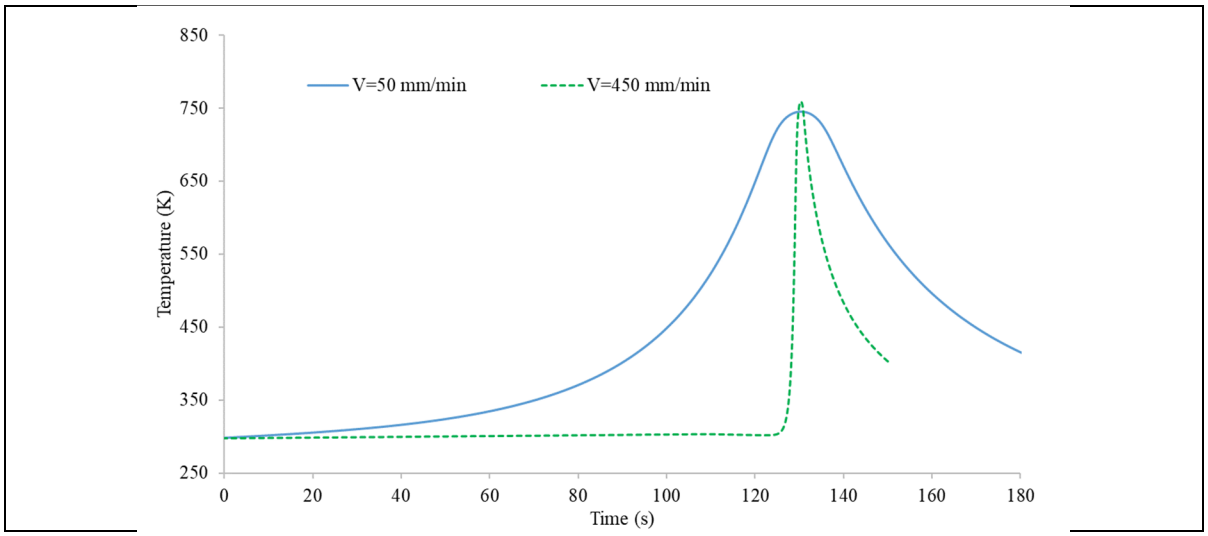

Figure 6.5 The effect of welding traverse speed on thermal history of a point on the edge of TMAZ in the middle of thickness.

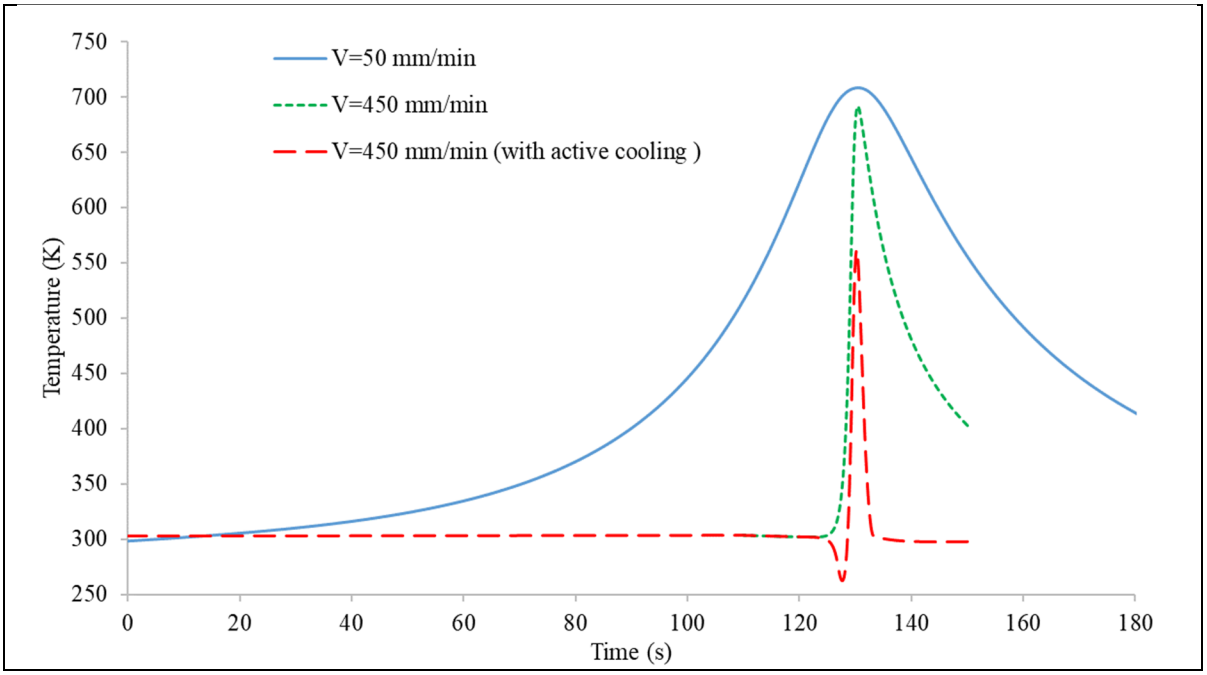

Figure 6.6 The effect of welding traverse speed and cooling jet of liquid CO_2 on thermal history of a point on the edge of shoulder (TMAZ) in the middle of thickness.

6.4 Conclusions

In the present chapter FEM simulation of FSW process was presented in order to investigate the effect of welding traverse speed and cooling jet of liquid CO_2 on the thermal history of HAZ. Results were able to predict experimental data of thermal history of HAZ. Simulation results showed that even with choosing a cold welding condition (fast traverse and low rotational speeds) high temperatures cannot be avoided. Besides, the size of zone which achieve high temperatures decreases negligibility in a cold welding condition in comparison to hot weld condition. It does not mean using cold weld condition is not useful for avoiding loss of mechanical properties in the joint area because the heat exposure time at cold weld condition decreases significantly. The lower heat exposure time limits dissolution precipitation of AA2198 base metal and over aging of AA2024 precipitates. The use of an external cooling system can prevent reaching the harmful temperatures in TMAZ/HAZ and it decrease the heat exposure time significantly. It should mention even by using a cold welding condition with cooling, the nugget of joint will achieve the harmful temperature for AA2198 but with less heat exposure time, so, the external cooling system could be beneficial for increasing the joint

strength thus investment on the cooling equipment for FSW process of AA2198 is recommended. It worth to mention, severe cold condition can enhance the possibility of welding defect. Furthermore, the penetration of liquid CO_2 inside the nugget can affects the mechanical properties. So, practical aspects of using a cooling during welding should be evaluated in the real situation. Modeling of time and temperature effect on precipitates growth or dissolution

CONCLUSIONS

The present study documents various efforts for improving the mechanical properties of friction stir welded joints of AA2198/AA2024 in both T8 and T3 heat treatment conditions. Five different pin profiles (tapered cylindrical, straight cylindrical, thread cylinder, cone and square) with three different shoulder profiles (flat, spiral, and fan) were investigated on simple AA2024 in order to determine the defect-free joints conditions with these tools. They were characterized by means of visual inspection, microstructure analysis, microhardness, and tensile tests. The tools which are able to produce bead on plate weld for AA2024, were selected for joining AA2024 and AA2198. Besides, the influences of traverse and rotational speeds and T8 post weld heat treatment (with and without pre-straining) on the joint mechanical properties have been assessed for the optimal tool. Furthermore, the effect of active cooling during welding to avoid high temperatures has been investigated by FEM simulation. The following points are the main conclusions of the study:

- The tapered cylindrical pin with a fan shoulder produces joints with higher mechanical properties for FSW of AA2198-T3 and AA2024-T3.
- The optimum welding speed parameters with tapered cylindrical pin are 750 RPM and 450 $mm.min^{-1}$ for the highest yield strength. The joint efficiency can reach up to 78%.
- The formation of tunneling defects occurs when increasing the rotational and traverse welding speed over 750 RPM and 450 $mm.min^{-1}$, respectively.
- The formation of kissing bond defects occurs when increasing the traverse welding speed over 150 $mm.min^{-1}$. In this case increasing the pin length may solve the problem.
- Using AA2024 and A2198 plates in T8 and T3 will create joints with similar mechanical properties due to loss of mechanical properties during FSW process, so using T3 plates from economical points of view is recommended if T8 properties is not required.
- Applying post weld heat treatment on joint between AA2024 and AA2198 with or without pre-strained was not effective for mechanical properties improvement.

- The external cooling system could limit the high temperature exposure of the joint, that in turn could reduce undesirable precipitation dissolution of AA2198 and over aging of AA2198 precipitation will beneficial for increasing the joint strength.

RECOMMENDATIONS

In order to create a reliable, defect free and high strength joint between AA2024 and AA2198, the author recommends a FSW tool design composed of tapered cylindrical pin with raised fan shoulder. The welding speed parameters should keep around 750 RPM and 450 mm/min. Higher speed than 150 mm/min could increase the possibility of kissing bond defect so the longer pin is advised. The experiments should run with active cooling system to reduce the heat exposure time and peak temperature. Besides, a more precise material flow model could be helpful for the optimizing tool selection and complete mixing the two base metals. The model should validate at different welding speeds with more thermocouples. The current study shows that applying post aging heat treatment on similar joint of 2198-T3 could be a valuable research. Deeper investigation by TEM microscope could be helpful to find the responsible precipitates for loss of mechanical properties during welding. Besides, AA2198 is sensitive to high temperatures so more investigation is required to modify its chemical composition. Presenting a model for AA2198 material to show quantitative relationships between the yield strengths of the alloys and the sizes, volume percentages of precipitates, related to aging temperature and aging time as well as alloy compositions could be a valuable.

LIST OF BIBLIOGRAPHICAL REFERENCES

Alexopoulos, N. D., Migklis, E., Stylianos, A., & Myriounis, D. P. (2013). Fatigue behavior of the aeronautical Al-Li (2198) aluminum alloy under constant amplitude loading. *International Journal of Fatigue, 56*(0), 95-105. doi:10.1016/j.ijfatigue.2013.07.009

Amirafshar, A., & Pouraliakbar, H. (2015). Effect of tool pin design on the microstructural evolutions and tribological characteristics of friction stir processed structural steel. *Measurement, 68*(0), 111-116. doi:10.1016/j.measurement.2015.02.051

Anil Kumar, K., Karur, A., Chipli, S., & Singh, A. (2015). Optimization of FSW Parameters to Improve the Mechanical Properties of AA2024-T351 Similar Joints Using Taguchi Method. *Journal of Mechanical Engineering and Automation, 5*(3B), 27-32.

Aydın, H., Bayram, A., & Durgun, İ. (2010). The effect of post-weld heat treatment on the mechanical properties of 2024-T4 friction stir-welded joints. *Materials & Design (1980-2015), 31*(5), 2568-2577.

Bitondo, C., Prisco, U., Squilace, A., Buonadonna, P., & Dionoro, G. (2011). Friction-stir welding of AA 2198 butt joints: mechanical characterization of the process and of the welds through DOE analysis. *The International Journal of Advanced Manufacturing Technology, 53*(5-8), 505-516. doi:10.1007/s00170-010-2879-9

Bitondo, C., Prisco, U., Squillace, A., Giorleo, G., & Buonadonna, P. (2010). Friction stir welding of AA2198-T3 butt joints for aeronautical applications. *International Journal of Material Forming, 3*(S1), 1079-1082. doi:10.1007/s12289-010-0958-y

Bitondo, C., Prisco, U., Squillace, A., Giorleo, G., Buonadonna, P., Dionoro, G., & Campanile, G. (2010). Friction stir welding of AA2198-T3 butt joints for aeronautical applications. *International Journal of Material Forming, 3*(1), 1079-1082. doi:10.1007/s12289-010-0958-y

Bussu, G., & Irving, P. E. (2003). The role of residual stress and heat affected zone properties on fatigue crack propagation in friction stir welded 2024-T351 aluminium joints. *International Journal of Fatigue, 25*(1), 77-88. doi:10.1016/S0142-1123(02)00038-5

Cantor, B., Assender, H., & Grant, P. (2015). *Aerospace Materials*: CRC Press.

Chandler, H. (1996). *Heat Treater's Guide: Practices and Procedures for Nonferrous Alloys*: ASM International.

Charit, I., & Mishra, R. S. (2008). Abnormal grain growth in friction stir processed alloys. *Scripta Materialia, 58*(5), 367-371.

Chen, J., Madi, Y., Morgeneyer, T. F., & Besson, J. (2011). Plastic flow and ductile rupture of a 2198 Al–Cu–Li aluminum alloy. *Computational Materials Science, 50*(4), 1365-1371. doi:10.1016/j.commatsci.2010.06.029

De Backer, J. (2014). *Feedback control of robotic friction stir welding.* (Phd), University West, (136)

Deschamps, A., Livet, F., & Bréchet, Y. (1998). Influence of predeformation on ageing in an Al–Zn–Mg alloy—I. Microstructure evolution and mechanical properties. *Acta Materialia, 47*(1), 281-292. doi:10.1016/S1359-6454(98)00293-6

Dixit, V., Mishra, R., Lederich, R., & Talwar, R. (2009). Influence of process parameters on microstructural evolution and mechanical properties in friction stirred Al-2024 (T3) alloy. *Science and Technology of Welding and Joining, 14*(4), 346-355.

Dorin, T., Deschamps, A., De Geuser, F., Lefebvre, W., & Sigli, C. (2014). Quantitative description of the T1 formation kinetics in an Al–Cu–Li alloy using differential scanning calorimetry, small-angle X-ray scattering and transmission electron microscopy. *Philosophical Magazine, 94*(10), 1012-1030.

Dubourg, L., Amargier, R., & Jahazi, M. (2008). *Relationship between FSW parameters, hardness and tensile properties of 7075-T6 and 2098-T851 similar butt welds*. Paper presented at the 7th International Symposium on Friction Stir Welding, Awaji Yumebutai Conference Centre, Awaji Island, Japan.

Dursun, T., & Soutis, C. (2014). Recent developments in advanced aircraft aluminium alloys. *Materials & Design, 56*(0), 862-871. doi:10.1016/j.matdes.2013.12.002

Elangovan, K., & Balasubramanian, V. (2008). Influences of tool pin profile and welding speed on the formation of friction stir processing zone in AA2219 aluminium alloy. *Journal of Materials Processing Technology, 200*(1–3), 163-175. doi:10.1016/j.jmatprotec.2007.09.019

Eramah, A. M., Rakin, M. P., Veljić, D. M., Tadić, S., Radović, N. A., Zrilić, M., & Perović, M. M. (2014). Influence of friction stir welding parameters on properties of 2024 T3 aluminium alloy joints. *Thermal Science, 18*(suppl. 1), 21-28.

Fujii, H., Cui, L., Maeda, M., & Nogi, K. (2006). Effect of tool shape on mechanical properties and microstructure of friction stir welded aluminum alloys. *Materials Science and Engineering: A, 419*(1–2), 25-31. doi:10.1016/j.msea.2005.11.045

Gadakh, V. S., & Adepu, K. (2013). Heat generation model for taper cylindrical pin profile in FSW. *Journal of Materials Research and Technology, 2*(4), 370-375. doi:/10.1016/j.jmrt.2013.10.003

Genevois, C., Deschamps, A., Denquin, A., & Doisneau-cottignies, B. (2005). Quantitative investigation of precipitation and mechanical behaviour for AA2024 friction stir welds. *Acta Materialia, 53*(8), 2447-2458. doi:10.1016/j.actamat.2005.02.007

Giummarra, C., Thomas, B., & Rioja, R. J. (2007). *New Aluminum Lithium alloys for aerospace applications.* Paper presented at the Proceedings of the Light Metals Technology.

Guerra, M., Schmidt, C., McClure, J., Murr, L., & Nunes, A. (2002). Flow patterns during friction stir welding. *Materials characterization, 49*(2), 95-101.

Handbook, A., & Welding, B. (2005). Soldering, vol. 6. *ASM International, Material Park, OH*, 438.

Hasan, M. M., Ishak, M., & Rejab, M. R. M. (2016). Influence of machine variables and tool profile on the tensile strength of dissimilar AA7075-AA6061 friction stir welds. *The International Journal of Advanced Manufacturing Technology*, 1-11. doi:10.1007/s00170-016-9583-3

Heinz, A., Haszler, A., Keidel, C., Moldenhauer, S., Benedictus, R., & Miller, W. S. (2000). Recent development in aluminium alloys for aerospace applications. *Materials Science and Engineering: A, 280*(1), 102-107. doi:10.1016/S0921-5093(99)00674-7

Hu, Z., Yuan, S., Wang, X., Liu, G., & Huang, Y. (2011). Effect of post-weld heat treatment on the microstructure and plastic deformation behavior of friction stir welded 2024. *Materials & Design, 32*(10), 5055-5060. doi:10.1016/j.matdes.2011.05.035

Hunsicker, H. (1984). Metallurgy of heat treatment and general principles of precipitation hardening. *Aluminum: Properties and Physical Metallurgy, ed. by JE Hatch, American Society for Metals, Metals Park, Ohio*, 134-199.

Hwang, Y.-M., Kang, Z.-W., Chiou, Y.-C., & Hsu, H.-H. (2008). Experimental study on temperature distributions within the workpiece during friction stir welding of aluminum alloys. *International Journal of Machine Tools and Manufacture, 48*(7–8), 778-787. doi:10.1016/j.ijmachtools.2007.12.003

ISO 5817: Welding -- Fusion-welded joints in steel, nickel, titanium and their alloys (beam welding excluded) -- Quality levels for imperfections. (2014). In.

ISO 6520: Classification of geometric imperfections in metallic materials. (1998).

ISO 10042: Welding -- Arc-welded joints in aluminium and its alloys -- Quality levels for imperfections. (2005).

Ji, S., Xing, J., Yue, Y., Ma, Y., Zhang, L., & Gao, S. (2013). Design of friction stir welding tool for avoiding root flaws. *Materials, 6*(12), 5870-5877.

Kadlec, M., Růžek, R., & Nováková, L. (2015). Mechanical behaviour of AA 7475 friction stir welds with the kissing bond defect. *International Journal of Fatigue, 74*, 7-19. doi:10.1016/j.ijfatigue.2014.12.011

Kamble, L., Soman, S., & Brahmankar, P. (2012). Effect of Tool Design and Process Variables on Mechanical Properties and Microstructure of AA6101-T6 Alloy Welded by Friction Stir Welding. *Journal of Mechanical and Civil Engineering (IOSR-JMCE)*.

Kasman, Ş. (2016). Effects of FSW parameters and pin geometry on the weldability of EN AW 2024 alloy. *Materials Testing, 58*(7-8), 694-701.

Knüwer, M., Schumacher, J., Ribes, H., Eberl, F., & Bes, B. (2006). *2198-Advanced Aluminium-Lithium Alloy for A350 Skin Sheet Application.* Paper presented at the Presentation for the 17th AeroMat Conference & Exposition. Seattle, USA.

Kumar, K., & Kailas, S. V. (2008). The role of friction stir welding tool on material flow and weld formation. *Materials Science and Engineering: A, 485*(1-2), 367-374. doi:10.1016/j.msea.2007.08.013

Kumar, R., Singh, K., & Pandey, S. (2012). Process forces and heat input as function of process parameters in AA5083 friction stir welds. *Transactions of Nonferrous Metals Society of China, 22*(2), 288-298. doi:10.1016/S1003-6326(11)61173-4

Le Jolu, T., Morgeneyer, T. F., Denquin, A., & Gourgues-Lorenzon, A.-F. (2015). Fatigue lifetime and tearing resistance of AA2198 Al–Cu–Li alloy friction stir welds: Effect of defects. *International Journal of Fatigue, 70*, 463-472.

Le Jolu, T., Morgeneyer, T. F., Denquin, A., Sennour, M., Laurent, A., Besson, J., & Gourgues-Lorenzon, A.-F. (2014). Microstructural Characterization of Internal Welding Defects and Their Effect on the Tensile Behavior of FSW Joints of AA2198 Al-Cu-Li Alloy. *Metallurgical and Materials Transactions A, 45*(12), 5531-5544.

Le Jolu, T., Morgeneyer, T. F., & Gourgues-Lorenzon, A.-F. (2010). *Effect of friction stir weld defects on fatigue lifetime of an Al-Cu-Li alloy.* Paper presented at the Fracture of materials and structures from micro to macro scale-ECF 18.

Li, X., Song, N., Guo, G., & Sun, Z. (2013). Prediction of forming limit curve (FLC) for Al–Li alloy 2198-T3 sheet using different yield functions. *Chinese Journal of Aeronautics, 26*(5), 1317-1323.

Lipski, A., & Mroziński, S. (2012). The Effects of Temperature on the Strength Properties of Aluminium Alloy 2024-T3. *acta mechanica et automatica, 6*, 62-66.

Lohwasser, D., & Chen, Z. (2009). *Friction Stir Welding: From Basics to Applications*: Elsevier Science.

Ma, Y. E., Xia, Z. C., Jiang, R. R., & Li, W. (2013). Effect of welding parameters on mechanical and fatigue properties of friction stir welded 2198 T8 aluminum–lithium alloy joints. *Engineering Fracture Mechanics, 114*(0), 1-11. doi:10.1016/j.engfracmech.2013.10.010

Masoumi, M., Zedan, Y., Texier, D., Jahazi, M., & Bocher, P. (2016). *Optimization of friction stir welding tool geometry and parameters for joining AA2024 and AA2198*. Paper presented at the The International Committee for Study of Bauxite, Alumina & Aluminium conference, Quebec City, Canada.

Mastanaiah, P., Sharma, A., & Reddy, G. M. (2016). Dissimilar Friction Stir Welds in AA2219-AA5083 Aluminium Alloys: Effect of Process Parameters on Material Inter-Mixing, Defect Formation, and Mechanical Properties. *Transactions of the Indian Institute of Metals, 69*(7), 1397-1415. doi:10.1007/s12666-015-0694-6

McQueen, H., Cabibbo, M., Evangelista, E., Spigarelli, S., Di Paola, M., & Falchero, A. (2013). Microstructure and mechanical properties of AA6056 friction stir welded plate. *Metallurgical Science and Tecnology, 24*(1).

Meilinger, Á., & Török, I. (2013). The importance of friction stir welding tool. *Production Processes and Systems, 6*(1), 25-34.

Mishra, R. S., & Ma, Z. (2005). Friction stir welding and processing. *Materials Science and Engineering: R: Reports, 50*(1), 1-78.

Mohanty, H. K., Mahapatra, M. M., Kumar, P., Biswas, P., & Mandal, N. R. (2012). Effect of tool shoulder and pin probe profiles on friction stirred aluminum welds — a comparative study. *Journal of Marine Science and Application, 11*(2), 200-207. doi:10.1007/s11804-012-1123-4

Muruganandam, D., Raguraman, D., & Kumaraswamidhas, L. A. (2015). Effect of post-welding heat treatment on mechanical properties of butt FSW joints in high strength aluminium alloys. *Indian Journal of Engineering and Materials Sciences, 22*(4), 381-388.

Mustafa, F. F., Kadhym, A. H., & Yahya, H. H. (2015). Tool Geometries Optimization for Friction Stir Welding of AA6061-T6 Aluminum Alloy T-Joint Using Taguchi Method to Improve the Mechanical Behavior. *Journal of Manufacturing Science and Engineering, 137*(3), 031018. doi:10.1115/1.4029921

Pieta, G., dos Santos, J., Strohaecker, T., & Clarke, T. (2014). Optimization of friction spot welding process parameters for AA2198-T8 sheets. *Materials and Manufacturing Processes, 29*(8), 934-940.

Prasad, N. E., Gokhale, A., & Wanhill, R. J. H. (2013). *Aluminum-Lithium Alloys: Processing, Properties, and Applications*: Elsevier Science.

Radisavljevic, I., Zivkovic, A., Radovic, N., & Grabulov, V. (2013). Influence of FSW parameters on formation quality and mechanical properties of Al 2024-T351 butt welded joints. *Transactions of Nonferrous Metals Society of China, 23*(12), 3525-3539. doi:10.1016/s1003-6326(13)62897-6

Rai, R., De, A., Bhadeshia, H., & DebRoy, T. (2011). Review: friction stir welding tools. *Science and Technology of Welding and Joining, 16*(4), 325-342.

Reza-E-Rabby, M., & Reynolds, A. P. (2014). Effect of Tool Pin Thread Forms on Friction Stir Weldability of Different Aluminum Alloys. *Procedia Engineering, 90*(0), 637-642. doi:10.1016/j.proeng.2014.11.784

Richards, D., Prangnell, P., Withers, P., Williams, S., Nagy, T., & Morgan, S. (2010). Efficacy of active cooling for controlling residual stresses in friction stir welds. *Science and Technology of Welding and Joining, 15*(2), 156-165.

Rioja, R. J., & Liu, J. (2012). The Evolution of Al-Li Base Products for Aerospace and Space Applications. *Metallurgical and Materials Transactions A, 43*(9), 3325-3337. doi:10.1007/s11661-012-1155-z

Robe, H., Zedan, Y., Chen, J., Feulvarch, E., & Bocher, P. (2015). Microstructural and mechanical characterization of a dissimilar friction stir welded butt joint made of AA2024-T3 and AA2198-T3. *Materials Characterization*. doi:10.1016/j.matchar.2015.10.029

Roberto, J. R., & John, L. (2012). The Evolution of Al-Li Base Products for Aerospace and Space Applications. *Metallurgical and Materials Transactions A, 43*(9), 3325-3337. doi:10.1007/s11661-012-1155-z

Salari, E., Jahazi, M., Khodabandeh, A., & Ghasemi-Nanesa, H. (2014). Influence of tool geometry and rotational speed on mechanical properties and defect formation in friction stir lap welded 5456 aluminum alloy sheets. *Materials & Design, 58*, 381-389. doi:10.1016/j.matdes.2014.02.005

Saravanan, V., Rajakumar, S., Banerjee, N., & Amuthakkannan, R. (2016). Effect of shoulder diameter to pin diameter ratio on microstructure and mechanical properties of dissimilar friction stir welded AA2024-T6 and AA7075-T6 aluminum alloy joints. *The International Journal of Advanced Manufacturing Technology, 87*(9), 3637-3645. doi:10.1007/s00170-016-8695-0

Sattari, S., Bisadi, H., & Sajed, M. (2012). Mechanical Properties and Temperature Distributions of Thin Friction Stir Welded Sheets of AA5083. *Mechanics and Applications, 2*(1), 1-6. doi:10.5923/j.mechanics.20120201.01

Scialpi, A., De Filippis, L. A. C., & Cavaliere, P. (2007). Influence of shoulder geometry on microstructure and mechanical properties of friction stir welded 6082 aluminium alloy. *Materials & Design, 28*(4), 1124-1129. doi:10.1016/j.matdes.2006.01.031

Shi, L., & Wu, C. S. (2017). Transient model of heat transfer and material flow at different stages of friction stir welding process. *Journal of Manufacturing Processes, 25*, 323-339. doi:10.1016/j.jmapro.2016.11.008

Shigematsu, I., Kwon, Y. J., Suzuki, K., Imai, T., & Saito, N. (2003). Joining of 5083 and 6061 aluminum alloys by friction stir welding. *Journal of Materials Science Letters, 22*(5), 353-356. doi:10.1023/A:1022688908885

Song, M., & Kovacevic, R. (2003). Thermal modeling of friction stir welding in a moving coordinate system and its validation. *International Journal of Machine Tools and Manufacture, 43*(6), 605-615. doi:10.1016/S0890-6955(03)00022-1

Srivatsan, T. S., Vasudevan, S., & Park, L. (2007). The tensile deformation and fracture behavior of friction stir welded aluminum alloy 2024. *Materials Science and Engineering: A, 466*(1), 235-245. doi:10.1016/j.msea.2007.02.100

Sullivan, A., & Robson, J. (2008). Microstructural properties of friction stir welded and post-weld heat-treated 7449 aluminium alloy thick plate. *Materials Science and Engineering: A, 478*(1), 351-360.

Texier, D., Zedan, Y., Amoros, T., Feulvarch, E., Stinville, J. C., & Bocher, P. (2016). Near-surface mechanical heterogeneities in a dissimilar aluminum alloys friction stir welded joint. *Materials & Design, 108*, 217-229. doi:10.1016/j.matdes.2016.06.091

Tongne, A., Jahazi, M., Feulvarch, E., & Desrayaud, C. (2015). Banded structures in friction stir welded Al alloys. *Journal of Materials Processing Technology, 221*, 269-278. doi:10.1016/j.jmatprotec.2015.02.020

Trueba Jr., L., Heredia, G., Rybicki, D., & Johannes, L. B. (2015). Effect of tool shoulder features on defects and tensile properties of friction stir welded aluminum 6061-T6. *Journal of Materials Processing Technology, 219*(0), 271-277. doi:10.1016/j.jmatprotec.2014.12.027

Zhang, S.-f., Zeng, W.-d., Yang, W.-h., Shi, C.-l., & Wang, H.-j. (2014). Ageing response of a Al–Cu–Li 2198 alloy. *Materials & Design, 63*, 368-374.

Zhang, Y., Cao, X., Larose, S., & Wanjara, P. (2012). Review of tools for friction stir welding and processing. *Canadian Metallurgical Quarterly, 51*(3), 250-261.

Zhang, Y., Ying, Y., Liu, X., & Wei, H. (2016). Deformation control during the laser welding of a Ti6Al4V thin plate using a synchronous gas cooling method. *Materials & Design, 90*, 931-941. doi:10.1016/j.matdes.2015.11.035

Zhou, C., Yang, X., & Luan, G. (2006). Effect of oxide array on the fatigue property of friction stir welds. *Scripta Materialia, 54*(8), 1515-1520. doi:10.1016/j.scriptamat.2005.12.036